List of Contributors

H. Yoshimizu and Y. Tsujita, *Department of Material Science and Engineering, Nagoya Institute of Technology, Gakiso, Showa-ku, Nagoya 466, Japan*

K. Saito, K. Kanehashi and I. Komaki, *Advanced Technology Research Laboratories, Nippon Steel Corporation, 20–1 Shintomi-chou Futtsu City, Chiba, 293–8511, Japan*

K. Asayama, Y. Kitaoka, G.-q. Zheng, K. Ishida and Y. Tokunaga, *Faculty of Engineering Science, Osaka University, Toyonaka, Osaka, Japan*

Preface

It is a great pleasure for me to introduce volume 44 of *Annual Reports on NMR Spectroscopy* and to welcome my longstanding co-worker, Professor I. Ando of the Tokyo Institute of Technology as co-editor. This is another in the series of special issues of *Annual Reports on NMR Spectroscopy* and covers advances in applications of NMR to materials science, an area previously visited in volume 28 of this series. Three quite distinct topics are included in this volume, namely Applications of NMR Spectroscopy to the Structure and Ionic Aggregates of Ionomers by H. Yoshimizu and Y. Tsujita, Applications of NMR Techniques to Coal Science by K. Saito, K. Kanehashi and I. Komaki and An NMR Study of Strongly Correlated Superconductors by K. Asayama, Y. Kitaoka, G-q. Zheng, K. Ishida and Y. Tokunaga.

My thanks are due to all of these contributors, to my co-editor and to the production staff at Academic Press (London) for their cooperation in the creation of this volume.

University of Surrey
Guildford, Surrey
UK

G. A. WEBB
November 2000

Applications of NMR Spectroscopy to the Structure and Ionic Aggregates of Ionomers

H. YOSHIMIZU and Y. TSUJITA

Department of Materials Science and Engineering, Polymeric Materials Course, Nagoya Institute of Technology, Gokiso-cho, Showa-ku, Nagoya 466-8555 Japan

1. INTRODUCTION

In general, ionomers are defined as polymers with non-polar backbones containing up to about 10 mol% salt group of, for example, carboxyl, sulfonic, acids. and pyridinum groups, either present as pendant groups or directly incorporated into the main chain. The classifications of ionomers, therefore, become complicated. Familiar and conventional names of ionomers are formed by using the names of host polymers, such as ethylene ionomers and styrene ionomers. In addition, the types of ionic groups, i.e. anionic and cationic ionomers, and the types of chemical structures such as random copolymers, block copolymers (including AB diblock, triblock, star-like, and graft types), and telechelic types are used.

The fields of application of ionomers are very wide because of their great variety of characteristics. For example, the ethylene ionomers are used as heat seals, adhesive layers in foil/paper containers, packaging films, rubbers for golf ball covers, and sports shoes, etc., because the hydrophilic ionic groups are separated from the hydrophobic polymer matrix to form small ionic domains

ANNUAL REPORTS ON NMR SPECTROSCOPY
VOLUME 44 ISBN 0-12-505344-4

(ionic aggregates); the formation of the ionic aggregates improves tensile strength, impact resistance and optical properties. Many ionomers are used as micellar and/or self-assembly materials, compatibilizer for polymer blends, ion selective or separation membranes, etc.

A great number of reports on ionomers from research and academic areas to industrial applications have been published.[1-4] The structural details and the effects on physical properties of ionic aggregates in ionomers have been much studied by many techniques, including small-angle X-ray scattering (SAXS), electron microscopy, infrared spectroscopy (IR), thermal analyses, and mechanical and dielectric measurements. Magnetic resonance spectroscopic studies on ionomers, however, are relatively fewer than others, except for ESR studies on the characterization of ionic aggregates using paramagnetic ions.

The purpose of the present chapter is to overview recent applications of NMR to the structure and ionic aggregates of ionomers, in particular the ethylene ionomers. It is expected that more NMR studies on ionomers will be activated by this review.

2. ETHYLENE IONOMERS

In this section, the metal-cationic salts of copoly(ethylene-methacrylic acid) are called the ethylene ionomers. This ethylene ionomer is one of the well-known commercial ionomers, marketed under the trade name Surlyn by DuPont. Many ethylene ionomers have crystalline and amorphous phases of ethylene chain units as well as polyethylene. Therefore, there is a three-phase structure, with crystalline, amorphous, and ionic aggregate phases; this is a unique characteristic of ethylene ionomers compared with other ionomers. Although the ionic aggregate structure of the ethylene ionomer has not been fully established, its structural model is represented[5] as shown in Fig. 1. In ethylene ionomers, therefore, it is necessary that some physical properties should be considered by correlating to not only the ionic aggregates but also the crystalline phases.

2.1. Physical properties of ethylene ionomers

First, the thermal properties of ethylene ionomers are reviewed. The melting behaviour observed by differential scanning calorimetry (DSC) measurement of poly(ethylene-co-methacrylic acid) and its salt has been discussed by several researchers.[6-18] A reduction in crystallinity with increasing degree of neutralization was reported,[6] however, a considerable increase in crystallinity was observed with annealing of the ionomer.[5,7-9] In addition, a morphological change after annealing was observed during light-scattering studies.[19] Wunderlich conjectured that the difference in the melting behaviour of the

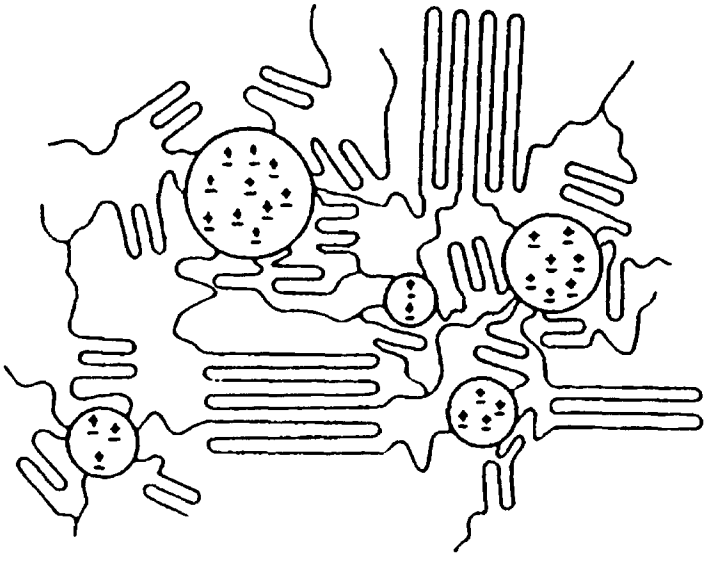

Fig. 1. Structural model of ethylene ionomers.

ionomers relative to the acid copolymers is caused largely by the hindered crystallization of the melt, which is much more viscous.[10]

Figure 2 shows DSC thermograms obtained on heating (10 °C/min^{-1}) zinc salts of ethylene ionomers which had been stored at room temperature for a long time. Two endothermic peaks appeared at around 50–60 °C and 90 °C in all samples. The higher temperature peak became smaller and shifted to lower temperature with an increase in the degree of neutralization: the lower temperature peak became larger and shifted to a higher temperature. These two endothermic peaks for ethylene ionomers were assigned as follows: the lower temperature peak was attributed to the melting of crystallites formed by annealing, and the higher peak was attributed to crystallites formed by cooling. Ionic aggregates, which play the role of crosslinking, hinder the crystallization of ethylene ionomer upon faster cooling such as quenching. Consequently, crystallization of the ethylene ionomer aged at room temperature, which is higher than the glass transition temperature of this polymer, proceeds much more remarkably than that of low-density polyethylene (LDPE). The fusion curves observed by DSC measurement were presumably due to not only the melting of the crystallites which exist before the measurement, but also the recrystallization and/or thickening after the melting of part of the original crystallites and subsequent melting during the measurement. Furthermore the lower temperature peak caused by the ageing is indicative of superheating.

Next, an attempt was made to clarify the effect of crystalline phase on the mechanical properties of ethylene ionomer. Dynamic mechanical measurements

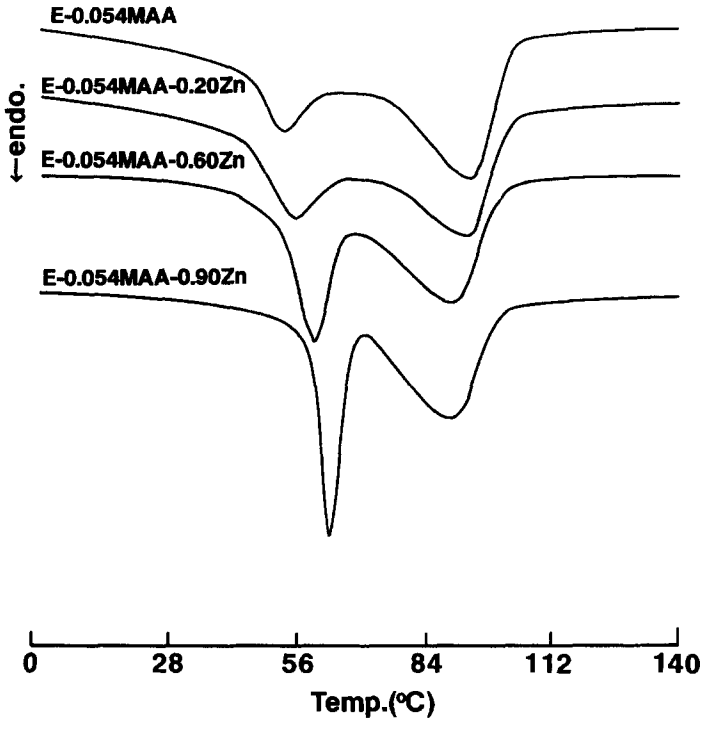

Fig. 2. DSC thermograms of the zinc salt of ethylene ionomers after ageing at room temperature for a long time (heating rate 10 °C/min). These ethylene ionomers are copoly(ethylene-methacrylic acid) with an acid content of 0.054 and various degrees of neutralization (E-0.054MAA-xZn): $x = 0$, 0.20, 0.60, and 0.90.

(DMS) were performed on zinc salts of ethylene ionomers. Figure 3 shows the temperature dependence of the loss tangent, tan δ, for the zinc salts of ethylene ionomers. When neutralization was increased to 60% or higher, α and β relaxation appeared. The α relaxation, which was previously assigned by other researchers to a glass–rubber transition of the ionic aggregate phase in the ethylene ionomer, shifted to higher temperatures, while the β relaxation stayed at almost the same temperature (ca. −20 °C) with increasing neutralization. MacKnight *et al.* explained that β relaxation in the ionomers arises from the amorphous hydrocarbon phase and is identical to the β relaxation in a branched polyethylene.[20] Therefore, the appearance of α and β relaxation is regarded as indicating the phase separation of ionic aggregates from the polyethylene matrix and the formation of ionic aggregates. Figure 4 shows the frequency dependence of the α relaxation of the ethylene ionomer. This tan δ peak is obviously independent of the frequency. This indicates that a first-order transition occurs at around the α relaxation temperature. The assignments of tan δ peaks are summarized in Table 1.

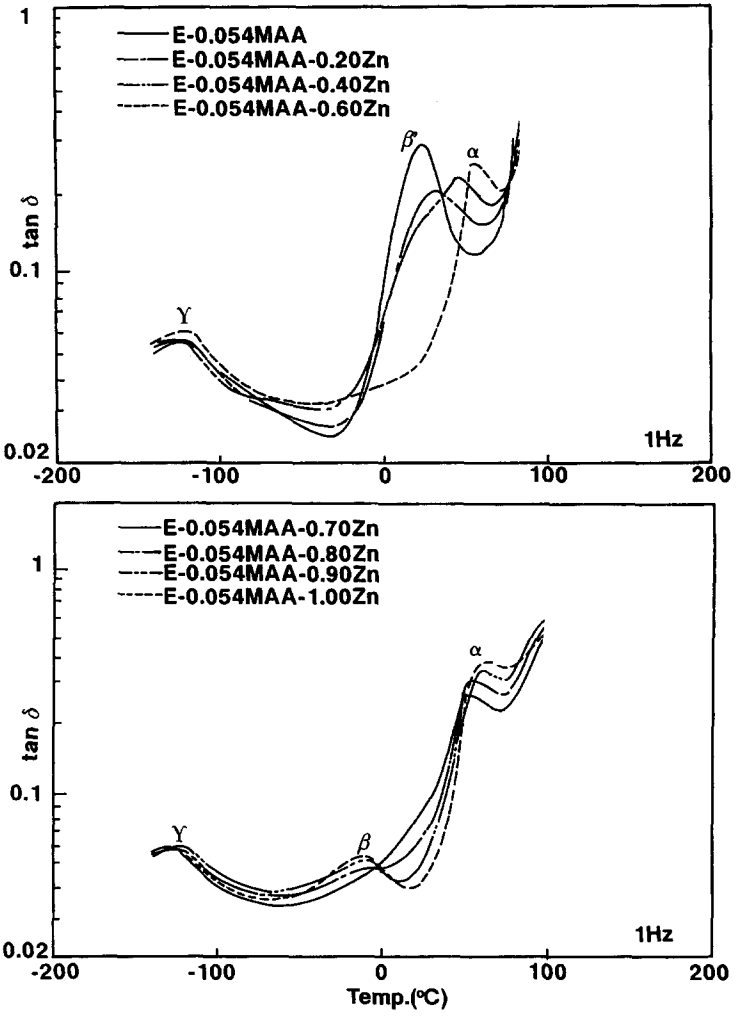

Fig. 3. The temperature dependence of tan δ at a frequency of 1 Hz for the zinc salt of ethylene ionomers. These ethylene ionomers are copoly(ethylene-methacrylic acid) with an acid content of 0.054 and various degrees of neutralization (E-0.054MAA-xZn: x is the degree of neutralization).

The α relaxation exhibits a thermal history: that is, in the tan δ curve of the ionomer quenched from 80 °C for 30 min to room temperature, the α relaxation disappeared and then, by ageing at room temperature for a long time, the tan δ curve was restored to that of the original specimen.

As mentioned above, the lower temperature DSC peak was attributed to the melting of the crystallites formed by annealing and the higher peak to that by cooling. Ionic aggregates, which play the role of crosslinking, hindered

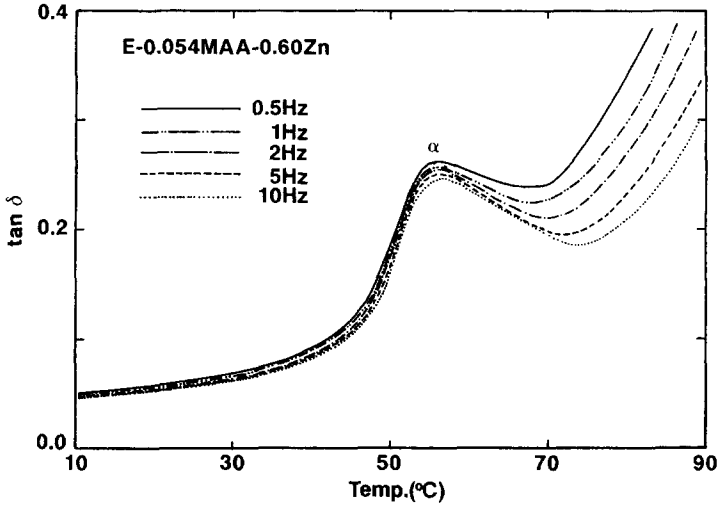

Fig. 4. The temperature dependence of tan δ at various frequencies for the zinc salt of ethylene ionomer. This ethylene ionomer is copoly(ethylene-methacrylic acid) with an acid content of 0.054 and a degree of neutralization of 0.6 (E-0.054MAA-0.6Zn).

Table 1. Temperatures of mechanical dispersions at 1 Hz

Sample	Mechanical dispersion temperature (°C)				
	α_1	α_2	β'	β	γ
E-0.054MAA	–	–	23.3	–	−123.3
E-0.054MAA-0.20Zn	–	–	31.8	–	−125.0
E-0.054MAA-0.60Zn	55.4	–	–	–	−123.0
E-0.054MAA-0.80Zn	54.2	63.3	–	−9.5	−127.8
E-0.054MAA-0.90Zn	57.0	67.2	–	−11.2	−125.7
E-0.054MAA-0.20Na	–	–	40.8	–	−125.5
E-0.054MAA-0.60Na	–	75.7	–	−20.0	−125.5
E-0.054MAA-0.90Na	63.0	78.7	–	−22.2	−125.1

E-0.054MAA means copoly(ethylene-methacrylic acid) with acid content = 0.054, and xZn and xNa mean the degree of neutralization with zinc and sodium cations, respectively.

α_1 melt of the isothermally crystallized part in the polyethylene matrix
α_2 motions of large segment related with the melt of the isothermally crystallites
β' motions of segments containing carboxylic acid existing in the form of interchain hydrogen bonded dimers (the grass transition of E-0.054MAA)
β motions of segments in amorphous part of the polyethylene matrix (the glass transition of the phase-separated polyethylene matrix)
γ 'crankshaft'-type motions of linear methylene sequences.

crystallization of the ethylene ionomer upon faster cooling such as quenching. Consequently, crystallization of the ionomer aged at room temperature, which is higher than the glass transition temperature of this polymer, proceeded much more remarkably than that of LDPE. The melting of the crystallites is also a first-order transition. Therefore, we assigned the α relaxation to the melting of the crystallites formed by the ageing at room temperature for a long time. The growth of this crystallite depends on the neutralization because the amount and/or size of the crystallites formed by quenching decreased with increasing amount and/or size of ionic aggregates. Accordingly, both the α relaxation temperature and the lower DSC peak temperature are elevated with neutralization.

The ESR spectra of spin-probe (TEMPO)-containing ethylene ionomers were measured in order to clarify the structure and molecular dynamics of the ionomers in more detail.[21] TEMPO is one of the probes used to obtain information on the polyethylene matrix, because of its hydrophobic properties. It is considered that TEMPO exists favourably in the polyethylene matrix and does not approach close to the ionic aggregates. At low temperatures, the ESR spectra of TEMPO-containing ethylene ionomers have a broad line shape suggesting that the polymer matrix is in a rigid state. With increasing temperature a narrowing of the peak separation occurs because the mobility of TEMPO becomes high. In the case of a low degree of neutralization, a very small subsplitting appears above -20 °C, indicating that TEMPO experiences at least two dynamic states in its microenvironments. This was not observed for the ethylene ionomer with a high degree of neutralization. The temperature at which the separation of the outermost peaks of the ESR spectrum of the nitroxide spin probes in a polymer matrix is 50 G (T_{50G}), is a valuable tool for T_g determination.[22] The values of T_{50G} for ethylene ionomers were estimated to be in the range -20 to $+30$ °C. These values are consistent with the mechanical dispersion temperatures obtained from dynamic mechanical analysis.

2.2. Ionic aggregates of ethylene ionomers

Ionic aggregates can play the role of physical crosslinking and provide an important and characteristic viscoelastic behaviour of ionomers. The presence of ionic aggregates is the most characteristic feature of the physical properties of ionomers. There are, however, few structural morphological studies on ionic aggregates and there exist no comprehensive conclusions about them at the present time.[23] Electron microscopic observations have been reported by some researchers.[24,25] Longworth *et al.*[1] observed a black spot with a radius of 150 Å probably assigned to the ionic aggregates of an ethylene ionomer containing a rubidium salt. On the other hand, Cooper *et al.*[26] report the size of aggregates of butadiene-methacrylic acid sodium salt ionomer to be 13–26 Å, and Philips *et al.*[27] observed a similar size for ethylene-phosphoric acid cesium salt

ionomer. Many small-angle X-ray scattering (SAXS) studies on ionomers have been carried out but there are still some unresolved problems.[23,28-30] Many structural models of ionic aggregates have been proposed, i.e. ball-like structure[28] of pseudocrystalline array, core-shell structure,[23] lamellar structure, cylindrical structure,[29] those with a modified structure and so on. Yarusso and Cooper examined the proposed structures experimentally and theoretically and found that a modified hard sphere model is a much more suitable structural model for the ionic aggregates, and gives better agreement between the observed and calculated SAXS profiles.[23]* SAXS profiles of the ethylene ionomers were studied to clarify the structure of ionic aggregates in them as functions of the species of cations, acid content, and degree of neutralization.[31]

An ionic aggregates peak was observed for the ionomers with a certain degree of neutralization. In Fig. 5, observed SAXS profiles of the sodium salts of ethylene ionomers are plotted against calculated ones by a nonlinear least squares method using Yarusso and Cooper's structural model. The intensity of the ionic aggregates peak increases and the peak shifts to a smaller angle with an increase in the degree of neutralization. The observed profile agrees fairly well with the corresponding calculated curve, indicating that the structure of ionic aggregates may be interpreted in terms of the modified hard sphere model proposed by Yarusso and Cooper. The structural parameters obtained by the curve fitting method for the sodium and zinc salts of ethylene ionomers used in

* Yarusso and Cooper[23,32] derived the theoretical X-ray scattering intensity based on various structure models with different electron densities and radii of the ionic aggregates. They made the calculated scattering curve fit the observed one and as a result, have found the most suitable structural model for ionic aggregates to be a modified hard sphere model, for which X-ray scattering intensity is represented by the following equation.

$$I(q) = I_e(q)V\frac{1}{V_p}V_1^2\rho_1^2\Phi^2(qR_1)\frac{1}{1+\left(\dfrac{8\,V_{ca}}{V_p}\right)\varepsilon\Phi(2qR_{ca})}$$

$$V_{ca} = \tfrac{4}{3}\pi R_{ca}^3 \qquad V_1 = \tfrac{4}{3}\pi R_1^3 \qquad \Phi(\chi) = 3\,\frac{\sin\chi - \chi\cos\chi}{\chi^3}$$

where q is the magnitude of the scattering wave vector represented as $q = (4\pi/\lambda)\sin\theta$, where 2θ is the angle between the incident and scattered beams, and λ is the radiation wavelength. $I_e(q)$ is the intensity scattered by a single electron under the experimental conditions and $I(q)$ is the observed intensity; V_p and V are the average system volume per particle of ionic aggregates, and the volume of the sample illuminated by the X-ray beam, respectively; ρ_1 is the electron density difference between matrix and ionic aggregate, ε is a constant very close to one, R_1 is the radius of the ionic aggregate, and $2R_{ca}$ is the closest approach distance between two ionic aggregates.

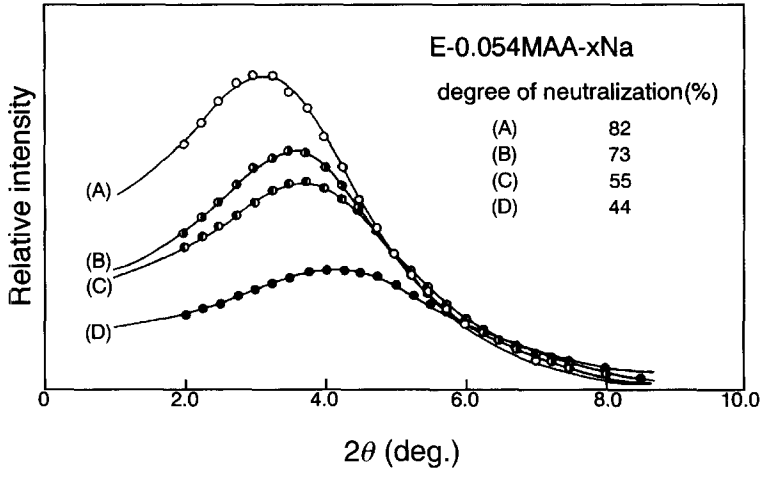

Fig. 5. Observed and calculated curves of SAXS profiles by a modified hard-sphere model for the sodium salt of ethylene ionomers. These ethylene ionomers are copoly(ethylene-methacrylic acid) with an acid content of 0.054 and various degrees of neutralization (E-0.054MAA-xNa): circles are observed data; (A), ○: $x = 0.82$, (B), ◑: 0.73, (C), ◐: 0.55, and (D), ●: 0.44.

this study are shown in Table 2. The size and distance of the ionic aggregates in the ionomers with a monovalent cation, sodium salts of ethylene ionomers, increase with the ion content (acid content degree of neutralization), and on the other hand, those with a divalent cation, i.e. zinc salts of ethylene ionomers, are

Table 2. The values of V_p, R_1, and $2R_{ca}$, determined by the curve fitting method for ethylene ionomers with acid content = 0.054, E-0.054MAA-xM and 0.035, E-0.035MAA-xM (x is degree of neutralization and M is Counter ion)

Sample	V_p (nm^3)	R_1 (nm)	$2R_{ca}$ (nm)
E-0.054MAA-0.82Na	22.0	0.69	2.10
E-0.054MAA-0.67Na	15.0	0.62	1.98
E-0.054MAA-0.44Na	10.0	0.53	1.70
E-0.035MAA-0.80Na	30.0	0.71	2.22
E-0.035MAA-0.70Na	23.0	0.66	2.14
E-0.035MAA-0.44Na	14.0	0.55	1.74
E-0.054MAA-0.78Zn	10.0	0.41	1.50
E-0.054MAA-0.57Zn	10.0	0.44	1.46
E-0.054MAA-0.32Zn	10.0	0.43	1.34
E-0.035MAA-0.83Zn	15.0	0.42	1.58
E-0.035MAA-0.64Zn	16.0	0.43	1.56
E-0.035MAA-0.49Zn	10.0	0.43	1.44

slightly changed, and suggests an increase in the number of ionic aggregates with almost similar size. The structure of ionic aggregates was found to be affected markedly by the coordination number of the cation aggregated.

2.3. ^{13}C NMR of ethylene ionomers

The characteristics of the physical properties and ionic aggregates in the ethylene ionomers have been outlined in the previous sections. The application of solid-state high-resolution ^{13}C NMR spectroscopy to the structural analysis of ethylene ionomers[33–37] is described in this section. One of the advantages of ^{13}C NMR is to simultaneously obtain information from all phases of ethylene ionomers, i.e. crystalline, amorphous, and ionic aggregate phases.

^{13}C CP/MAS NMR spectra of the ethylene ionomers in the aliphatic carbon region are shown in Fig. 6 together with the spectrum of LDPE as a reference. The ^{13}C NMR signals of the methylene carbons in the crystalline and amorphous regions were independently observed at about 33 and 31 ppm, respectively. The peaks of the non-protonated and methyl carbons appear at about 45 and 15 ppm, respectively. In the zinc salt of ethylene ionomer, the signal at about 45 ppm was split into two peaks, indicating neutralization with zinc. On the other hand, the relative peak intensities of the amorphous methylene carbons in ethylene ionomers were larger than that in LDPE, reflecting the degree of crystallinity: i.e. the crystallinity of the ethylene ionomers is lower than that of LDPE. The relative intensities of the crystalline and amorphous peaks obtained from ^{13}C DD/MAS NMR experiments (using only high-power dipolar decoupling, namely a single pulse-method) at various temperatures give values that are closer to the exact crystallinities of ethylene ionomers than those determined from CP experiments.

In Section 2.1, it was mentioned that the crystalline phase in the ethylene ionomer could be distinguished as consisting of two types corresponding with the endothermic DSC peaks at low and high temperatures. As the lower temperature peak was attributed to the melting of the crystallites formed by annealing, the total crystallinity of ethylene ionomers at certain temperatures cannot be determined exactly by DSC. Figure 7 shows the temperature dependence of the crystallinity for ethylene ionomers determined using ^{13}C DD/MAS NMR. The crystallinity decreases with increasing neutralization, in other words, with the ionic aggregates, similar to the conclusion of the DSC study mentioned above. Moreover, in higher neutralization samples, there is a tendency for the temperature dependence of the crystallinity to become large before the melting temperature is reached. These findings show that the quantity of the isothermal crystalline part increases with the ionic aggregates. It is concluded that the morphology of the ethylene matrix and the ionic aggregates are affected by each other.

Similar interpretations of the crystal size of zinc salts of ethylene ionomers were obtained in discussions about ^{1}H spin-diffusion with ^{1}H spin-lattice relaxation times in the laboratory (T_1^H) and rotating ($T_{1\rho}^H$) frames. Table 3

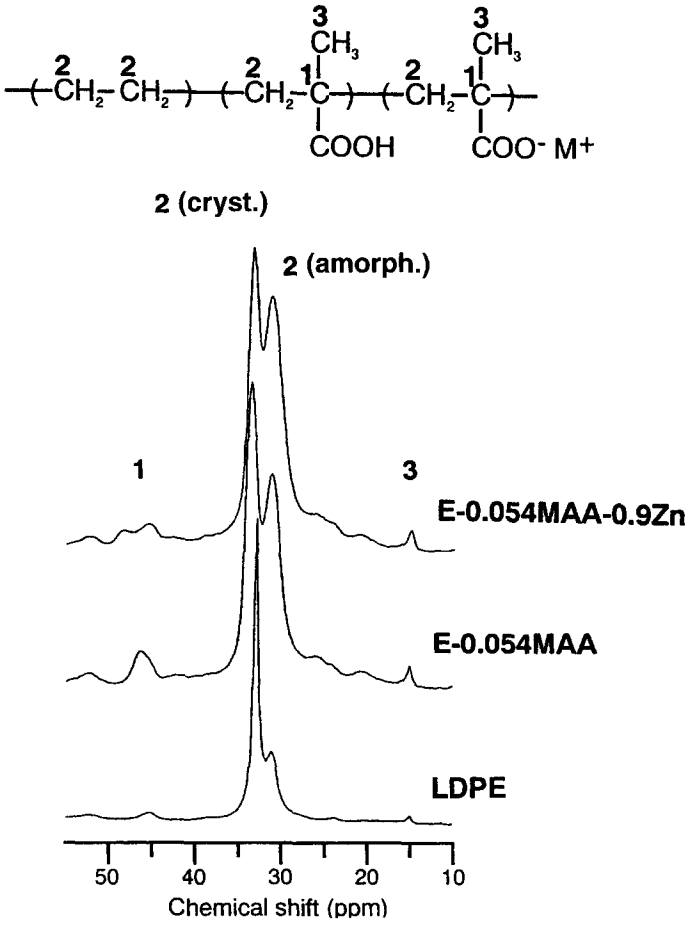

Fig. 6. ^{13}C CP/MAS NMR spectra of low-density polyethylene (LDPE), copoly(ethylene-methacrylic acid) with acid content of 0.054 (E-0.054MAA), and its zinc salt ionomer with a degree of neutralization of 0.9 (E-0.054MAA-0.9Zn) in the aliphatic carbon region at room temperature.

summarizes the results of T_1^H and $T_{1\rho}^H$ data for the methylene carbons in zinc salts of ethylene ionomers. The values of the crystalline and amorphous methylene carbons in LDPE are different from each other in both T_1^H and $T_{1\rho}^H$, indicating that the size of crystallite in LDPE is larger than about 600–690 Å. Those in the ethylene ionomers stood at room temperature for a long time are almost the same in T_1^H but different in $T_{1\rho}^H$. This means that the size of the crystallites in the ionomer is mainly in the range of several hundreds to tens of Å. However, there is a tendency for the values of T_1^H for the crystalline and amorphous methylene carbons in the sample annealed at 80 °C for 78 hours to become different, indicating an increase of crystallite due to annealing. This is

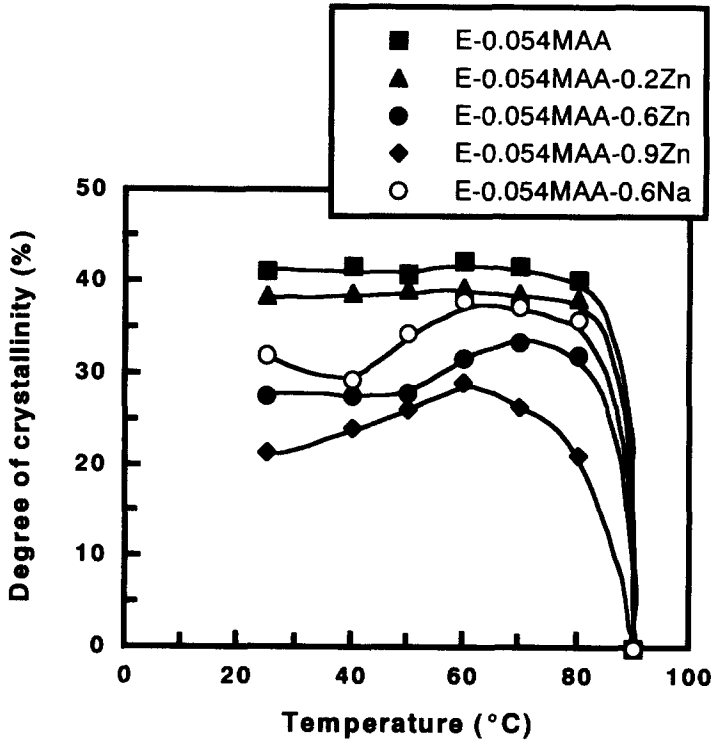

Fig. 7. The temperature dependence of the degree of crystallinity for the copoly(ethylene-methacrylic acid) and its zinc or sodium salt ionomers. The abbreviations of samples in inserted notations are the same as those of Figs 2–6.

Table 3. ^{1}H spin-lattice relaxation times, T_1^H, and spin-lattice relaxation times in the rotating flame, $T_{1\rho}^H$, of low density polyethylene (LDPE) and the zinc salt ethylene ionomers (E-0.054MAA-0.9Zn and E-0.054MAA-0.9Zn-ann*)

	T_1^H (ms)		$T_{1\rho}^H$ (ms)	
Sample	Cryst.	Amorph.	Cryst.	Amorph.
LDPE	752	812	5.79	2.75
E-0.054MAA-0.9Zn	625	623	7.78	5.81
E-0.054MAA-0.9Zn-ann	624	592	7.06	4.27

* Annealing: at 80 °C for 78 hours.
** ^{1}H spin diffusion coefficient, D is ca. 10^{-12} cm^2 s^{-1}.
From the equation, $L = (6Dt)^{1/2}$,
T_1^H (600–800 ms): L = about 600–690 Å,
$T_{1\rho}^H$ (3–6 ms): L = about 40–60 Å.

one piece of evidence for the existence of an isothermally crystallizable part in ethylene ionomers, and coincident with the results obtained by other means such as DSC, XRD and DMS.

Next, the ^{13}C spin-lattice relaxation time, T_1^C at room temperature was measured by Torchia's method.[38] Fig. 8 shows the ^{13}C magnetization recovery curves of the crystalline and amorphous methylene carbons in ethylene ionomers and LDPE. The signal from the amorphous methylene carbons shows a single exponential decay, but that from the crystalline ones show a multi-exponential decay, indicating that a distribution of mobilities exists for the crystalline region. The value of T_1^C for the crystalline methylene carbons in ethylene ionomers is smaller than that for LDPE, and this time becomes long upon annealing at 80 °C for 78 hours. These results suggest that the size of the crystallite in ethylene ionomers is relatively smaller than that in LDPE; its distribution is relatively wide; and the crystallites in ethylene ionomers increase upon annealing. As mentioned above, the high-order structures of the polyethylene matrix in ethylene ionomers can be characterized by means of high-resolution solid-state ^{13}C NMR spectroscopy.

The discussions on structure and mobility of the ionic aggregates in ethylene ionomers are based upon ^{13}C NMR signals, that is, the carbonyl carbon's signals. Figure 9 shows ^{13}C CP/MAS NMR spectra of carbonyl carbons in zinc and sodium salts of ethylene ionomers. In zinc salt ethylene ionomers, two signals are obviously measured at about 185 and 189 ppm, and their relative intensities change with the degree of neutralization. The high-frequency peak increases with increasing neutralization; low-frequency peak decreases with increasing neutralization. Therefore, these two peaks observed at low and high frequencies are assigned to the carbonyl carbons in the carboxylic acid and carboxylate anion types in the ethylene ionomers, respectively. In other words, the low- and high-frequency peaks are attributed to the carbonyl carbons non-neutralized and neutralized with the zinc cation, respectively. Asada *et al.* reported that the ^{13}C NMR chemical shifts of carbonyl carbons in poly(methacrylic acid) which were hydrogen-bonded appear at 180–187 ppm.[39] According to their assignments, the

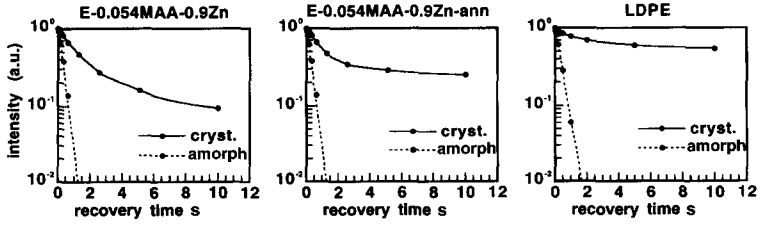

Fig. 8. ^{13}C magnetization recovery curves of the crystalline and amorphous methylene carbons in zinc salt of ethylene ionomers after ageing at room temperature for a long time (E-0.054MAA-0.9Zn) and annealing at 80 °C for 78 hours (E-0.054MAA-0.9Zn-ann), and low-density polyethylene (LDPE) at room temperature.

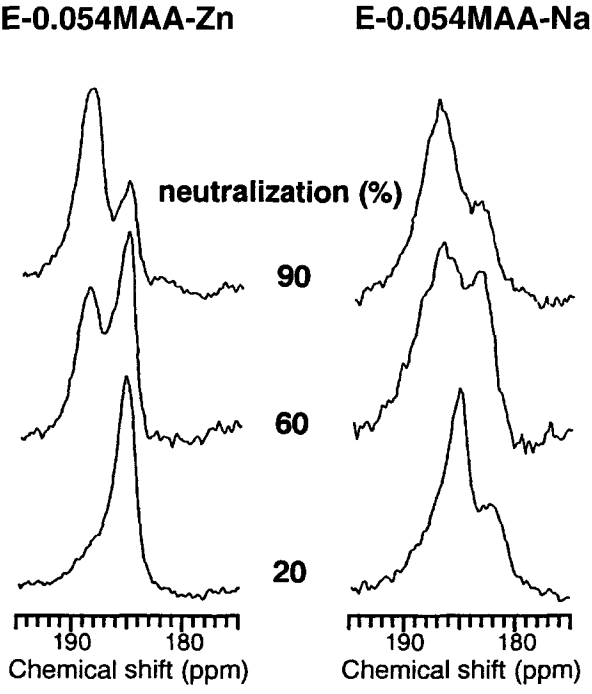

Fig. 9. ^{13}C CP/MAS NMR spectra of zinc and sodium salt ethylene ionomers (E-0.054MAA-Zn and E-0.054MAA-Na) with degrees of neutralization of 20, 60 and 90% in the carbonyl carbon region at room temperature.

observed carbonyl carbon peaks at 185 ppm for ethylene ionomers originate from the hydrogen-bonded carboxylic acid dimer. The chemical shift value of the high-frequency peak (at 189 ppm) agrees with the report for the zinc salt of poly(methacrylic acid).[39] The ^{13}C CP/MAS NMR signals of carbonyl carbons were measured at various temperatures and it was observed that the peak shapes become considerably broadened with increasing temperature, because their mobility becomes high close to the dipolar-decoupling frequency of around 60 kHz. The broadening temperature of the high-frequency peak was greater than that of the low-frequency peak. This suggests that the mobility of the carbonyl carbon in the ionic aggregates is restricted in comparison with that in the hydrogen-bonded carboxylic acid dimer.

On the other hand, the ^{13}C CP/MAS NMR spectra of carbonyl carbons in a sodium salt of ethylene ionomers are relatively confusing, i.e. the signals which should be assigned to be *C*OO-Na at high frequency, shift from about 181 ppm to 187 ppm as the degree of neutralization increases. This finding shows that the fine structures of the ionic aggregates in sodium salt ethylene ionomers, such as bond length, angle; and its distribution, etc., are probably changed by increases in the ionic aggregates. From the ^{13}C CP/MAS NMR chemical shift, the differences obtained when using the various metal cation types in ethylene

ionomers can be detected, and the interpretations derived from this viewpoint are consistent with those of the SAXS study mentioned above.

2.4. Multinuclear NMR of ethylene ionomers

The multinuclear NMR technique is a powerful tool for investigating the structure and dynamics of ionic aggregates in ionomers; obtaining the NMR signals of metal cations in ionomers as particularly useful. In this section, some results of ^{23}Na[40,41] and ^{113}Cd[42,43] NMR on ethylene ionomers are described. In general, NMR experiments can easily be carried out on these two nuclei because of their high NMR sensitivity.

Figure 10 shows the ^{23}Na MAS NMR spectra of some sodium salt ethylene ionomers at room temperature. A broad peak at about -10 to 12 ppm is clearly observed for all samples. The ^{23}Na NMR spectra of the styrene ionomers have been reported[44] (details are given in the next section, see Fig. 14). Peaks are observed at about 7, 0, and -12 to -23 ppm, which are assigned to isolated ion pairs, hydrated ions and aggregated ions respectively. The sodium cations in ethylene ionomers, therefore, are almost in ionic aggregates. The isolated ion pairs

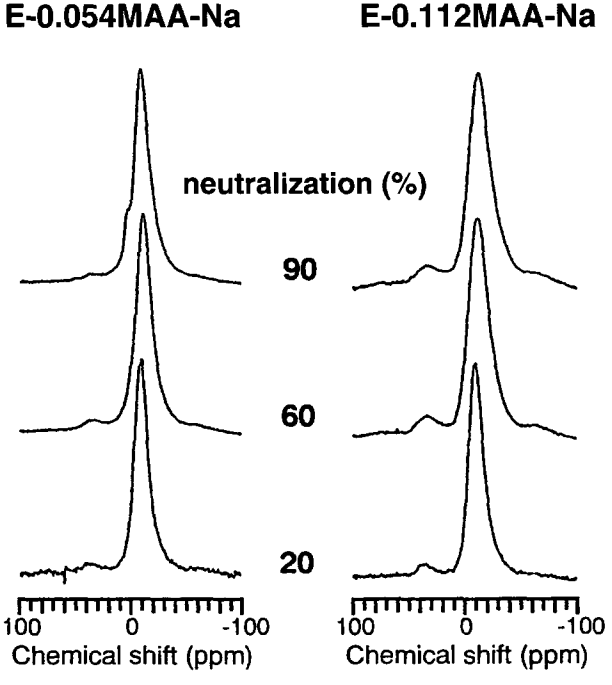

Fig. 10. ^{23}Na MAS NMR spectra of sodium salt of ethylene ionomers (E-0.054MAA-Na and E-0.112MAA-Na) with degrees of neutralization of 20, 60 and 90% at room temperature.

are observed in fully dried styrene ionomers with a low ion content, but in the dried sodium salt ethylene ionomers, they are not observed even at a very low ion content. It is suggested that the ionic aggregates with sodium cations in ethylene ionomers are easily formed compared with those in the styrene ionomers. This is coincident with the results of SAXS analysis, and suggests easier formation of ionic aggregates for the ethylene ionomer than for the styrene ionomer, because of the greater flexibility of the polyethylene matrix in the ethylene ionomer.

There are tendencies for the position of a peak to shift to low frequency, the peak to become broad, and the value of T_1 to become short, with an increase in the degree of the neutralization, as shown in Fig. 10. These findings are consistent with the fact that the ionic aggregates increase with neutralization of sodium salt ethylene ionomers. Figure 11 shows the ^{23}Na MAS NMR spectra of the sodium salt ethylene ionomer at various temperatures. The same tendencies can be seen upon increasing the temperature. The ^{13}C NMR results show that the mobility of ionic aggregates becomes large at high temperatures. Although the mobility increases, the peak width increases with temperature, indicating that the peak width of the ^{23}Na in the ionomer mainly corresponds to the distribution of its magnetic environment. As the T_1 value of ^{23}Na mainly depends on quadrupolar interactions, the finding that the T_1 of ^{23}Na in the ethylene ionomer is shorter upon increasing temperature, suggests that the variety of ^{23}Na situations in the ionic aggregates increases. Furthermore, the peak position and width and T_1 value of ^{23}Na in ethylene ionomers critically change above the melting temperature of the polyethylene matrix. From this, it can be said both that the structure and mobility of the ionic aggregates are affected by those of the polyethylene matrix.

However, since ^{113}Cd nuclei has a spin number $I = 1/2$ and high NMR sensitivity, this nucleus spin has many advantages for NMR experiments and for the investigation of ionic aggregates with divalent metal cations. In cadmium salt of ethylene ionomers, SAXS analysis has confirmed that ionic aggregates are formed.[42] The thermal properties of the polyethylene matrix in this ionomer are almost the same as those for the other ethylene ionomers. The size of the ionic aggregates of this ionomer become larger with an increase in the degree of neutralization. This is different in comparison with the other ethylene ionomers which contain divalent metal cations such as zinc.

The ^{113}Cd MAS spectra obtained with and without the CP experiment for the cadmium salt ethylene ionomer at various temperatures are shown in Fig. 12. In the CP/MAS spectra, a very broad peak is observed only at low temperatures. It can be seen that these spectra consist of several peaks appearing between about 120 and -50 ppm. It is well known that the ^{113}Cd NMR chemical shift changes widely as the type of counter anion atom is varied. The presently observed peak appears in the range of cadmium–oxygen complexes. Consequently, the broadening of this peak may be mainly caused by the very wide distribution of microstructures in the surroundings of the ^{113}Cd nuclei in the ionic aggregates. This consideration implies that the size of the ionic aggregates in the cadmium salt ethylene ionomer, as determined by SAXS, is relatively large in comparison

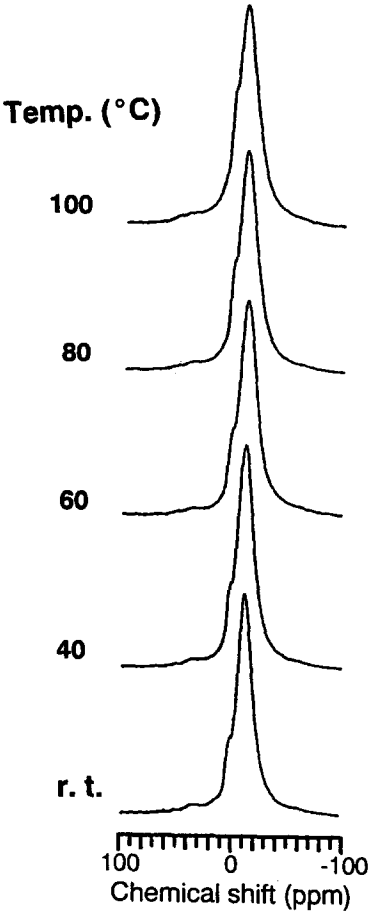

Fig. 11. ^{23}Na MAS NMR spectra of the sodium salt of ethylene ionomer with a degree of neutralization of 0.9 (E-0.054MAA-0.9Na) at various temperatures.

with the others. At higher temperatures, this CP/MAS peak disappears, indicating that the mobility of the ^{113}Cd nuclei close to the dipolar decoupling frequency and/or the CP efficiency becomes too low to detect the CP signals because of the high mobility of ^{1}H nuclei in the surroundings of the ^{113}Cd. That is, the ionic aggregates in the cadmium salt ethylene ionomers lead to a mobile state from an immobile one by heating.

On the contrary, the ^{113}Cd MAS NMR spectra obtained without the CP experiment are observed only at high temperatures, and the widths of the observed peaks are relatively narrow compared with those from the CP/MAS experiment. In addition, the ^{113}Cd NMR chemical shift changes with temperature. These findings indicate that the mobility of the ionic aggregates is high at higher temperatures. The T_1 value of ^{113}Cd is probably too large to

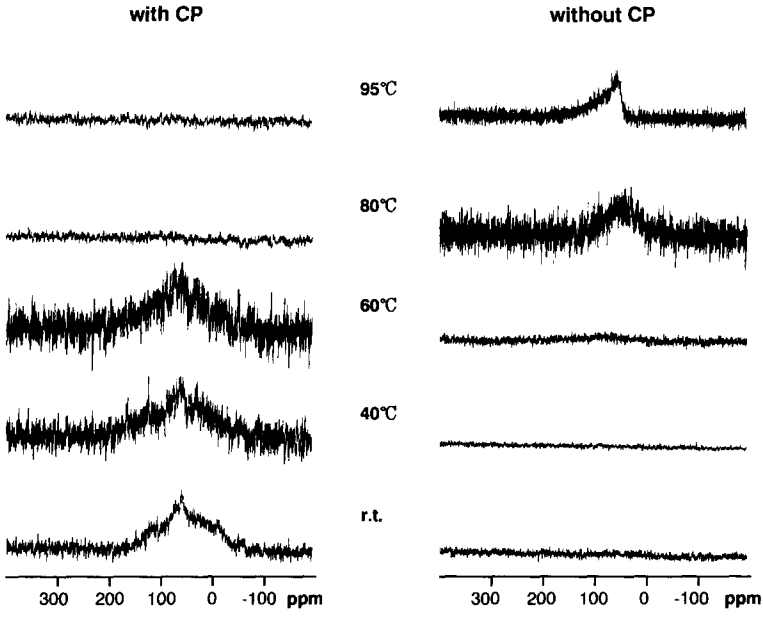

Fig. 12. ^{113}Cd MAS NMR spectra of the cadmium salt of ethylene ionomer with a degree of neutralization of 1.0 (E-0.054MAA-1.0Cd) with and without CP experiment at various temperatures. All spectra were obtained using high-power ^{1}H decoupling and a repetition time of 10 s. A contact time of 6 ms was used in the CP experiment.

observe the ^{113}Cd NMR spectrum under the experimental condition of a short repetition time (10 s) at lower temperatures. At higher temperatures, the T_1 value of ^{113}Cd is shortened by the high mobility; as a result, the spectrum can be observed. The very wide distribution of microstructures in the surroundings of the ^{113}Cd nuclei in the ionic aggregates is to some extent averaged by the high mobility, thus the line width becomes relatively small. Furthermore, the apparent chemical shifts originate from a change of the time-averaged structure, in other words, a change in the mobility of the ionic aggregates at each temperature.

3. OTHER IONOMERS

3.1. Styrene ionomers

Polystyrene-based ionomers have no crystalline phase in a host polymer matrix. Figure 13 shows a schematic model of the styrene ionomer (compare with Fig. 1). One of the characteristics of styrene ionomers is that, in addition to the ionic aggregates, there are also some isolated ion pairs distributed throughout the polystyrene matrix, which do not contribute to the crosslinking of the polystyrene chains.

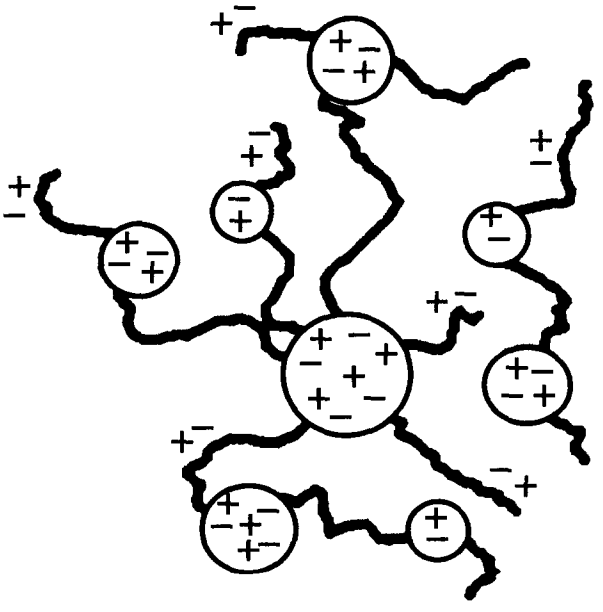

Fig. 13. Structure model of the styrene ionomers.

Cooper *et al.* reported that solid-state ^{23}Na NMR is useful for observing the sodium cation in sulfonated polystyrene ionomers (NaSPS).[44] Three NMR peaks were detected, corresponding to isolated ion pairs, aggregated ions and hydrated ions (Fig. 14). The distributions of these three types of sodium cations are systematically influenced by hydration treatment, sulfonation level and neutralization level. Fully dried NaSPS at low ion content shows that the isolated and aggregated sodium ions in NaSPS are available for hydration. As the sulfonation level increases, the fraction of sodium ions held in isolated ion pairs decreases while the fraction of ionic species in the ionic aggregates increases. This coincides with a shift in the peak position of the aggregated sodium ions to low frequency, indicative of increased quadrupolar interactions.

To probe the local mobility of the chain segments directly attached to ionic aggregates, Laupretre *et al.* synthesized two model ionomers and studied them by means of ^{13}C CP/MAS NMR.[45] The first one is a carboxylate-telechelic deuterated polystyrene in which the chain segments bearing the sodium caroxylate end groups have been selectively protonated (DHD); the second one has a protonated polystyrene backbone terminated at both ends with a deuterated polystyrene segment bearing the sodium carboxylate groups (HDH). Through the CP experiment, the ^{13}C NMR signals of protonated carbons are emphasized compared with those of the deuterated ones. Therefore, the ^{13}C NMR signals from nuclei both near to and far from the ionic aggregates are obtained by using HDH and DHD, respectively. Linewidth measurements of the protonated units have clearly shown that the dipolar interactions of the sodium carboxylate end

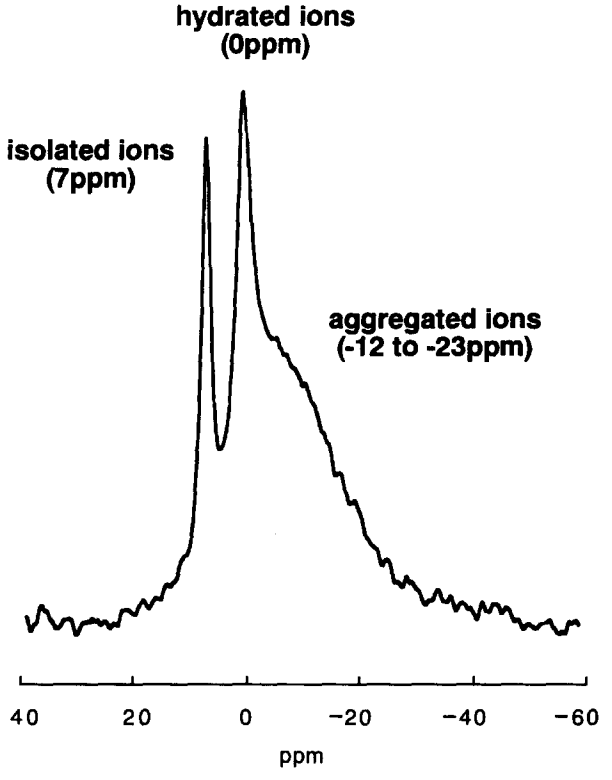

Fig. 14. ^{23}Na MAS NMR spectrum of NaSPS with an acid content of 1.7%. This ionomer was exposed to the atmosphere before the experiment.

groups are responsible for a mobility restriction of the chain end segments. This experiment, which is thought to be the first direct evidence for the model, was proposed by Eisenberg *et al.*[46] for an ionomer morphology according to which the ionic aggregates are surrounded by a shell of constrained polymer segments.

3.2. Polymer blends with ionomers

Many ionomers are used in polymer blends as a compatibilizer, because the ionomers have at least two different properties, that is, hydrophobic host–polymer matrix and hydrophilic ionic groups and/or aggregates. In addition, the solution properties of mixtures including the ionomers have also been investigated to clarify the details of characteristics not only in blending but also in micellar structures. For example, Bosse and Eisenberg recently reported on the kinetics of coil overlap in ionomer blends in DMSO by means of ^{1}H NMR.[47,48]

Weiss *et al.* reported details of polymer blends by using the ionomers studied by means of solid-state NMR. In order to characterize polystyrene and

polyamide blends using a NaSPS, they applied solid-state ^{15}N NMR.[49] In this polymer blend system, the metal sulfonate groups, which aggregate in the neat ionomer, are dispersed by the polyamide in the blend as a consequence of a complexation that involves the sulfonate cation and both the carbonyl oxygen and the amide nitrogen of the polyamide. The ^{15}N CP/MAS NMR spectra were consistent with a 2p electron redistribution model for the complex, in which electrons migrate from the nitrogen to the metal ion through the carbonyl group. The crystallinity of the polyamide component and the morphologies of the phase-separated blend samples were investigated by solid-state ^{13}C and ^{1}H NMR techniques which include multipulse irradiation, CP, and MAS.[50]

The microphase structure and mechanical properties of the blends containing neat acrylonitrile-butadiene-styrene copolymer (ABS), styrene-acrylonitrile copolymer (SAN) and sodium sulfonated SAN ionomer have been investigated as a function of ion content of the ionomer in the blend by Park *et al.*[51] The interfacial adhesion was quantified by ^{1}H NMR solid echo experiments. The amount of interphase for the blend containing the SAN ionomer with low ion content (3.1 mol%) was nearly the same as that of ABS, but it decreases with the ion content of the ionomer for the blend with an ion content greater than 3.1 mol%. Changing the ionomer content in the blends shows a positive deviation from the rule of mixtures in tensile properties of the blends containing the SAN ionomer with low ion content. This seems to result from the enhanced tensile properties of the SAN ionomer, interfacial adhesion between the rubber and matrix, and the stress concentration effect of the secondary particles.

4. CONCLUSIONS

This chapter shows that NMR spectroscopy is a powerful tool for the structural analysis of ionomers. Ionomers are already widely used in various fields of application. In the near future, it is expected that research on the physical, mechanical, electrical, and transport properties of ionomers using NMR techniques will increase.

REFERENCES

1. L. Holiday, *Ionic Polymers*, Applied Science, London, 1975.
2. A. Eisenberg and M. King, *Ion-Containing Polymers: Polymer Physics and Structure*, Academic Press, New York, 1977.
3. R. Longworth, in *Developments in Ionic Polymers 1* (eds D. Wilson and H. J. Prosser), Applied Science, London, 1983, Chapter 3.
4. M. Pineri and A. Eisenberg, *Structure and Properties of Ionomers*, NATO ASI Series, D. Reidel, Dordrecht, 1987.
5. R. Longworth and D. J. Vaughan, *Nature*, 1968, **218**, 85.
6. W. J. MacKnight, L. W. McKenna and B. E. Read, *J. Appl. Phys.*, 1967, **38**, 4208.
7. C. L. Marx and S. L. Cooper, *Makromol. Chem.*, 1973, **168**, 339.
8. W. J. MacKnight, W. P. Taggart and L. McKenna, *J. Polym. Sci., Symposium*, 1974, No. 46, 83.

9. T. Kajiyama, T. Oda, R. S. Stein and W. J. MacKnight, *Macromolecules*, 1971, **4**, 198.
10. B. Wunderlich, *Macromolecular Physics*, Volume 3, p. 286, Academic Press, New York, 1976.
11. C. L. Marx and S. L. Cooper, *J. Macromol. Sci. Phys.*, 1974, **B9**, 19.
12. M. Kohzaki, Y. Tsujita, A. Takizawa and T. Kinoshita, *J. Appl. Polym. Sci.*, 1987, **33**, 2393.
13. K. Tadano, E. Hirasawa, Y. Yamamoto, H. Yamamoto and S. Yano, *Jpn. J. Appl. Phys.*, 1987, **26**, L1440.
14. K. Tadano, E. Hirasawa, H. Yamamoto and S. Yano, *Macromolecules*, 1989, **22**, 226.
15. E. Hirasawa, Y. Yamamoto, K. Tadano and S. Yano, *Macromolecules*, 1989, **22**, 2776.
16. R. A. Register and S. L. Cooper, *Macromolecules*, 1990, **23**, 318.
17. Y. Tsujita, K. Shibayama, A. Takizawa and T. Kinoshita, *J. Appl. Polym. Sci.*, 1987, **33**, 1307.
18. H. Okumura, H. Yoshimizu, Y. Tsujita and T. Kinoshita, *Polym. Preprints Jpn*, 1994, **43**, 1304.
19. R. E. Prud'homme and R. S. Stein, *Macromolecules*, 1971, **4**, 668.
20. W. J. MacKnight and T. R. Earnest, Jr., *J. Polym. Sci. Macromol. Rev.*, 1981, **16**, 41.
21. S. Nakamura, H. Yoshimizu, M. Takei, Y. Tsujita and T. Kinoshita, *Polym. Preprints Jpn*, 1993, **42**, 1365.
22. for example; D. Brun, P. Tormala and G. Weber, *Polymer*, 1978, **19**, 598.
23. D. J. Yarusso and S. L. Cooper, *Macromolecules*, 1983, **16**, 1871.
24. D. L. Handlin, W. J. Macknight and E. L. Thomas, *Macromolecules*, 1981, **14**, 795.
25. C. E. Williams, C. Colliex, J. Horrion and R. Jerome, *Multiphase Polymers: Blends and Ionomers*; L. A. Utracki and R. A. Weiss, eds, *ACS Symposium Series* 395, American Chemical Society, Washington DC, 1989, Chapter 18.
26. C. L. Marx, J. A. Koutsky and S. L. Cooper, *J. Polym. Sci. Polym. Lett. Ed.*, 1971, **9**, 167.
27. P. J. Philips, *J. Polym. Sci. Polym. Lett. Ed.*, 1972, **10**, 443.
28. C. L. Marx, D. F. Caulfield and S. L. Cooper, *Macromolecules*, 1973, **6**, 3.
29. S. Kumar and M. Pineri, *J. Polym. Sci. Polym. Phys. Ed.*, 1986, **24**, 1767.
30. Y. S. Ding, S. R. Stevan, K. O. Hodgson, R. A. Register and S. L. Cooper, *Macromolecules*, 1988, **21**, 1698.
31. Y. Tsujita, M. Yasuda, M. Takei, T. Kinoshita, A. Takizawa and H. Yoshimizu, *Macromolecules*, 2001, **34**, 2220.
32. D. J. Yarusso, S. L. Cooper, G. S. Knapp and P. Georgopoulos, *J. Polym. Sci. Polym. Lett. Ed.*, 1980, **18**, 557.
33. Y. Murata, H. Yoshimizu, Y. Tsujita and T. Kinoshita, *Polym. Preprints Jpn*, 1994, **43**, 1305.
34. H. Yoshimizu, Y. Murata, Y. Tsujita and T. Kinoshita, *Proc. ISF '94 Preprint*, 1994, 349.
35. K. Sogabe, Y. Suzuki, H. Yoshimizu, Y. Tsujita and T. Kinoshita, *Polym. Preprints Jpn*, 1995, **44**, 731.
36. H. Yoshimizu, Y. Tsujita and T. Kinoshita, *33rd Meeting on NMR*, Kobe, 1994, p. 233.
37. K. Sogabe, Y. Suzuki, H. Yoshimizu, Y. Tsujita and T. Kinoshita, *34th Meeting on NMR*, Tsukuba, 1995, p. 237.
38. D. A. Torchia, *J. Magn. Reson.*, 1978, **30**, 613.
39. M. Asada, N. Asada, A. Toyota, I. Ando and H. Kurosu, *J. Mol. Struct.*, 1991, **244**, 237.
40. K. Sogabe, H. Yoshimizu, T. Kinoshita and Y. Tsujita, *35th Meeting on NMR*, Kyoto, 1996, p. 152.
41. K. Sogabe, H. Yoshimizu, Y. Tsujita and T. Kinoshita, *Polym. Preprints Jpn*, 1997, **46**, 821.
42. H. Sugiura, H. Yoshimizu, Y. Tsujita and T. Kinoshita, *Polym. Preprints Jpn*, 2000, **49**, 403.
43. H. Sugiura, H. Yoshimizu, Y. Tsujita and T. Kinoshita, *39th Meeting on NMR*, Tokyo, 2000, p. 358.
44. E. M. O'Connell, T. W. Root and S. L. Cooper, *Macromolecules*, 1994, **27**, 5803.
45. P. Vanhoorne, R. Jerome, P. Teyssie and F. Laupretre, *Macromolecules*, 1994, **27**, 2548.
46. A. Eisenberg, B. Hird and R. B. Moore, *Macromolecules*, 1990, **23**, 4098.
47. F. Bosse and A. Eisenberg, *Macromolecules*, 1994, **27**, 2846.
48. F. Bosse and A. Eisenberg, *Macromolecules*, 1994, **27**, 2853.
49. Y. Feng, A. Schmidt and R. A. Weiss, *Macromolecules*, 1996, **29**, 3909.
50. D. L. VanderHart, Y. Feng, C. C. Han and R. A. Weiss, *Macromolecules*, 2000, **33**, 2206.
51. J. W. Lee, C. H. Kim, J. K. Park and T. S. Hwang, *Polym. Int.*, 1998, **45**, 47.

Applications of NMR Techniques to Coal Science

KOJI SAITO, KOJI KANEHASHI AND IKUO KOMAKI

Advanced Technology Research Laboratories, Nippon Steel Corporation, 20–1 Shintomi-chou Futtsu City, Chiba, 293–8511, Japan

1. INTRODUCTION AND REVIEW OF NMR WORK IN COAL SCIENCE

Coal[1] is considered to be a heterogeneous organic rock and is typically black in colour, although, deposits can range in colour from brown to brownish red. It is formed by the accumulation of plant debris that has been altered over geological time by the action of biological, chemical, and physical (heat and pressure) degradation processes. The relative quantities of remaining plant parts and the degree of their thermal maturation and degradation result in coals with varied properties. Coals may be classified as banded (humic coals) or non-banded (cannel or boghead coals), are hard or soft, or can vary in rank from brown coal, through lignite, subbituminous, bituminous to anthracite. The degree of thermal maturation of plant matter, or coalification, is referred to as *rank*.

ANNUAL REPORTS ON NMR SPECTROSCOPY
VOLUME 44 ISBN 0-12-505344-4

The evolution of coal, the enormous variation found in its composition, its microheterogeneity, and its differentiation towards chemical reactions suggest that coal is a complex mixture of compounds. While this is true, however, there is some order to its inherent, overall structure. There are microscopically discrete, optically homogeneous aggregates of organic materials derived from the various plant parts that constitute coal. These individual domains are referred to as *macerals*.[2,3] There are three major maceral groups having their own distinct set of properties and selective chemistries, respectively. The most abundant of the macerals found in coals is vitrinite, which is derived from the woody tissue of plants and is a largely lignin-based polymer. The group of macerals called liptinite may be derived either from waxy leaf cutin, parts of spores and pollen, or algal bodies. This group of macerals tends to be composed of highly aliphatic macerals. The last maceral group, inertinite, is named for its relative unreactivity in most chemical reactions. It is derived from material that has undergone extensive oxidation or that is a form of fossilized charcoal derived from primordial forest fires. The inertinite macerals have a high degree of aromatic character. Apart from the organic components, there may be substantial quantities of water and mineral matter present in coal. The minerals can be varied and also rather complex in composition; hydrated aluminosilicates, clay minerals, quartz, sulfides, sulfates, pyrite and carbonates have been identified, to name a few. The main elemental constituents of coals, therefore, are carbon, hydrogen and oxygen, with varying amounts of nitrogen and sulfur, and lesser amounts of silicon, calcium, aluminium, iron, magnesium, sodium, and other trace elements. Given this diversity of chemistry and elemental composition, coals have been a rich source for study by NMR techniques.

Applications of NMR spectroscopy to the study of coals have experienced extraordinary growth since the inception of the technique in 1946.[4] Early experiments focused on the application of broadline ^{1}H NMR spectroscopy to coal research. High-resolution liquid state ^{1}H NMR proved to be an extremely useful structure elucidation tool for coal extracts and liquefied conversion products in subsequent years. The earliest report on the use of broadline ^{1}H NMR in coal research was published in 1955 by Newman *et al.*[5] However, apart from demonstrating that the NMR experiment was feasible on such materials, little chemical information was gleaned from this original work. It was more than 20 years later, in 1976, when the first solid-state ^{13}C NMR spectra appeared in the literature,[6] utilizing the then recently developed CP methods for sensitivity enhancement together with strong proton decoupling.[7] These initial ^{13}C spectra, recorded for four coal samples of different rank, are shown in Fig. 1. It was the first time that coal structure was determined by a direct method for whole coals in their native state. Less than a year later, magic-angle spinning (MAS) with respect to the static magnetic field, was used in combination with CP and proton decoupling to produce the first high-resolution solid ^{13}C CP/MAS spectra of coal.[8] This constituted a major

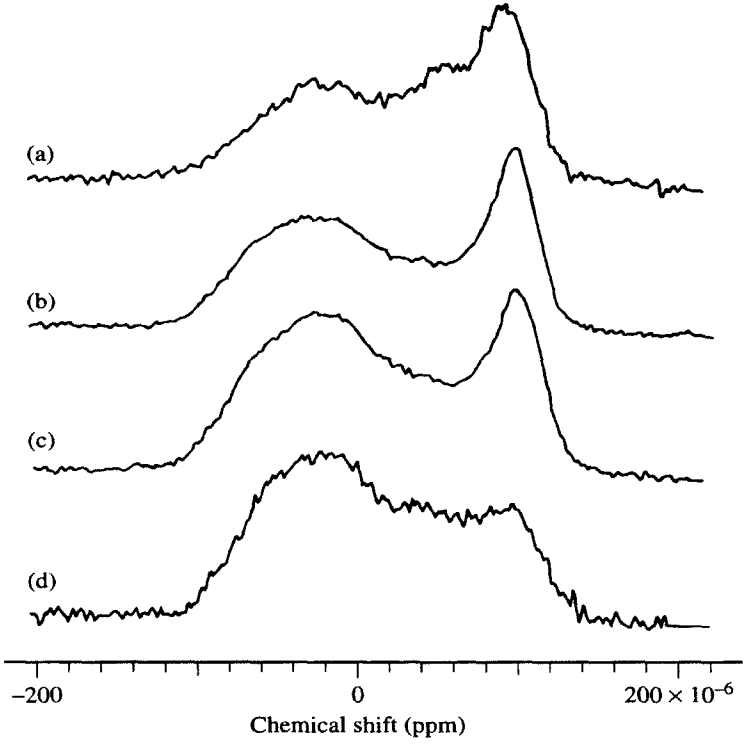

Fig. 1. ^{13}C CP NMR spectra of coals of increasing rank (reported by Dr R. E. Botto in *Encyclopedia of NMR* John Wiley, New York, 1996, p. 2105).

breakthrough in the field; removing broadening effects arising from both CSA and ^{1}H-^{13}C dipolar interactions produced isotropic resonance lines and facilitated the analysis of different carbon functional groups in coals. Early ^{13}C CP spectra of coals (see Fig. 1) exhibited two broad, overlapping resonance bands that could be assigned to regions of aliphatic (0–60 ppm) and aromatic (30–250 ppm) carbon atoms. From these spectra, the fractional carbon aromaticities (fa) were estimated by employing peak deconvolution methods. The results supported the classical view that coals were highly aromatic materials and that the aromaticity of coals increased with increasing rank as calculated on the basis of their carbon content. Comparing ^{13}C CSA lineshapes of coals and model compounds allowed the identification of regions of polycondensed aromatic ring structures, simple aromatic systems, aliphatic structures, and also aliphatic ether linkages. However, it was difficult to obtain estimates of these different functionalities because of the lack of resolution in the spectra.

This situation changed dramatically with the introduction of MAS in the NMR experiment to remove CSA. Narrowing of the resonances to their

isotropic chemical shift values facilitated the assignment of a host of carbon functional groups, including aromatic and alkenic carbons, carboxylic acids and other carbonyl groups, phenolic and furanyl carbon atoms, carbon-substituted aromatic carbon atoms, oxygen-substituted carbon atoms (including methoxyl groups), as well as methylene and methyl carbon atoms. Assignment for a typical high-resolution solid-state ^{13}C spectrum of a whole coal is shown in Fig. 2. First and second moments of the aromatic carbon resonance band were shown to vary as a function of the carbon content of coals ranging in rank from lignite to anthracite. The first moments were found to decrease with increasing rank, which was in accord with estimates derived from models for the increase in the aromatic ring condensation index. The second moments decreased with rank, implying that the dispersion of chemical shifts in the aromatic region was decreasing, or becoming more homogeneous with increasing carbon content of the coal. Nevertheless, interrupted decoupling solid-state NMR has provided valuable insight into the nature of coal as a macromolecular material, and the technique has been used to explain some of the chemistry occurring upon its treatment under a variety of conditions. Solid-state NMR spectroscopy has seen limited applications to the study of mineral phases in coals, since all chemical information obtained from NMR spectroscopy is averaged, although coal is considered to be a heterogeneous organic rock.

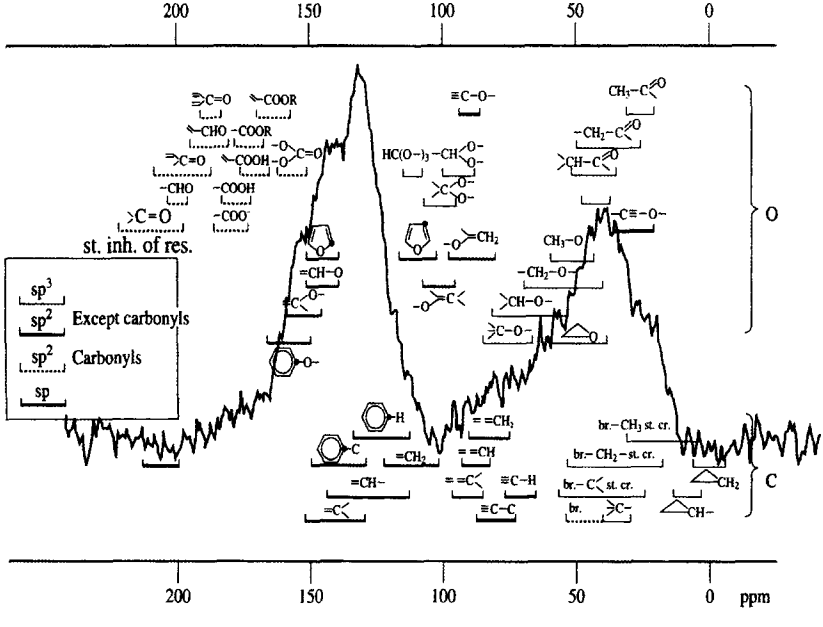

Fig. 2. ^{13}C CP/MAS spectrum of a whole coal with the NMR chemical shift correlation chart (reported by Dr R. E. Botto in *Encyclopedia of NMR* John Wiley, New York, 1996, p. 2105).

The first direct magnetic resonance imaging (MRI) experiment on solid coal and maceral specimens appeared in 1989.[9] These initial studies demonstrated the potential of MRI spatially to map proton distributions in whole coals. Individual macerals within the coals were readily distinguished by image contrast based on differences in proton density or spin-lattice relaxation. A subsequent MRI investigation focused on elucidating changes in the physical structure and on determining solvent accessibility parameters in solvent-swollen coals.[10] Other researchers have utilized MRI to determine the distribution of water in coalified woods and low-rank coals.[11] Correlation of proton spin distributions determined by MRI with the void spaces from other techniques allowed analysis of porosity and permeability in the specimens. Transient MRI studies of solvent penetration into solid coal specimens has led to a detailed understanding of transport phenomena for systems in which the glass transition is induced by solvent. The data obtained have led to the development of a new model for anomalous transport behaviour in coals.[12]

Finally, there is no doubt that energy[13] is an important commodity because it affects our lives in many ways. In the past, a direct relationship had been drawn between energy consumption and economic growth. Advancement in economic growth was shown to have a favourable impact on the quality of life in economically advanced societies by fostering better health and educational services, a robust industrial base with which to sustain future development, and various forms of labour-saving devices for common use. Often concerns about the negative impacts from economic growth, such as pollution, overpopulation, and crime have been neglected by nations striving to improve their economic status. In the rapidly changing world of the last 30 years, however, there have been escalating demands placed on global energy resources. An ever-increasing number of developing countries have competed for the existing energy supply. Environmental issues have become the highest priority in guiding the utilization of global resources. While traditional 'old-world' coals such as wood and agricultural products are still in use around the globe, they remain effective sources of energy only for less-developed societies. Alternative energy resources in the form of geothermal and hydroelectric power are limited throughout the world, while renewable resources such as solar, wind, and tidal have been slow to develop on a large commercial scale. Development of nuclear energy, once heralded as the answer to future global energy demands into the next millennium, has been severely curtailed because of apprehension about radioactive release into the environment and problems in storage of high-level radioactive wastes. Consequently, a greater burden of world energy demands over the past 30 years has centred on fossil fuels. With increasing demands on supplies worldwide, fuel quality has diminished significantly. In addition, utilization of coals as a carbon source for the production of bulk and specialty chemicals, and of high technology polymer blends and composites may be almost as important economically as their use as an energy source. Coal is playing a very important role in energy fields. The total world resources of coal

are 10^{12} tons; total world production is estimated to be 4.0×10^9 tons per year. The importance of this resource is that, despite having greater problems with production, transportation and utilization compared with oil and gas, it represents a vast resource in meeting energy demands well into the future (for more than 1000 years). From the viewpoint of energy resources, coal is a very important material for humans and NMR techniques have many advantages compared to other methods in order to analyse coal structures.

2. MULTINUCLEAR NMR SPECTROSCOPY OF COALS

2.1. ^{1}H CRAMPS

NMR techniques offer a non-destructive solid-state examination of the chemical and physical properties of coal structures. Of the NMR techniques being used for coal studies today, the most common are based on ^{13}C, using direct polarization (DP) due to ^{13}C spin-lattice relaxation or cross-polarization (CP) approaches with high-power ^{1}H decoupling and magic-angle spinning (MAS). These methods allow the observation of aliphatic and aromatic resonances separately and often provide partial resolution into additional peaks, giving more structural detail. On the other hand, ^{1}H NMR methods had not until recently been able to provide information about chemical functionality in coal, because of the line-broadening effects of strong proton–proton dipolar coupling. The recently introduced ^{1}H CRAMPS technique now provides 'high-resolution' coal spectra consisting primarily of two broad peaks: a peak due to protons attached to aliphatic carbons ('aliphatic protons') and a peak due to protons attached to aromatic-ring carbons ('aromatic protons').[14,15]

^{1}H CRAMPS spectra were obtained on a Chemagnetics CMX-300 spectrometer on Witbank and Goonyella coals. The BR-24 pulse sequence[16] was used to obtain these spectra. The coal samples were saturated with perdeuterated pyridine (100% C_5d_5N). The samples were spun with an MAS speed of 1–2.5 kHz. Lower-rank coals require smaller MAS speeds than do coals of higher aromaticity, because both spinning sideband and rotor lines[17–19] are generally less intense and a suitable baseline is typically easier to achieve for lower-rank coals. Generally it is more difficult to spin C_5d_5N-saturated samples than untreated coals, but here a system saturated with vapour was used. Spectral deconvolution of overlapped peaks was performed using standard Chemagnetics software 'Spin-Sight'. This section discusses the information on chemical functionalities present in two coals, Witbank and Goonyella, and their relative concentrations as provided by the ^{1}H chemical shift patterns in the ^{1}H CRAMPS spectra.[20]

Saturation of the sample with perdeuteropyridine often dramatically enhances the spectral resolution, making it possible to elucidate more structural details.

The effect of pyridine on coal has been the subject of substantial interest, but the exact origin of the narrowing of the ^1H CRAMPS spectra is not known with certainty. There is some difference in the aromatic regions of CRAMPS spectra between raw coal and coal with pyridine added (Fig. 3). It seems likely that the main effect is due to an enhancement of localized anisotropic motions within the structural units of coals. Such motions, although not able to average anisotropic influences (e.g. dipole–dipole interactions, chemical shift anisotropies) to zero, are able to effect a substantial degree of averaging of the various isotropic chemical shift differences (e.g. due to specific conformations) that would otherwise be locked-in by the absence of motion. Such averaging would reduce the breadth of the distribution of isotropic chemical shifts that occur in a rigid system only in terms of geometric variation. A second, and probably much smaller, effect could be the filling of voids in coal by pyridine molecules, thereby reducing the heterogeneity of the local magnetic susceptibility. Knowledge about functional groups present in coals has increased in recent years, but is still inadequate in some major respects.[21] The chemical functionality of coal has been summarized and discussed many times in the literature in terms of coal structure models.[22–24] ^{13}C NMR and ^1H NMR have been used extensively in attempts to

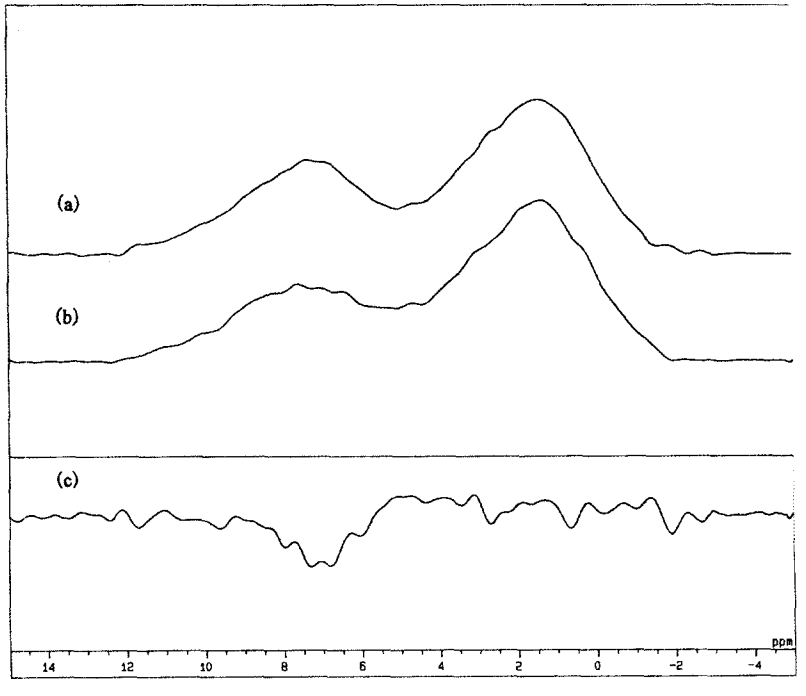

Fig. 3. ^1H CRAMPS spectra of Witbank coal: (a) raw coal; (b) C_5d_5N-saturated coal; (c) differential spectrum.

elucidate functionality in coal, e.g. the recent studies by Solum *et al.*[25] and Dela Rosa *et al.*[26] None of the authors of detailed models of coal structure or functionality has had the advantage of the availability of ^{1}H CRAMPS data in deriving such models. The ultimate analyses of Witbank coals are shown in Fig. 4 with the results of spectrum deconvolution.

Deconvolutions of the ^{1}H CRAMPS spectra of C_5d_5N-saturated coals allow the following chemical shift determined categories of chemical functionalities in coal to be identified: (1) 1.0–1.4 ppm: methyl groups β, γ to, or further from, an aromatic ring or ethoxy methyl groups; (2) 1.8–2.5 ppm: methylene groups β to an aromatic ring, tetralin-like CH_2, indene-type CH_2, hydroanthracene CH_2, alicyclic CH_2; (3) 3.5 ppm: ether methyl groups; (4) 6.8 ppm: aromatic C–H; (5) 10.5. ppm: carboxylic groups, aromatic protons, α to nitrogen within an amino-pyridine-type ring, hydroxypyridine.

The relative concentrations determined for the various chemical shift ranges shown above, display a very large diversity among typical coals. To some extent, correlations can be observed between the ^{1}H NMR-based patterns of chemical functionalities described above for the two coals and analogous patterns determined by ^{13}C CP/MAS NMR approaches. Of course, ^{13}C CP/MAS NMR studies provide much more direct evidence on carbonyl (including carboxyl)

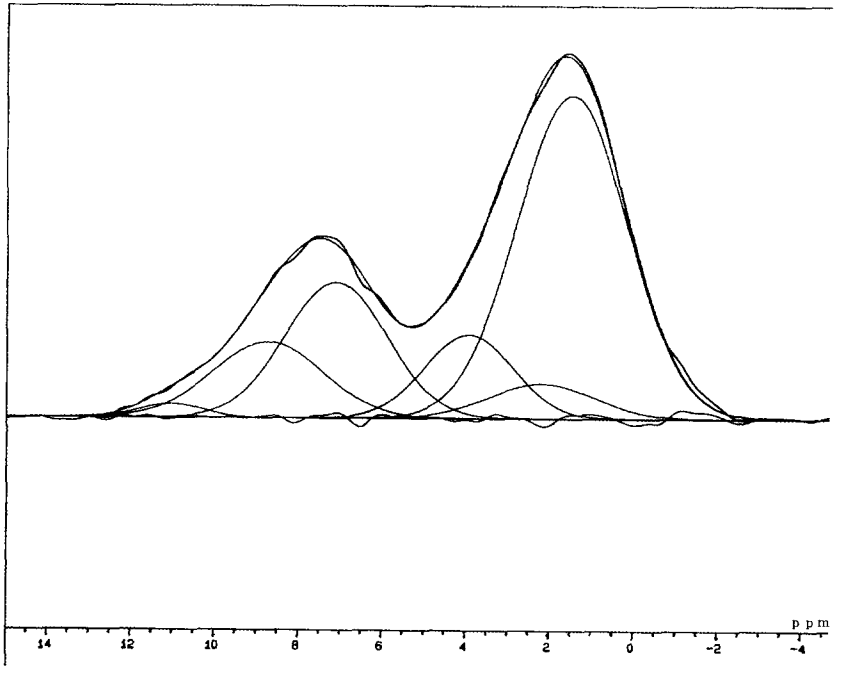

Fig. 4. ^{1}H CRAMPS spectra of Goonyella coal with deconvoluted contributions.

functionalities, but CRAMPS is very useful in order to discuss the chemical structure of coals generally, because of the relatively short measurement time compared to the case of ^{13}C CP/MAS NMR. Additionally, combination of the use of the hydrogen aromaticity and elemental analysis data could afford determination of the amount of tertiary aromatic carbon present. The parameter *Xb*, the mole fraction of aromatic bridgehead carbons in all aromatic carbons, could be derived from the above NMR data and elemental analysis of coal. *Xb* is directly correlated to the number of aromatic carbon atoms per cluster, *C*.

2.2. ^{13}C CP/MAS with spectral editing techniques

In general, ^{13}C CP/MAS techniques depend on the mathematical manipulation which is employed to enhance the resolution of solid state NMR coal spectra.[27] The several methods that have been implemented include:

(1) convolution difference spectroscopy, which uses a filtering function composed of two exponentials and an adjustable weighting constant;
(2) Gaussian multiplication, which has been used to improve resolution on the basis of lineshape modification;
(3) a variety of curve and Fourier deconvolution methods, for which the usual practice is to fit mathematically a broad band of unresolved resonances to a series of peaks that are varied according to frequency position, lineshape, linewidth and intensity.

^{13}C CP/MAS is a very powerful technique for the analysis of coal structures, but sometimes it is difficult to decide the peak assignments because of broad and overlapping peaks. Although the DEPT method[28] is useful in the solution NMR field, there is as yet no suitable application for the solid-state NMR field. As the state of the art progressed, greater emphasis was placed on obtaining specific, detailed information on the chemical functionality of coals and coal macerals. Several approaches were implemented to enhance the resolution of ^{13}C CP/MAS spectra so that greater structural information could be obtained.[27] The first, and still most utilized, spectral editing technique developed for the simplification of coal spectra was the interrupted decoupling (or dipolar dephasing) experiment[4] which was originally proposed by Alla and Lippmaa.[29] The basic approach distinguished between carbon atoms on the basis of dissimilarities in transverse relaxation times between protonated and non-protonated carbon atoms, owing to differences in the magnitudes of their ^{1}H-^{13}C dipolar couplings. In the absence of a strong proton-decoupling field, which is turned off during a finite period of time during the course of the experiment, the protonated carbon magnetization decays at a significantly faster rate than that of the non-protonated carbons. Methyl carbon atoms exhibit intermediate decay rates due to fast molecular motion. In principle, this allowed signals from these four types of carbon to be separated quantitatively,

provided that the appropriate mathematical solutions had been performed to calculate initial signal intensities from experimental decay rates in a series of variable interrupted decoupling time experiments.

Recently, spectral editing techniques developed by Wu *et al.*[30] (the pulse sequence is shown to Fig. 5), have shown remarkable effects in distinguishing between C, CH, CH_2, and CH_3 groups in the case of natural products with good signal to noise ratios (S/N). Therefore we have applied this method to complex materials, namely coals, for which the spectra have many overlapping peaks because there are many similar structures present.[31] It is clear that Wu's method (CP/MAS with TOSS, LCDP; long cross-polarization with depolarization, and SCPPI; short cross-polarization polarization inversion) is helpful in analysing structures, when the experimental conditions are optimized. In the case of CH_2 groups. In the aliphatic regions, it is easy to distinguish the CH_2 peaks among many other peaks (see Fig. 6) using the SCPPI pulse sequence. At the same time, these results give useful information for providing the deconvolution peaks with chemical shift and half-width values. These values can be fed back to assign coal peaks with much more accuracy.

2.3. ^{15}N CP/MAS

^{15}N NMR spectroscopy provides a complementary means to X-ray spectroscopic techniques[32] for identifying nitrogen-containing functional groups. This specificity is due to the large chemical shift range and sensitivity of ^{15}N to structural variations such as bond hybridization and hydrogen bonding, as recently shown for model compounds.[33] The major difficulty in employing ^{15}N NMR spectroscopy lies in its sensitivity, which is very low due to the low natural abundance (0.37%) of the ^{15}N isotope, the small magnetogyric ratio, and the low natural presence of nitrogen in coals (a few per cent). At the same time, the ^{15}N CP/MAS method requires optimized measurement conditions because of the variety of chemical structures containing nitrogen. In principle, the inherent capabilities of NMR techniques for identifying structural features and describing molecular motion have rendered this analytical method among the most powerful available for the study of condensed phases of matter. In this section, ^{15}N CP/MAS data are presented on Witbank coal.[34]

NMR spectra were obtained on a JEOL EX-400 spectrometer with a nitrogen frequency of 40 MHz employing a standard 6.5 mm rotor that contained 200 mg of sample. During the NMR experiments the samples were exposed to air, which reduces the proton T_{1H} value[35] and, thus, reduces the signal losses due to the short repetition rate employed. Line broadening at 300 Hz was applied to each of the spectra shown in Fig. 7. The spinning speed was locked at 6 kHz. The number of scans for each sample was approximately 400 000. Chemical shifts are reported on the nitromethane scale, using glycine (shift of −346.4) as a secondary reference. All spectra were taken at room temperature.

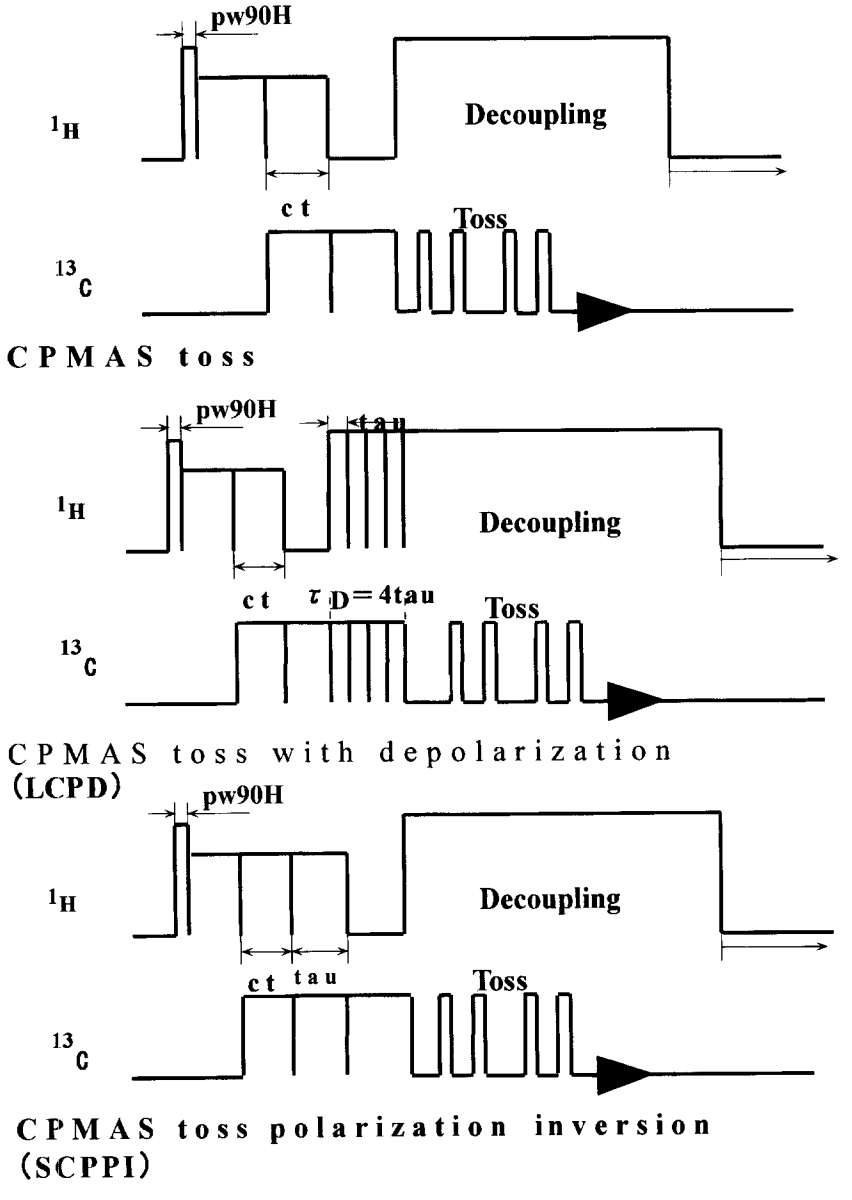

Fig. 5. Pulse sequences of Wu's method.

The ^{15}N NMR spectra of Witbank coals in Fig. 7 show only evidence of the presence of protonated nitrogens in five-membered rings. A diversity of these ring types is noted in the higher rank coal (Goonyella), and this observation is attributed to increasing ring size with rank. The six-membered ring nitrogen

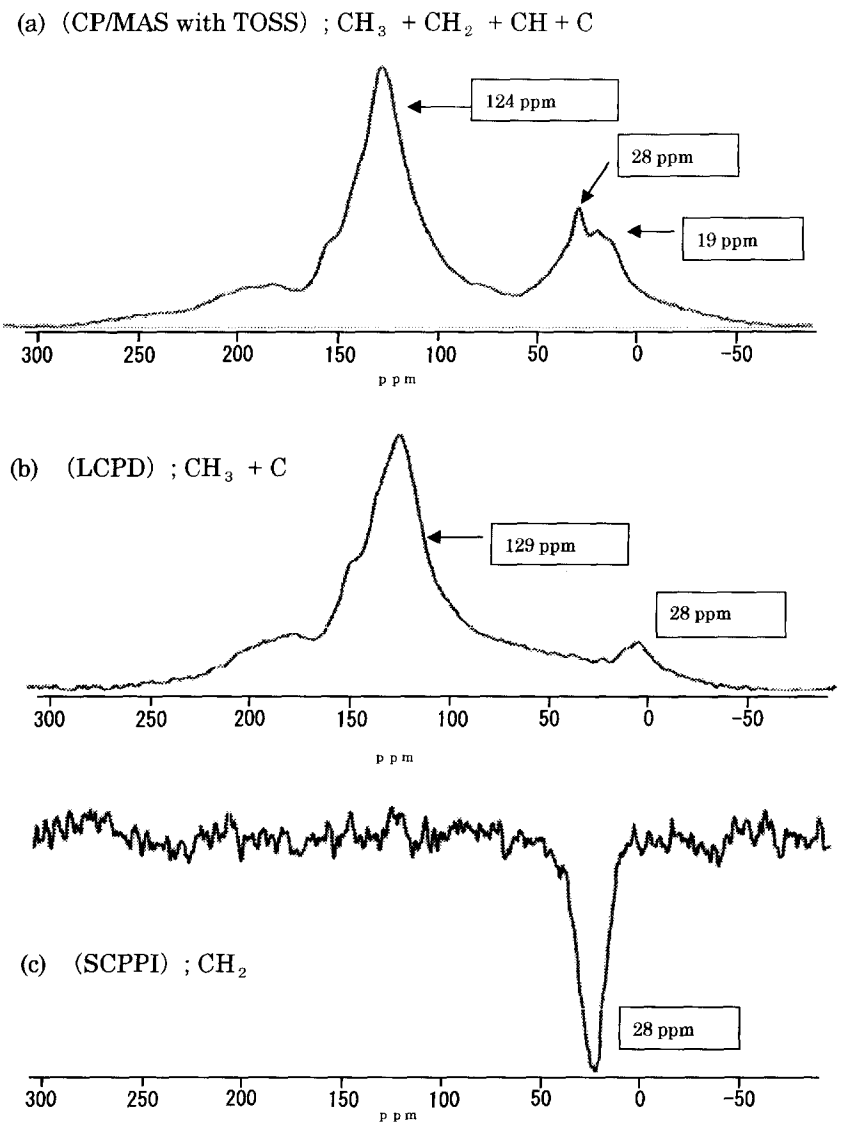

Fig. 6. ^{13}C CP/MAS spectra of Witbank coal with editing techniques: (a) CP/MAS with TOSS; (b) LCPD(CH_3 and C function group); (c) SCPPI(CH_2 function group only).

signals are not observed in the NMR spectra, which is not surprising considering the spinning speeds employed and the unfavourable cross-polarization dynamics for these types of nitrogen. These experimental results are in general agreement with the XPS data[36] which report that approximately

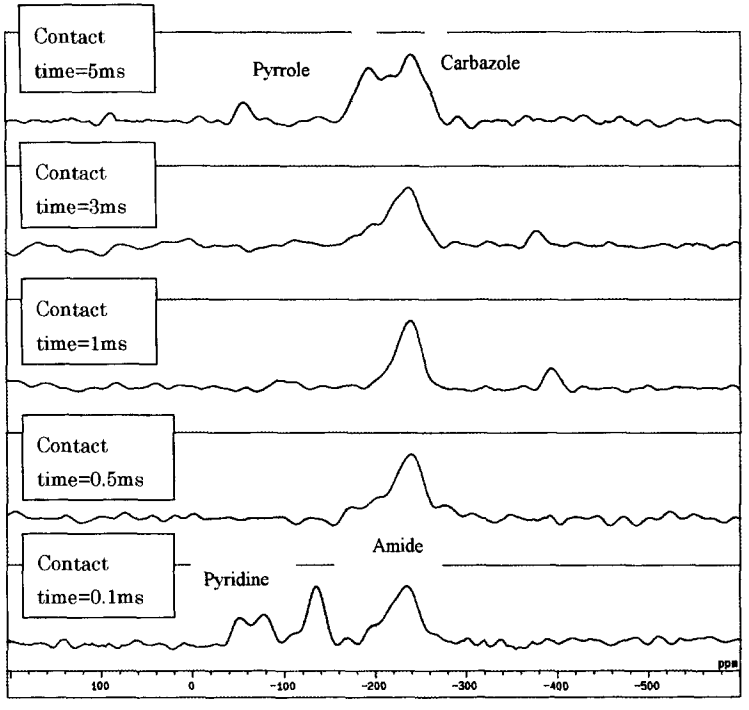

Fig. 7. ^{15}N CP/MAS spectra of Witbank using different contact time conditions.

25% of the nitrogens are present as six-membered ring types. In the case of other contact time conditions, we can observe different types of nitrogen structure from the same coal. Finally, it can be concluded from the data reported that the nitrogen signals are very small, resulting in spectra with poor S/N, even after the accumulation of 100 000 scans. This makes ^{15}N NMR studies on coal very time-consuming, prevents the detection of non-protonated nitrogens in pristine coals, and does not permit experiments such as those using variable contact times, by which the quantitative integrity of the results can be improved. This means that, for ^{15}N CP/MAS NMR to become a useful tool in coal research, it is imperative to develop methodologies to improve the sensitivity of experiments such as DNP-NMR.[37]

2.4. ^{37}Cl-MAS

Recent environmental problems of Cl-containing polymers give a spotlight on chlorine. Coal contains a small amount of chlorine (50–1500 ppm) but there is no information about chemical structure in raw coals. In the NMR field, although

^{35}Cl has a larger quadrupolar moment than ^{37}Cl, the sensitivity of ^{35}Cl is much larger than that of ^{37}Cl. Therefore, ^{35}Cl is selected as the observed nucleus in Cl-NMR measurements of coal. ^{35}Cl-MAS NMR spectra were referenced to the solid KCl, 0 ppm. First, analyses of several solid-state inorganic chlorides, KCl, NaCl and $CaCl_2$, were performed using ^{35}Cl-MAS NMR. KCl and NaCl show one sharp and one symmetric peak at 0 ppm and −49.6 ppm, respectively, which suggest that a small quadrupolar interaction occurs (Fig. 8). On the other hand, $CaCl_2$ shows a typical second-order quadrupolar pattern (Fig. 9). This difference is due to the crystal structures; the rock-salt structure in KCl and NaCl and the distorted rutile structure in $CaCl_2$. Since there is a possibility that coal contains some chemical sites of chlorine that have widely differing quadrupolar coupling constants such as KCl, NaCl and $CaCl_2$, a small flip angle of the pulse was applied in the ^{35}Cl-MAS NMR measurement on coal to provide an accurate quantitative spectrum. In coal A only one sharp peak was observed at −49.6 ppm, this is assigned to a NaCl type chloride (Fig. 10). Therefore, chloride in this coal is thought to originate in seawater, ground water, and so on. Thus, the investigation of coal using ^{35}Cl-MAS NMR is capable of the evaluation of the formative origin of chloride.[38]

2.5. ^{27}Al-MQMAS

The first application which focused on the use of ^{27}Al NMR to characterize mineral concentrates was obtained by a low-temperature ashing of coals in

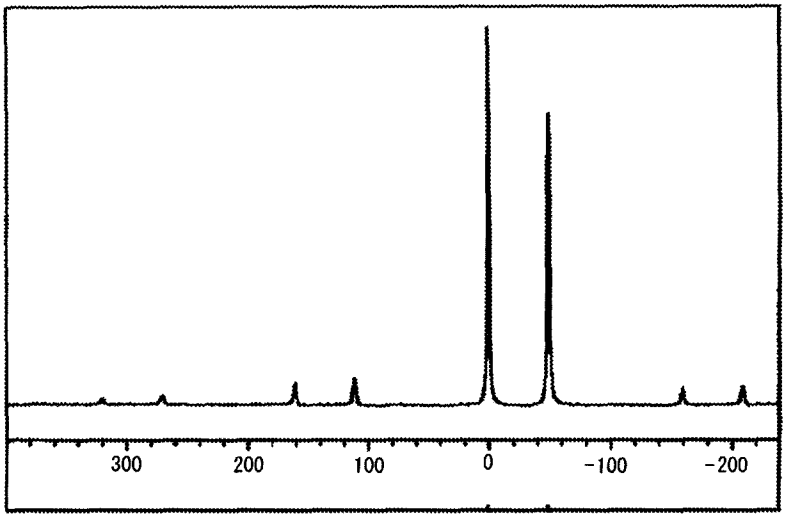

Fig. 8. ^{35}Cl-MAS spectrum of KCl : NaCl = 1 : 1 (mol ratio).

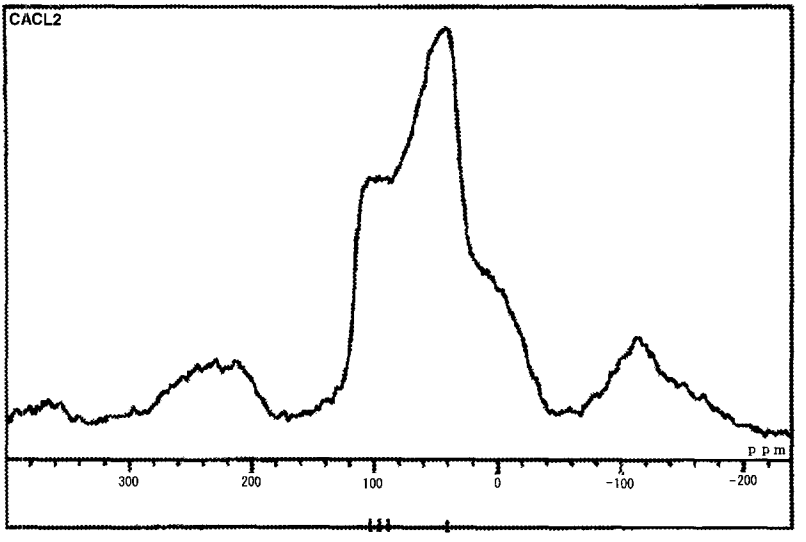

Fig. 9. ^{35}Cl-MAS spectrum of $CaCl_2$.

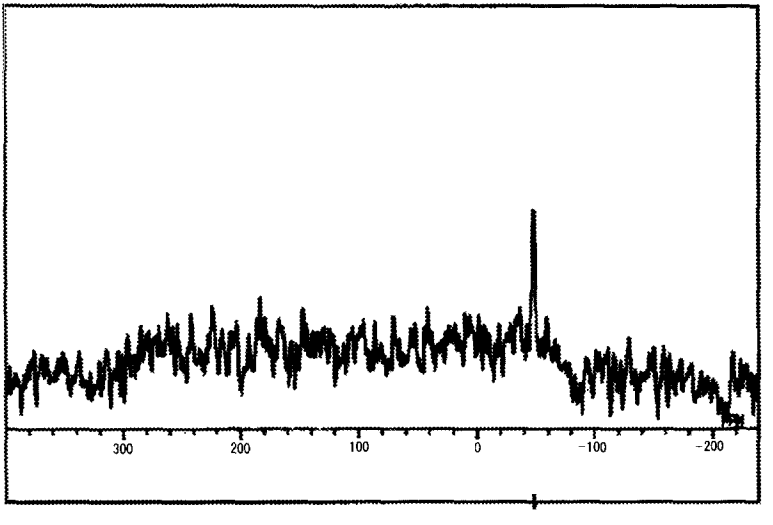

Fig. 10. ^{35}Cl-MAS spectrum of coal A.

order to obtain information on their mineralogy.[39] Silicon NMR spectra permit the identification of silicate resonances from quartz and clays, while aluminium spectra provided information on the tetrahedral and octahedral aluminium coordination sites which allow discrimination between kaolinite and mullite

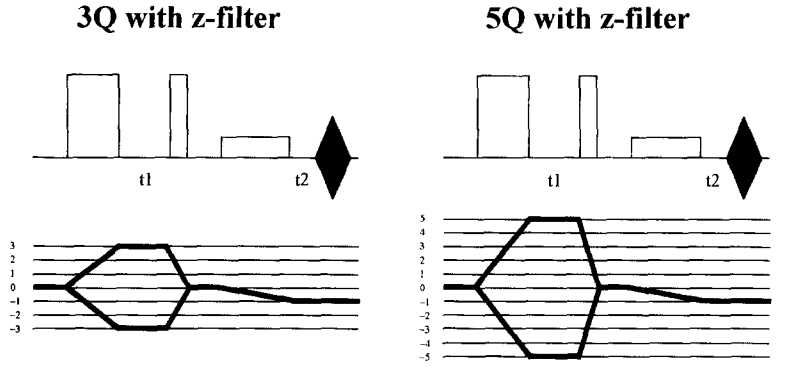

Fig. 11. Representative pulse sequences of MQ-MAS.

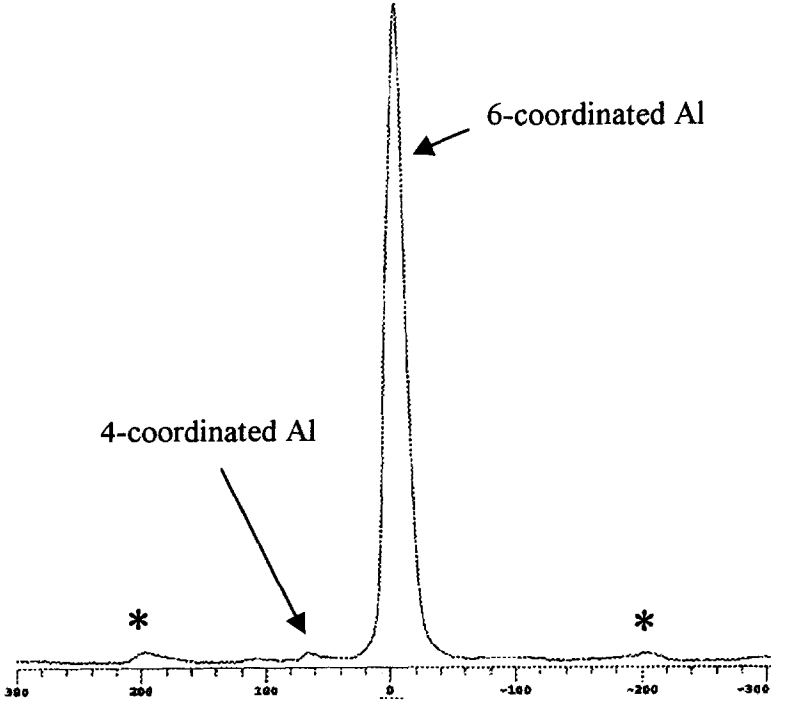

Fig. 12. ^{27}Al-MAS spectrum of kaolinite (* spinning sidebands).

clays that are present in the concentrates. A subsequent study[40] on mineral residues obtained from coal flash pyrolysis indicated that the ^{27}Al spectra were broad because of the presence of paramagnetic species and the effect of second-order quadrupolar interactions. However, the spectra were sufficiently resolved to detect the thermal transformation of kaolinite to quartz and mullite with increasing pyrolysis temperature. MAS techniques were employed to distinguish between the various clay minerals; quartz, kaolinite and smectite clays could readily be identified. Tetrahedral/octahedral aluminium ratios were determined for the coals, and the observation of an increasing tetrahedral aluminium content with coal rank indicated that there was a parallel between the diagenesis of the organic and inorganic matter in the coal.

Kaolinite ($Al_2Si_2O_5(OH)_4$) is a representative mineral component in coal. The structural analysis of aluminium in kaolinite was performed using the conventional MAS method and the MQMAS ($M = 3,5$ for a $I = 5/2$ nucleus such as Al) method. MQMAS is capable of averaging the second-order quadrupolar interaction under MAS by means of the use of the correlation of

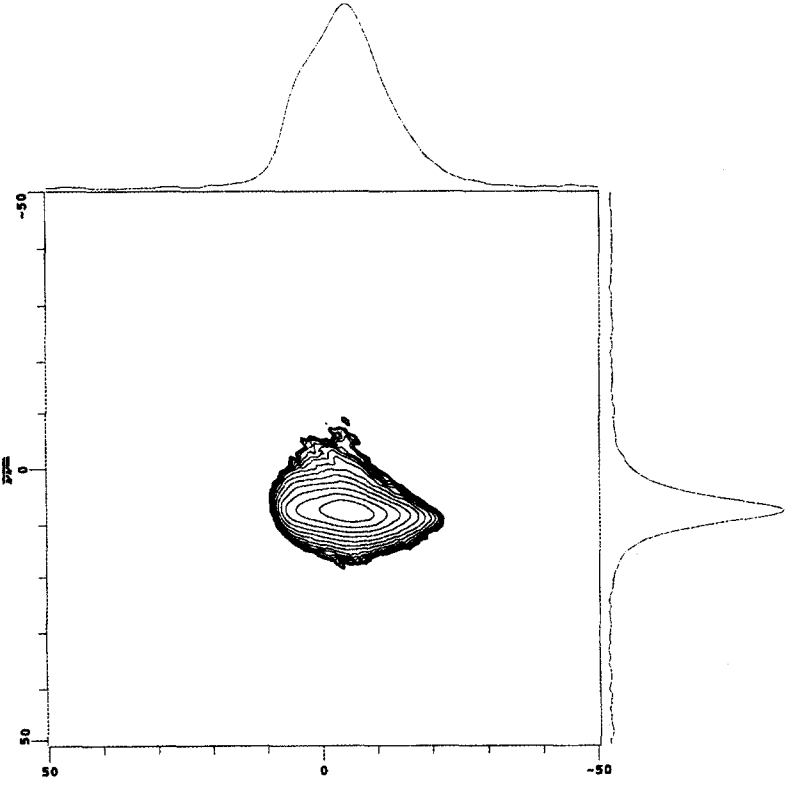

Fig. 13. ^{27}Al-3QMAS spectrum of kaolinite.

multiple-quantum and single-quantum coherences.[41] Pulse sequences including a z-filter pulse, which are selective at low rf-powers, were used in the MQMAS measurement.[42,43] In this section, the first MQ-MAS data are reported for kaolinite as a model of coal inorganic matter using two MQMAS pulse sequences.[44] Typical MQ-MAS pulse sequences used are shown in Fig. 11. The ^{27}Al-MAS spectrum in Fig. 12 shows a broadened and slightly asymmetric peak for 6-coordinated Al at -4.7 ppm and a very small peak assigned to 4-coordinated Al (referenced to 1.0 M $AlCl_3$ aqueous solution, -0.10 ppm). Figure 13 shows the ^{27}Al-3QMAS spectrum of kaolinite after shearing. A single slightly distributed cross-peak was observed, and the projection onto the isotropic dimension (F1) was narrower than that of the MAS dimension (F2) because of the elimination of the second-order quadrupolar interaction. The values of the isotropic chemical shift and the quadrupolar coupling constant extracted from the 3QMAS spectrum are 7.7 ppm (6-coordinated Al) and 3.2 MHz ($\eta = 0.8$), respectively. The ^{27}Al-5QMAS spectrum, after shearing, is shown in Fig. 14. The resonance is better resolved in the 5QMAS than in the

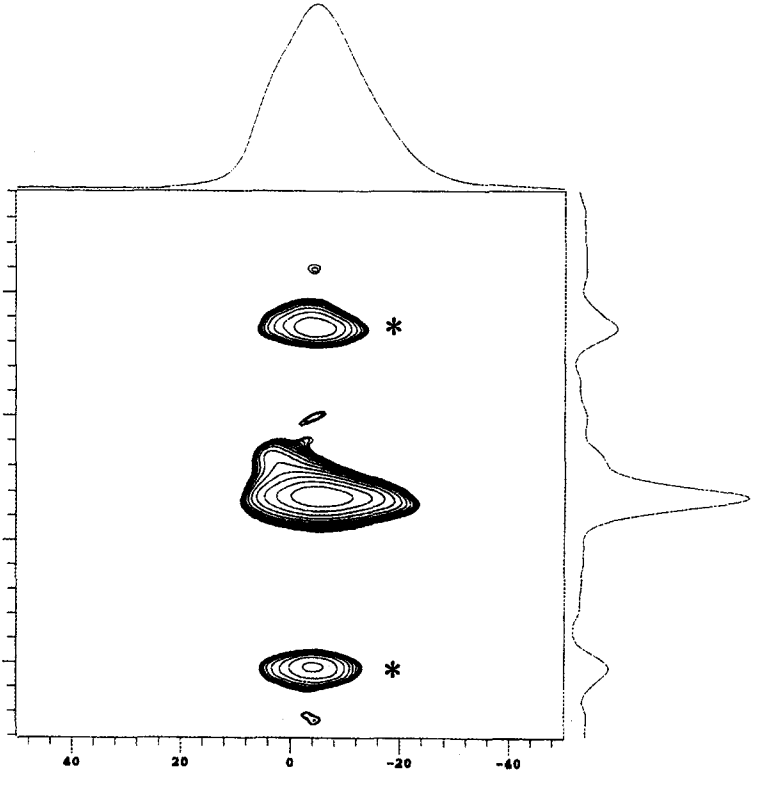

Fig. 14. ^{27}Al-5QMAS spectrum of kaolinite (* spinning sidebands).

3QMAS experiment. Thus it was suggested that there is another peak present besides the main cross-peak although the excitation of the 5Q coherence is less efficient than that of the 3Q coherence. This result of two chemical sites of 6-coordinated Al is consistent with earlier work,[45,46] and is the first direct observation of the existence of two distinct sites. The MQMAS technique has a high possibility of providing other chemical information on coals.

3. NMR IMAGING OF COALS

3.1. Single-point imaging and SPRITE imaging

A relatively new technique, which is demonstrating great potential in the area of coal research, is nuclear magnetic resonance imaging microscopy (NMR microimaging).[9–12] This method has its own special advantages; the sample is not destroyed because NMR microimaging is accomplished by placing the sample in a controlled magnetic field gradient. An image is obtained by measuring the spatial variation of the magnetic resonance frequency created by the magnetic field gradient. Contrast (spin density, spin-spin relaxation and spin-lattice relaxation time, etc.) and spatial resolution are selected by analysis conditions (number of voxels, strength of gradient and variable parameters, etc.).[47,48] Some excellent work at room temperature is reported by Botto *et al.*[9,10,12] However, a difficulty with the experimental setup needed in the case of coals occurs due to line broadening effects resulting from strong dipole–dipole interactions between protons arising from the rigid macromolecular network. In addition, the application of NMR microimaging to coal without using the solvent swelling method has so far been limited by the typical low resolution (more than 200 μm) which yields unclear images. This results from the influence of various magnetic susceptibilities (some due to mineral components and some due to paramagnetic components etc.) in coals. In addition, coals have various chemical structures; in particular, heterogeneous distributions of aromatic and aliphatic rich domains are expected as in macerals.

Single-point imaging (SPI) methods[49] have proven their worth for studies of short relaxation time systems, e.g. for rigid types of polymer and concrete.[50–52] The SPI pulse sequence does not employ band-selective pulses but relies on broadband RF pulses of limited duration. The pulse bandwidth (1/pulse length) must be greater than the maximum spectral width ($G_{max} \times$ sample length) to ensure uniform excitation. SPI is a pure phase encoding NMR microimaging technique. Therefore, position is encoded in reciprocal space, $S(k)$, where $k = 1/(2\pi)\gamma G_t$, by amplitude cycling of the applied phase gradients G. The signal is acquired at $t = t_p$ after a short excitation RF pulse in the presence of magnetic field gradients dB/dt with the quadrature method. Unlike frequency encoded images, SPI images are free from distortions due to B_0 inhomogeneity, susceptibility variations, and chemical shift variations.[53] The

resolution, even for short T_2^* species like coals, is limited only by the maximum gradient which can be applied to the sample. The signal intensity, S, from any point in the image is related to local proton density, ρ, by Eq. (1).

$$S = \rho \exp(-t_p/T_2^*) \times R(x) \tag{1}$$

where $R(x) = (1 - \exp(-T_R/T_1))/(1 - \cos\theta \exp(-T_R/T_1))$. The expression for $R(x)$ in Eq. (1) suggests that there will be a minimum acceptable repetition time T_R, for a given RF flip angle θ, in order to achieve an acceptable signal. This time restriction can be avoided in certain instances by reducing the pulse flip angle at the expense of the observable signal.

A modified SPI, single-point ramped imaging with T_1 enhancement (SPRITE),[51] consists of a ramped phase encoded gradient in the primary phase encoded direction and conventional phase encoded gradients in the other directions. The use of a ramped phase gradient permits imaging with greater speed and with lower values of dB/dt, which minimizes the gradient vibrations compared with SPI. However, a great time improvement is achieved with samples where T_1 relaxation times are of the order of the gradient rise time. Magnetization preparation is easily incorporated into the SPRITE sequence by sampling a single k-space point after each magnetization filter application. Balcom *et al.*[54] have demonstrated that magnetization preparation permits accurate T_2 and T_1 mapping of samples with short relaxation times.

This section discusses 3D-SPRITE which has been shown to be successful for studying short relaxation time systems and which is free from distortions due to susceptibility variations for coals with high resolution at a frequency of 400 MHz.[55] The results obtained are discussed in relation to the three-dimensional distribution of the mobile component for two kinds of coal, Witbank and Goonyella. At the same time, inversion recovery preparation experiments (T_1 mapping), T_2 mapping and T_2^* mapping based on SPRITE methods are presented in order to clarify the chemical heterogeneity of coals.

We will consider several basic features of SPRITE methods (Fig. 15). In the SPRITE sequence, unlike the basic SPI sequences, we don't switch the gradient on and off for each acquisition. Instead we ramp this gradient in discrete steps and apply an RF pulse, collecting a single datum point, at each gradient step as shown in Fig. 15(a). The step length is less than 5 ms so that the overall gradient duration is brief and the mechanical force on the gradients is minimal (because of low overall dB/dt values). An extremely loud SPI sequence becomes nearly inaudible when reconfigured as an equivalent SPRITE experiment. The phase-encode gradients in the SPRITE sequence inherently spoil transverse magnetization. When identical measurement conditions are used, typically SPRITE methods are quite time-saving, at the same time possibility of damage to the probe, which is accepted using the SPI sequence, is much less.

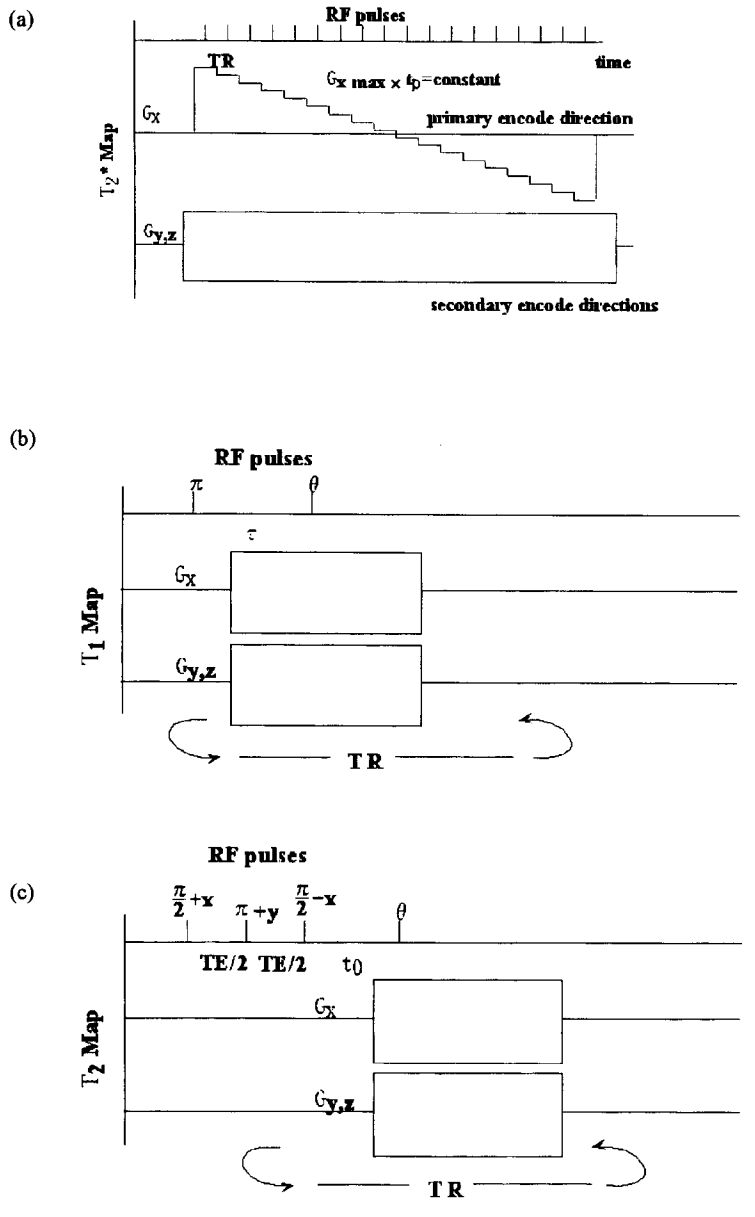

Fig. 15. Pulse sequence of T_1 and T_2^*-SPRITE imaging.

By examining Eq. (1) it can be seen that by using a long T_R, and/or a small RF flip angle, α, an image is obtained of the spin density, ρ, weighted purely by the local T_2^*,

$$S \propto \rho \exp(-t_p/T_2^*) \tag{2}$$

When using T_2^* mapping with a variable value of t_p, the magnitude of the gradient step size must be adjusted in order to maintain a constant k-space step,

$$\Delta k = (2\pi)\Delta G^* t_p (FOV = 1/\Delta k)$$

The proposed T_1 and T_2 mapping methods employ SPRITE to obtain the image, with some form of spin preparation imposed before acquiring the SPRITE k-space point. From Eq. (1) it is seen that for a large flip angle, α, and a T_R of the order of T_1, T_1 contrast can be introduced into a SPRITE image. The measurement is, however, more sensitive if a longitudinal recovery is introduced, following magnetization inversion, before sampling the SPRITE point, as shown in Fig. 15(b). By varying the delay time between the 180 degree inversion pulse and sampling pulse, α, images are obtained with local intensities weighted by T_1, as shown in Eq. (3):

$$S \propto \rho \exp(-t_p/T_2^*)(1 - 2\exp(-\tau/T_1)) \tag{3}$$

assuming that T_R is long enough to allow complete T_1 recovery between sequential RF pulses. Since t_p is a constant, the T_2^* decay is simply a constant weighting term, and the only variation between images is due to T_1 recovery.

The method proposed for spatially mapping T_2 requires spin preparation with a CPMG echo train with subsequent acquisition of the SPRITE point as shown in Fig. 15(c). The echo train is interrupted after n echoes, the transverse magnetization is z-stored, then the field gradient is switched on and the T_2-weighted longitudinal magnetization sampled with a low flip angle pulse. The z-storage is necessary to avoid spin dephasing of the magnetization during the gradient switch. This has the added advantage that it places the prepared magnetization along the axis with the longest relaxation time. A spoiling gradient is employed to prevent the formation of echoes at low-amplitude phase-encode steps. Repeating this experiment with a variable number of CPMG echoes produces images whose signal amplitudes decay as a function of T_2. The z-storage will, however, introduce T_1 relaxations into experiments, and these lead to images that are functions of both T_2 decay and T_1 recovery. Performing the experiment with z-storage on the positive z-axis, then repeating the experiment with z-storage on the negative z-axis and subtracting the k-space data, a k-space representation of the object is obtained, weighted by a pure T_2 decay term,

$$S \propto \rho' \exp(-t_p/T_2^*)(\exp(-2n\tau/T_2)) \tag{4}$$

where ρ' is directly proportional to M_0 (the initial longitudinal magnetization). The Fourier-transformed 'real' profiles could, equivalently, be subtracted; however, by subtracting the k-space data the necessity of phasing the results is avoided. This method gives accurate T_2 maps; however, the value of M_0, incorporated into $A_0(=2M_0 \exp(-t_g/T_1))$, where t_g is a finite period of time, cannot be obtained from the experiment. The true M_0 is most reliably obtained in the samples with a T_2^* mapping experiment. Alternatively, the data obtained has been fitted using similar methods with one z-storage pulse to an offset, to take into account the T_1 recovery term.

The size of the bulk samples was about 2.5 mm × 2.5 mm × 2.5 mm for the 3D-SPRITE experiment. The specimen was placed into a 5 mm diameter standard NMR tube. The 3D-SPRITE sequence was applied to observe the distribution of mobile components in the coals using an encoding time of 80 μs (T_2^* is about 100 μs for coal mobile components). On the other hand, as T_2^* is about 30 μs for coal samples with immobile components, the contributions of the immobile components to the signal intensity is negligible. The recycle delay time used is 10 ms and a gradient of about 1.08 $T\,m^{-1}$ for the three axes. The experimental sample scheme is shown in Fig. 16.

Figure 17 presents a 3D-SPRITE image of Goonyella (a) and Witbank (b) coal. The lighter areas in this sample correspond to higher concentrations of mobile component, as the conditions of this SPI experiment were set to the T_2^* value of the mobile component. The distribution of protons in the mobile component was mapped exclusively in this way. A user-adjusted threshold was applied to define the minimum intensity used to calculate the contiguous surface in 3D rendering.[56] This threshold was chosen to afford the most accurate representation of the sample topology while suppressing low S/N features near the sample surface. The lighter regions correlate with increased nuclear spin density; the lighter the region the greater the density. It is clearly evident that the three-dimensional distributions of the mobile components are very heterogeneous and their components have some three-dimensional connections to each other.

A distinct advantage of NMR microimaging over other imaging techniques is that one can display any plane required without sample reorientation, since the entire sample is digitized in a three-dimensional array. The thickness of one plane is about 50 μm because of the setup measurement conditions. It is obvious that SPI gives significantly clearer images of coal than those (Fig. 17(c)) obtained by the standard spin-echo imaging sequence with swelling caused by pyridine-d_5.[57] The amount of mobile component, which was calculated from all of the images using a program supplied by JEOL, is 22% in the case of Goonyella. This result is almost consistent with that of the ^1H wide-line method calculated from the sub-spectra line simulation data. On the other hand, the result of the SPI method (22%) may be compared with that of the spin-echo method (36%). As the estimated contribution to the total proton signals from residual protons in pyridine-d_5 is less than 0.1%, this is a

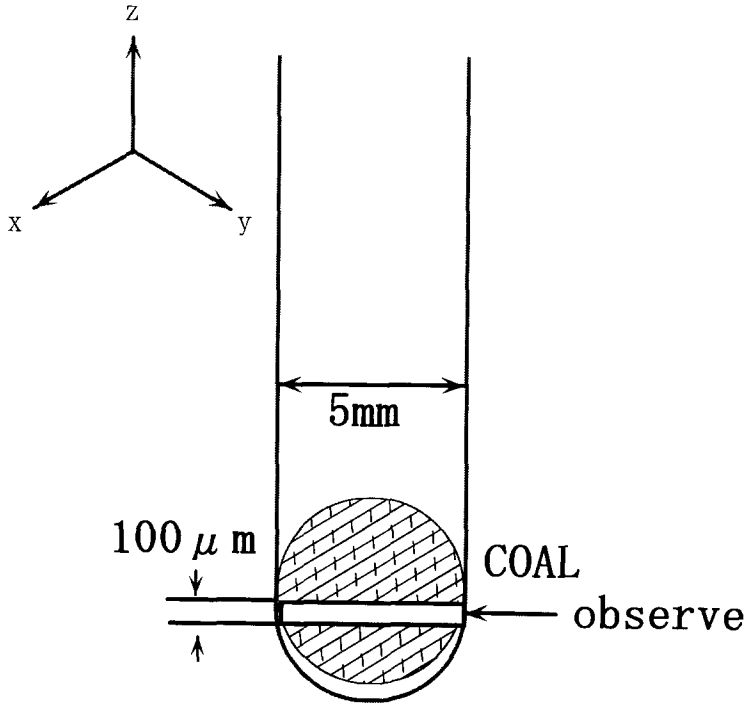

Fig. 16. Experimental sample scheme.

substantial enhancement in the amount of mobile component due to swelling. The results from SPI are definitely correct concerning the fractional intensity for the mobile component. In addition, the region of the mobile component is basically independent in a plane and heterogeneous on a scale of 100 μm, the distribution of maceral. These results are very interesting, since the dominant heterogeneity of coals, maceral, are on a scale of tens to hundreds of micrometres.[58] The amount of mobile components in Witbank (17%) is less than in Goonyella. According to the properties of both coals, it is reasonable to say that the data for Goonyella coal obtained using the Gieselar–Plastmeter[59] and *Ro* (vitrinite percentage refraction rate), are better than those of Witbank coal for coking purposes.

It is well known that coals have two ^{1}H structure domains (aliphatic and aromatic) and the T_1 values of the aliphatic domain are longer than those of the aromatic domains.[60] Therefore, T_1 mapping SPRITE was applied because there are differences in the T_1 values between the aliphatic and aromatic domains. Figure 18 shows T_2^* mapping SPRITE and T_1 mapping SPRITE images of Goonyella coal with various T_1 values. It is clear that these images are similar to each other. It is likely that the distribution of the aliphatic domain is not only almost the same as that of the aromatic domain but also the same as that

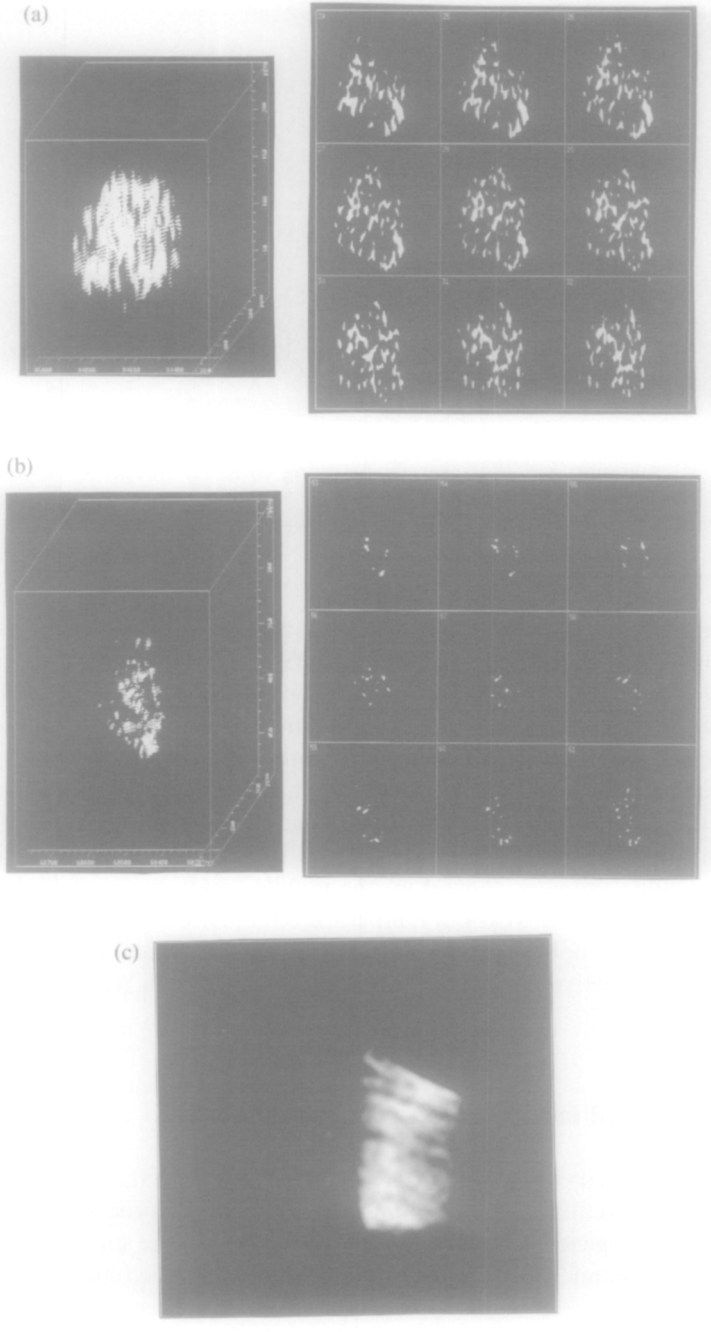

Fig. 17. NMR 3D and 2D images of (a) Goonyella coal; (b) Witbank coal obtained by SPRITE method; and (c) Goonyella coal obtained by spin echo method.

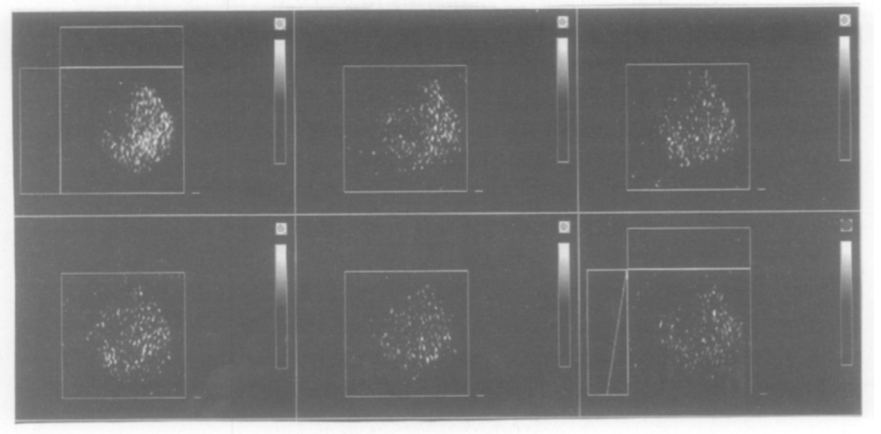

Fig. 18. T_2^* mapping SPRITE and T_1 mapping SPRITE images of Goonyella with various T_1 values (from top left, T_2^* mapping SPRITE image, T_1 mapping SPRITE images $\tau = 20$ ms, 40 ms, 60 ms, 80 ms, 100 ms).

of the mobile component as far as the resolution of the image is concerned. Other evidence is derived from CRAMPS-based T_1 measurements[61] which show that the difference of T_1 values between the aliphatic domain and the aromatic domain is small because of spin diffusion effects in the case of Goonyella as shown in Table 1. Therefore, the mobile component is in a homogeneous distribution between the aliphatic and aromatic domains. On the other hand, T_2^* mapping SPRITE and T_1 mapping SPRITE images of Witbank with various T_1 values as shown in Fig. 19 reveal that the distribution of images is quite different. Therefore the mobile component is mainly provided by aliphatic domains. At room temperature there are significant differences in the origin of the mobile component among the two typical coals and SPRITE methods are effective for clarifying the properties of coals which have very high inhomogeneities.

3.2. *In situ* NMR imaging of coals at high temperatures

Thermally induced changes in coals are interesting from the standpoint of both fundamental and applied research into the steel-making process.[62] Furthermore, for very inhomogeneous coals, there is a fascination in the study of the influence of thermal dynamic changes. To monitor the dynamic changes in coals with temperature, an *in situ* method must be used, because it is well known that the properties of coals change dramatically in the high temperature range (from 350 to 550 °C).[63–73] However, the main problem with standard empirical tests, such as the Gieseler plastometer and Audibert Arnudilatometer, to study changes in

Table 1. T_1 proton of relaxation parameters derived for two typical coals

Goonyella	Percentage (%)	T_1 (s)
Slow component		
aliphatic	12	1.02
aromatic	11	0.92
Rapid component		
aliphatic	88	0.032
aromatic	89	0.047

Witbank	Percentage (%)	T_1 (s)
Slow component		
aliphatic	39	0.71
aromatic	14	0.97
Rapid component		
aliphatic	61	0.031
aromatic	86	0.054

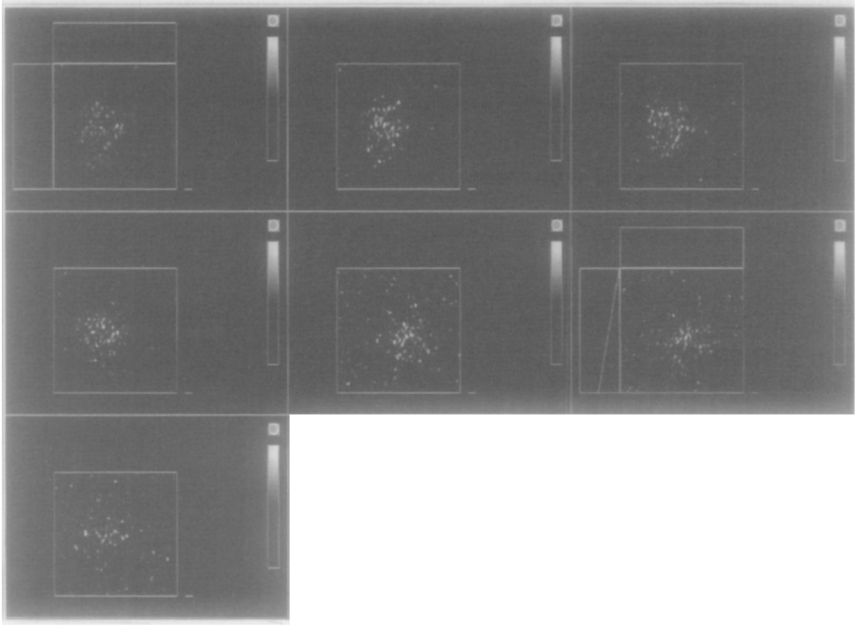

Fig. 19. T_2^* mapping SPRITE and T_1 mapping SPRITE images of Witbank with various T_1 values (from top left, T_2^* mapping SPRITE image, T_1 mapping SPRITE images $\tau = 10$ ms, 30 ms, 50 ms, 70 ms, 90 ms, 110 ms).

the properties of coals is that they have no relationship with the actual structural changes. High-temperature ^{1}H-NMR is a powerful technique for the *in situ* investigation of molecular motions in coals during carbonization. The ^{1}H-NMR spectra obtained for coals basically comprise contributions from a mobile and an immobile (rigid) component.[74–76] The technique was shown by Sanada *et al.*[75] to clarify the nature of fluid materials from coal during early carbonization stages. In the early 1980s, Lynch *et al.* detected both mobile and immobile components using a simple spectrometer (PMRTA; proton magnetic resonance thermal analysis).[77–84] They used mainly the empirical parameter M2 T16, corresponding to the second moment integration, limited to a width of 16 kHz, for monitoring changes in fluidity. PMRTA techniques have been used in many studies[78, 80, 81] dealing with the quantification of interactive effects between different components in coal blends.

In most studies with PMRTA, the overall concentrations of fluid and inert material over the thermoplastic range have not often been reported,[79] because of a combination of the convenience of handling large data sets and the likelihood of truncating broad Gaussian signals at high temperatures where sensitivity is much lower. Recently, Snape *et al.*[85, 86] have achieved this goal using a Doty probe operating at a frequency of 100 MHz for ^{1}H. The effects of particle size, mild oxidation, and different heating regimes on plasticity development are reported. Furthermore, these *in situ* measurements have confirmed that plasticity development is a reversible phenomenon provided that relatively fast quenching rates (ca. 75 °C min^{-1}) are used. However, from the NMR sensitivity point of view, a frequency of 100 MHz is not enough to monitor the dynamic change, because NMR sensitivity depends on the magnitude of B_0 used. In addition, NMR relaxation times as useful parameters for studying coal properties are changeable with the magnitude of B_0. Recent representative works[61, 87] were performed at a frequency of 300 or 400 MHz, therefore *in situ* measurements should be performed at a frequency of 400 MHz in order to provide a comparable discussion.

The results obtained from PMRTA and standard *in situ* ^{1}H-NMR investigations is limited to the average data for heterogeneous coals which thus lacks information about the distribution of the mobile component and its variations in the specimen due to chemical changes caused by the heating process.

It has long been established that the response of coal to process conditions during coking and combustion is strongly related to the heterogeneous nature of coal.[59, 88] Traditional means of characterizing coal at the microscopic level by direct observation are optical and electron microscopic techniques. Both methods have some disadvantages. Reflected light optical microscopic analysis (ROM) of coal is typically performed using oil immersion techniques.[89] Additionally, a given coal sample is suitably prepared for analysis and this process irreversibly alters the sample. Scanning electron microscopy (SEM) can surpass ROM in image quality, but at the same time,

is limited by the need for sample coating with conductive materials and the high vacuum conditions which are generally required during analysis, necessitating desiccation of the coal sample prior to imaging. Neither method can be performed in an *in situ* investigation during heating without destroying the sample.

In this section, we have described the first systematic *in situ* variable-temperature NMR microimaging study of coals between 25 and 600 °C in order to clarify the behaviour of the mobile component at high temperatures in heterogeneous coal specimens.[90,91] The main specifications of the probe are maximum sample temperature 600 °C; maximum field gradient strength 250 gauss cm^{-1}; maximum current 50 A; sample size 5 mm. These specifications can be achieved by use of a rectangular enamelled wire for the coil producing the gradient field (Fig. 20), cooling by water and an alcohol mixture, using the coil moulding technique (Fig. 21), and a very efficient heating system in the probe (Fig. 22). The rectangular wire, has an extremely high space factor (over 95%), so it is possible to get a high total current density, and it also has good heat dissipation. A Fourier–Bessel expansion method[92] was used for optimal coil design. Following this design, the coil was wound as a stand-alone type, cooled by a closed circulation cooling system. Coils and cooling pipes are moulded in resin for heat dissipation and to prevent coil vibration.

Figure 23 shows the variable temperature probe: it has a very long spiral heating wire, and the path of the heated N_2 gas is very close to this heating

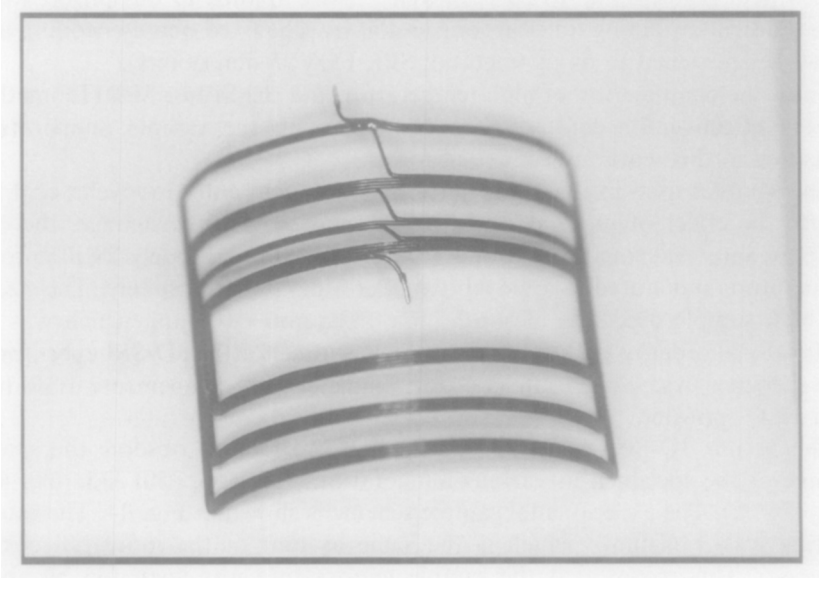

Fig. 20. Coil piece using rectangular enamelled wire.

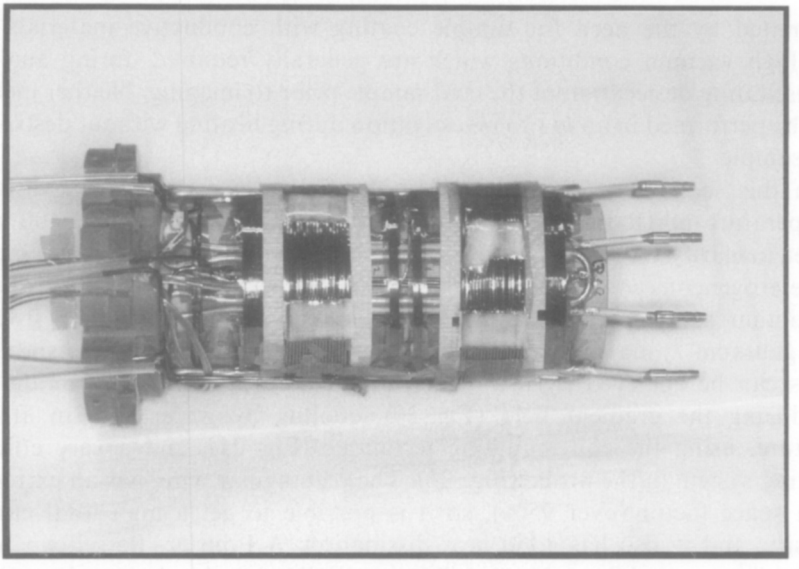

Fig. 21. Cooling pipe and gradient coil.

wire, so that a high efficiency of heat exchange is achieved. The SPI and SPRITE methods have been tried at 500 °C using this probe. Both of these methods are very tolerant of gradient-switching times. For example, large pulsed field gradients up to 250 gauss cm^{-1} were applied to this probe, which gave gradient-switching times as long as 150 μs. The fixed phase-encoding time t_p can be shortened to 64 μs (method: SPI, FOV: 5 mm points).

Thus, the combination of high temperature and the SPI or SPRITE method is very effective for coal science. The errors in the sample temperatures measured in this work are estimated to be ±2 °C.

The samples used in this study were Witbank coal and Goonyella coal. To reduce the effect of residual water in the coal on the microimage, the coal samples were evacuated at about 10^{-2} Torr for approximately 24 h at room temperature and stored in a glovebox under a dry N_2 atmosphere. The size of the bulk sample used was about 2.5 mm × 2.5 mm × 100 μm, which was cut artificially in order to reduce the measurement time for the 3D-SPI experiment. The specimen was placed into a 5 mm diameter high-temperature ESR tube with Al_2O_3 powder.

The *in situ* 3D-SPI sequence was applied in order to observe the spatial change of the specimen at various temperatures (25, 300, 350, 375, 400, 425, 450, 475 °C). The experimental sample scheme is shown in Fig. 24. The rate of heating was 3 °C min^{-1} which is the same as that of the industrial coking process.[93] This means that the sample temperature was increased by about 24 °C (8 min × 3 °C min^{-1}) during the NMR microimaging measurements.

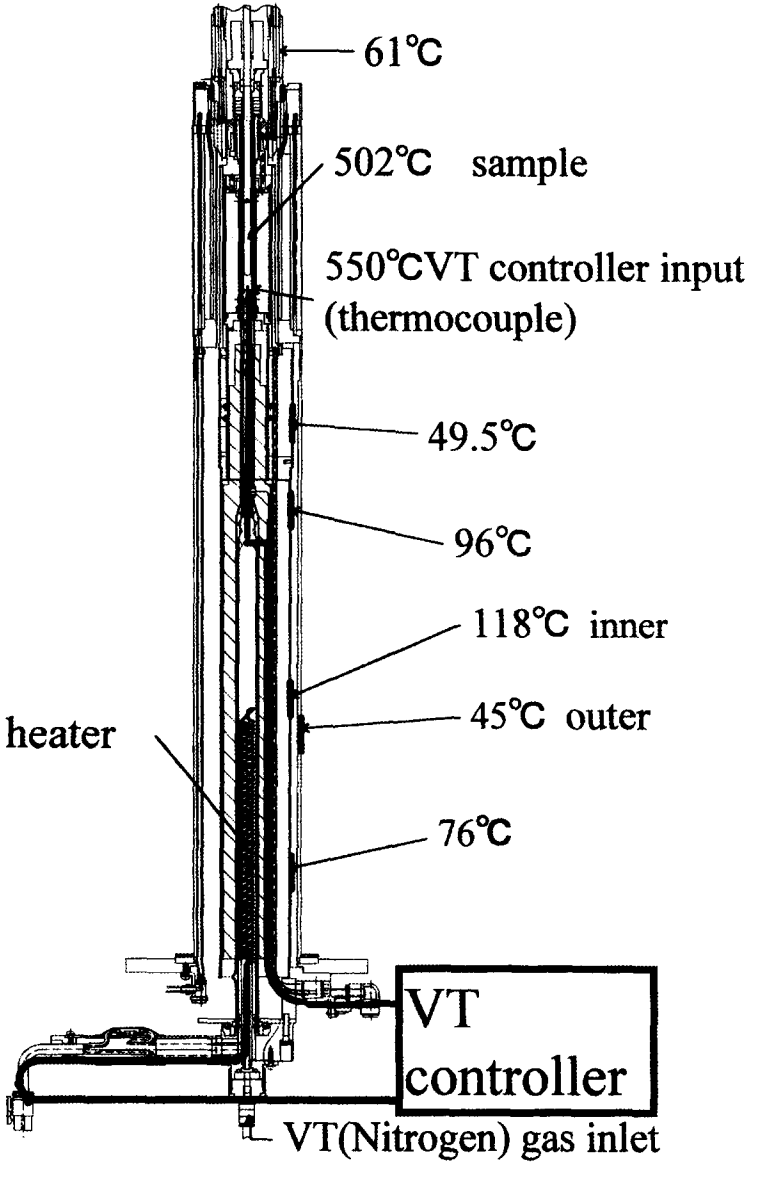

Fig. 22. Heating system in the probe and the temperature at specific points during the heating test when sample temperature was 502 °C.

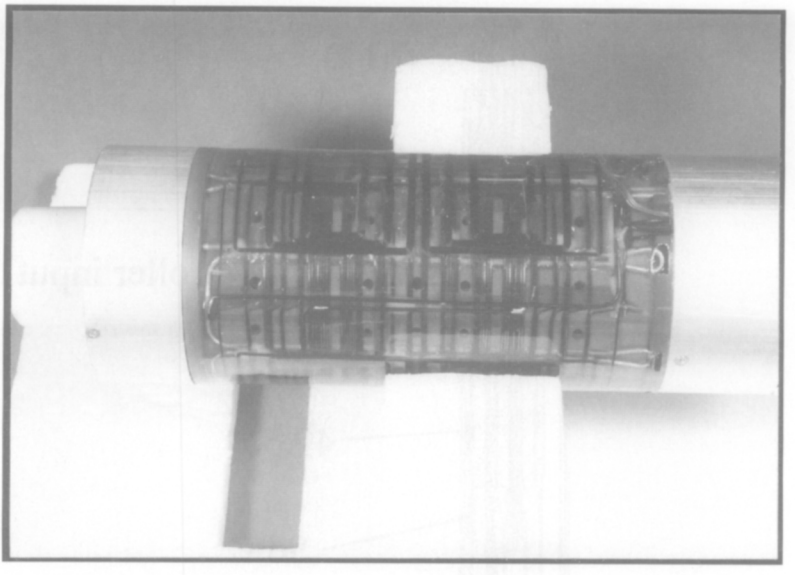

Fig. 23. High-temperature imaging probe.

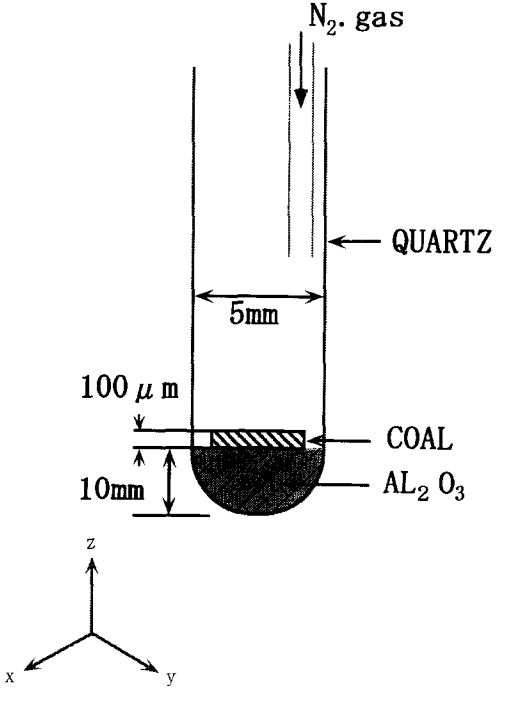

Fig. 24. Experimental sample scheme for *in situ* imaging.

It is well known that coals start to soften and melt at about 400 °C, and then to cake and carbonize at more than 450 °C. A solid echo pulse sequence with a refocusing time of 4 μs was used to minimize the loss of signal due to the dead time of the NMR coil. Figure 25 shows the ^{1}H-NMR spectra for Witbank coal obtained at various temperatures (e.g. at maximum fluidity of 400 °C, and after resolidification at 525 °C). The sensitivity is much better than that reported elsewhere,[85,86] where resolidification occurs because of a high B_0 (400 MHz) value. The spectra are deconvoluted into components for the mobile and immobile phases observed. Figure 26 shows the variations in the existence rate and the half-width of the signals at half-height for the mobile component between 25 °C and 550 °C in both coals. As the temperature increases, the existence rate of the mobile component increases gradually and shows maximum mobility at about 450 °C for the Goonyella sample, corresponding to a minimum in the half-width values. The existence rate of the mobile component increases less rapidly at temperatures over 475 °C. Good agreement has been obtained for the temperature of maximum mobility between Gieseler plastometry and rheology experiments[94] and comparable behaviour has been reported using the PMRTA method[77–84] and Snape's method.[85,86] Further, Fig. 26 indicates that maximum mobility is attained at a lower temperature for the Witbank coal than for the Goonyella sample, consistent with the Gieselar plastometer data. However, the advantage of the results performed at 400 MHz is that the dynamic thermal behaviour of the immobile component shows the same tendency as the mobile component found in Snape's work which was performed at 100 MHz. Since in general T_2 changes with temperature, the change of T_2 for the immobile component is reasonable at a higher value of B_0. In addition, the increase of the T_2 value, corresponds to a decrease of the signal half-width for the mobile component. This means that the increase of molecular mobility, which is subject to the rules of physical relaxation, and the increase of the mobile component rate is caused by the chemical and physical changes of the three-dimensional structure due to heating. Therefore, it is an acceptable conjecture that the increase in the T_2 value of the immobile component is caused by the chemical and physical changes occurring with heating.

Figure 27(a) shows the NMR image of Goonyella coal at 25 °C; it is found that the distribution of the mobile component is very heterogeneous, like the distribution of macerals in coal samples cut with a thickness of 100 μm. As the temperature increases, the mobile component increases but remains heterogeneous (Fig. 27(b),(c)). The images of Fig. 27(d),(e) and (f) show that the distribution of the mobile component becomes more homogeneous. This means that coal starts to soften and melt, and the mobility of the mobile component increases dramatically. It is likely that these areas which are easy to soften and melt are fixed initially, because there are rich areas of mobile component on the right-hand side of Fig. 27(a) at 25 °C. It is very interesting that the softening and melting areas move from the right side to the left side in these images,

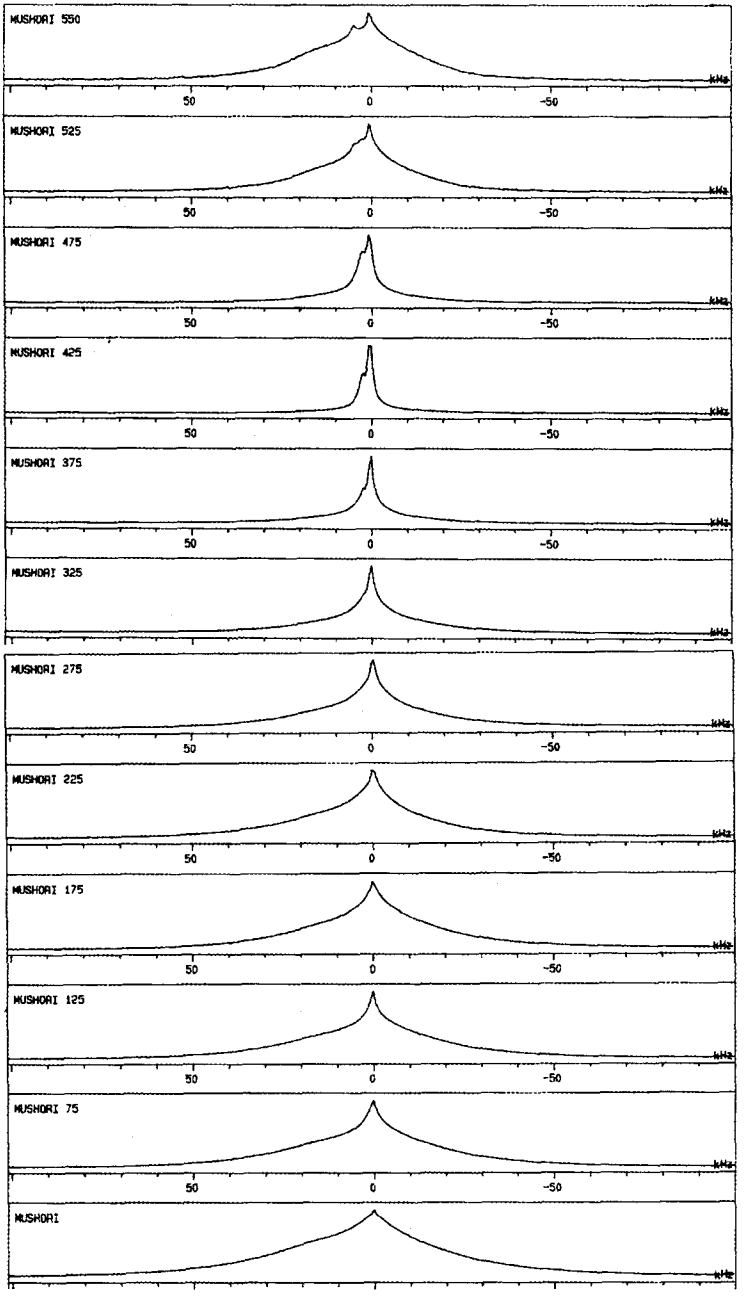

Fig. 25. ^{1}H-NMR spectra for Witbank coal obtained at various temperatures.

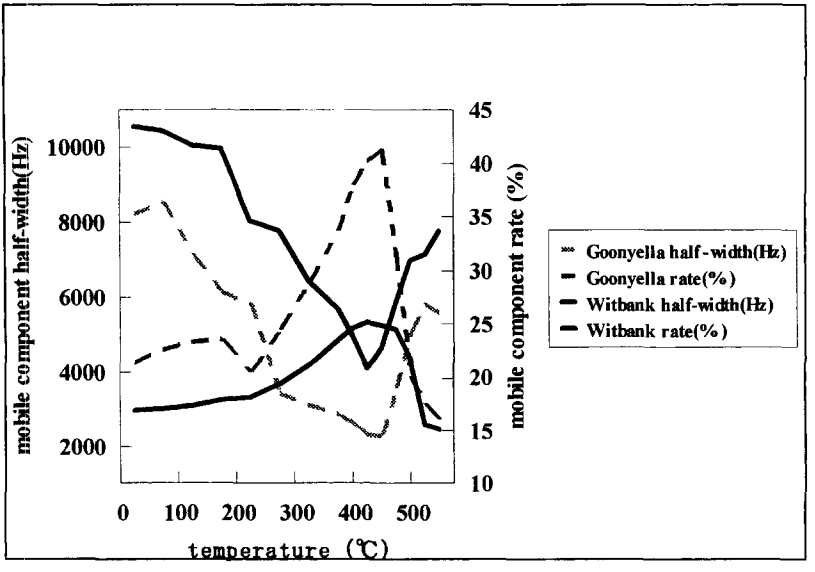

Fig. 26. Variations in the rates and their half-widths at half-height for the mobile component between 25 °C and 550 °C for Witbank and Goonyella coals.

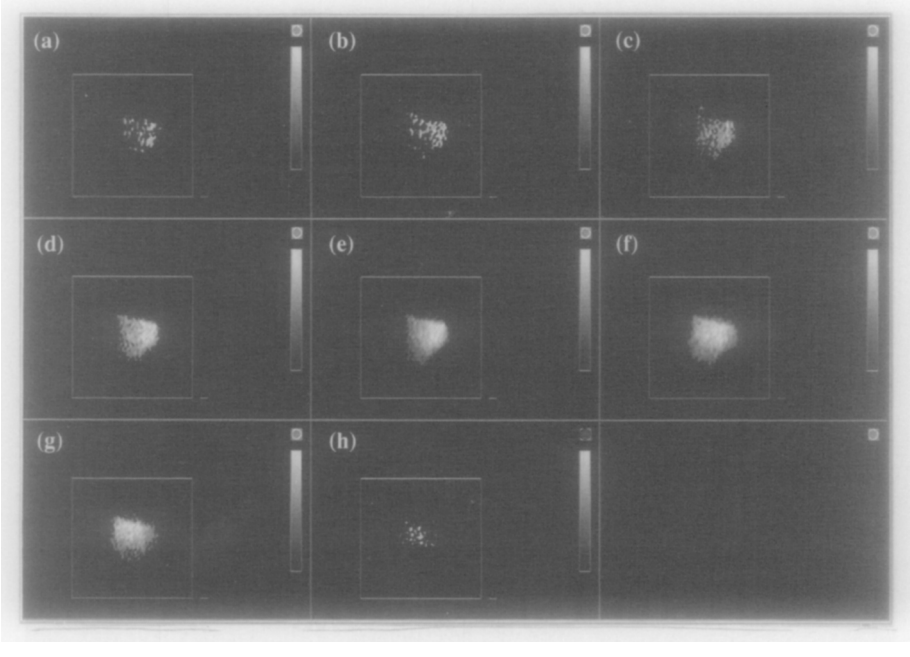

Fig. 27. NMR image of Goonyella coal at (a) 25 °C; (b) 350 °C; (c) 375 °C; (d) 400 °C; (e) 425 °C; (f) 450 °C; (g) 475 °C; (h) 500 °C.

similar to a diffusion phenomenon. According to the signal half-width of the mobile component at 400 °C (where 400 °C is the average data from 400 to 425 °C during the measurement, as the temperature was increasing at the rate of 3 °C min^{-1}), in comparison to other materials measured at the same frequency, the mobility of the mobile component is comparable to that of gels, not liquids.[95] Therefore, it is likely that stretching of the mobile component occurs since some immobile components are changed to mobile components by the heating process. At the same time some mobile components which have good fluidity initially, melt first and move by slow diffusion to other areas. As the optimized variable encoding time at each temperature was used in order to avoid contributions from immobile components in these experiments, the results show the behaviour of the mobile component only. When the temperature is over 450 °C, resolidification starts and the extent of the mobile component decreases (Fig. 27(g)). At 500 °C (Fig. 27(h)) there are few mobile components because of resolidification. Some mobile components become immobile and carbonization means that the number of protons in coal decrease rapidly. Figure 28 shows an image of Witbank coal at 425 °C, which indicates maximum mobility. It is surprising that it shows some low mobility areas and some unsoftened areas, in spite of being the maximum mobility for the Witbank sample. It is likely that low rank coals for coking, like Witbank, have some inert areas which are difficult to soften and melt at its maximum mobility temperature and to move to other areas by diffusion.

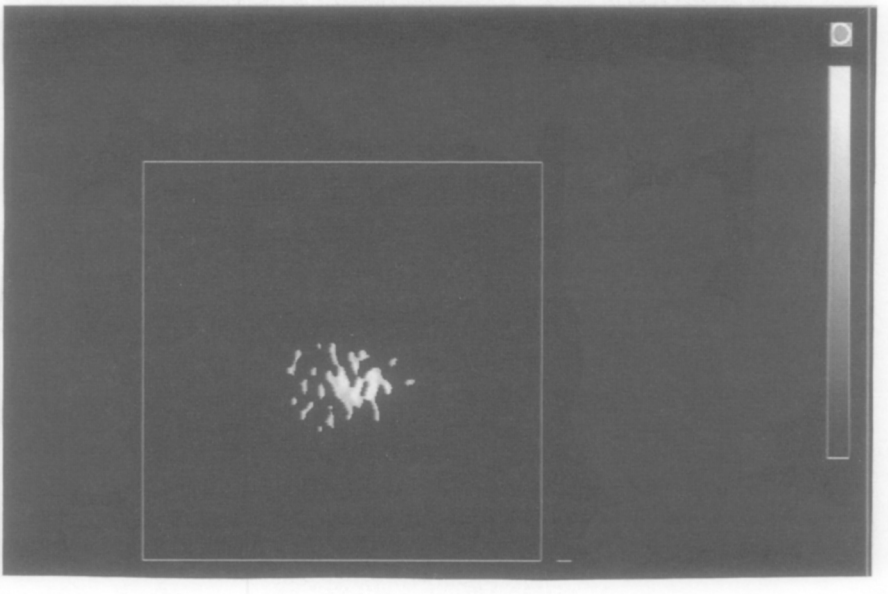

Fig. 28. Image of Witbank coal at 425 °C.

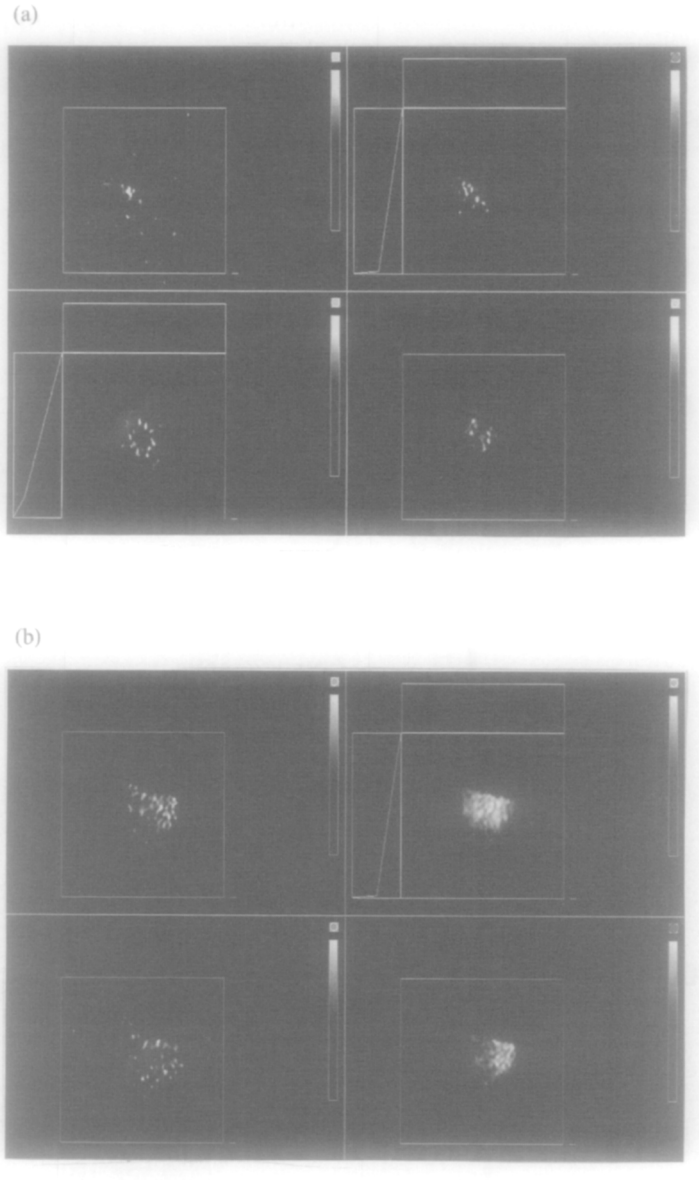

Fig. 29. *In situ* T_1 SPRITE image of (a) Witbank and (b) Goonyella coal at various temperature. From top left, T_2^* image at room temperature, T_1-SPRITE image at 425 °C; from bottom left, T_1-SPRITE image at room temperature, T_1-SPRITE image 450 °C.

The mobile component at room temperature is a very important factor for softening and melting as this component changes or expands upon melting. It is clear that T_1 SPRITE is a very powerful technique for deciding the roles of the softening and melting phenomena in coals. In addition, it is clear that the *in situ* variable-temperature NMR imaging method, which is based on T_1 mapping of

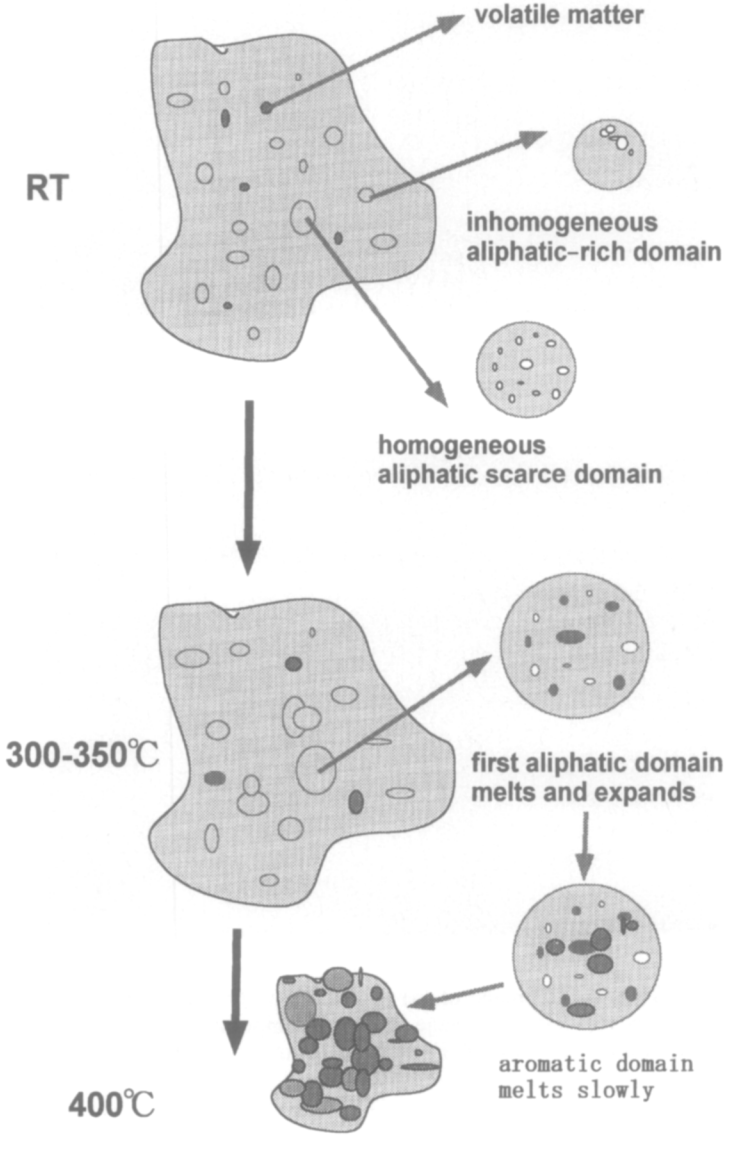

Fig. 30. Proposed mechanism for the softening and melting process in coals.

SPRITE imaging, is a very powerful means of investigating and clarifying the thermal changes of coal as shown in Fig. 29. The information from the T_1 mapping suggests that: first the aromatic domain softens and melts as the trigger for the thermal change of coals; homogeneous distribution of the aromatic domain is a helpful and effective softening property; the aromatic-rich domain of the inhomogeneous distribution disappears as volatile matter. Figure 30 shows the proposed mechanism of the softening and melting processes for coals.

4. APPLICATION OF NMR TO NEW COKING PROCESS DEVELOPMENTS

4.1. Background

The coke ovens available currently have various problems, e.g. restrictions on coal brand such that coal with a high coking property is essential, low productivity, intensive energy-consumption structure, environmental pollution, and so on. In the early 21st century many coke ovens are due for renewal, a difficult process with current oven systems.

To solve these problems, the development of an innovative coke-making process has been underway during the period 1994 to 2001 (SCOPE 21 project).[96] The following technical items have been developed to realize more economical and clean coke plants.[97]

(1) Preheating treatment to give higher utilization of poor coking coals using a rapid heating treatment.
(2) Coking system for higher productivity.
(3) Prevention of environmental pollution.

This section reports studies on item (1) using solid-state NMR methods (^{1}H CRAMPS, ^{13}C CP/MAS and ^{13}C DD/MAS) and NMR imaging methods. The behaviour from 300 to 550 °C of preheated coals is described using the newly developed high temperature *in situ* imaging system to clarify the effects of rapid heating on coal properties.[98]

4.2. Structural analysis

To adjust the temperature of coal that has been subjected to a rapid heating treatment to a specified level, the inlet gas temperature of the preheater was controlled between 350 and 550 °C and the inlet gas velocity was controlled to 20 m s^{-1}. To estimate the particle temperature of coal, a heat transfer model was derived taking account of heat transfer between the particles and gas. The particle temperature (average of the estimated temperature of particles of size 2–3 mm) estimated by simulation was 330 to 380 °C and the rate of

temperature increase was 1×10^4 °C min^{-1}, which is a very rapid heating rate (rapid heating sample). For slow heating, the temperature increase rate was 1×10 °C min^{-1} (slow heating sample) in an electric furnace. The coal given the heat treatment was cooled in a nitrogen atmosphere to investigate its properties using IR and NMR. After the carbonization process for three samples (raw sample, rapid heating sample, slow heating sample), the coke strength was evaluated using the JIS drum index, DI_{15}^{150} through a shutter test. The rapid heat treatment of coal raised the DI_{15}^{150} by almost 6 points at 380 °C, compared to the raw and slow heating samples.

All ^1H(300.5 MHz), and ^{13}C(75.6 MHz) high-resolution solid-state NMR experiments were performed on a Chemagnetics CMX-300 (7.5 T) spectrometer at room temperature, using MAS with a spinning speed of 16 000 Hz except for the case of CRAMPS. The ^1H chemical shifts were calibrated through the signal for the silicone-rubber peak (0.3 ppm relative to tetramethylsilane). The ^1H relaxation measurements were performed with Maciel's pulse sequence[61] which is based on CRAMPS using a spin lock field of 93 kHz.

For the ^{13}C CP/MAS measurement and dipolar-dephasing CP/MAS NMR the experimental conditions were 3 ms contact time, 5 s repetition time, 40 kHz spectral width, and 8 k data points. The ^{13}C chemical shifts were calibrated through the hexamethylbenzene peak (17.3 ppm relative to tetramethylsilane). The ^{13}C relaxation measurements were performed with Torchia's pulse sequence.[99]

The volatile matter was measured according to JIS M8812. This indicated that in the case of the heating rate having been set to 1×10^4 °C min^{-1}, the volatile matter was restrained from decreasing and even at the softening temperature, the volatile matter was maintained at a high level. H/C and O/C were kept high at the same level. It was found that there was no difference in the IR differential spectrum between raw coal and the rapid heating coal. On the other hand, when the heating rate was 10 °C min^{-1}, the volatile matter began to decrease from around 200 °C and at the softening temperature, a noticeable decrease of the volatile matter was seen. Reduction in H/C and O/C was conspicuous. Comparing the IR spectrum at 10 °C min^{-1} with the raw coal, the aliphatic CH stretch (2910 to 2840 cm^{-1}) was greatly decreased, but there was no change in the aromatic >C=C< stretch (1600 cm^{-1}).

According to these basic results, there is almost no chemical change detected by using elemental analysis and IR in the case of rapid heating (10^4 °C min^{-1}). Many NMR techniques were applied to clarify the properties of coal changes by the rapid heating process from the standpoint of the physical and chemical structures.

Table 2 shows the results obtained by CP/MAS, DD/MAS and dipolar-dephasing CP/MAS measurements. Assignment and analysis of the spectra were followed as in past work.[100] It is found that the results for raw coal and coal heated at 10^4 °C min^{-1} are in accord with each other. A similar tendency is found with the results of all three types of NMR measurements. When

Table 2. Integrated ^{13}C NMR intensities of the three coals

Coal	Technique	Integrated intensity sp2	sp3	Derlin
No treatment	CP/MAS	32.8	24.7	10
	Dipolar-Dephasing	38.5	21.7	10
	DD/MAS	27.1	19.6	10
Slow heating	CP/MAS	30.8	24.0	10
	Dipolar-Dephasing	35.1	25.1	10
	DD/MAS	25.2	20.1	10
Rapid heating	CP/MAS	31.9	23.9	10
	Dipolar-Dephasing	38.4	21.3	10
	DD/MAS	26.9	19.4	10

Relative concentration (%)

comparing Table 2 in the case of the slow heating sample with the raw coal, the peak intensity of sp2 carbon regions is clearly decreasing, with the same tendency in all of the NMR measurements. It becomes clear that when heating is set at 10^4 °C min^{-1}, compared with the case of the 10 °C min^{-1} heating rate the bridge-forming reaction due to a covalent bond arising in the step with thermal decomposition and desorption of a low-molecular component can be suppressed perfectly. It is well known that the amount found by CP/MAS in signal intensity is lower than that of DD/MAS in coals because of cross-polarization efficiency. But from the viewpoint of measurement times, DD/MAS needs much longer than CP/MAS.

Table 3 and Fig. 31 show the measurement results obtained using the CRAMPS method. Assignment follows Maciel's results.[101] The most difficult chemical shift assignment to make, and the most uncertain estimate of intensity, are for the broad peak at around 10.5–12 ppm. However, there is no significant difference between the raw coal and the rapid heating coal except for this region, which corresponds to that of carboxyl groups which could be

Table 3. Integrated ^{1}H CRAMPS intensities of the three coals

Coal	Peak (ppm) 1–1.8	2.0–2.5	3.5–4.5	6.8–7.2	8.3–9.0	10.5–12.0
No treatment	95.9	44.6	64.4	100	19.4	13.6
Slow heating	89.9	39.5	62.5	100	19.9	11.5
Rapid heating	95.0	45.2	63.9	100	22.9	7.7

Relative concentration (%)

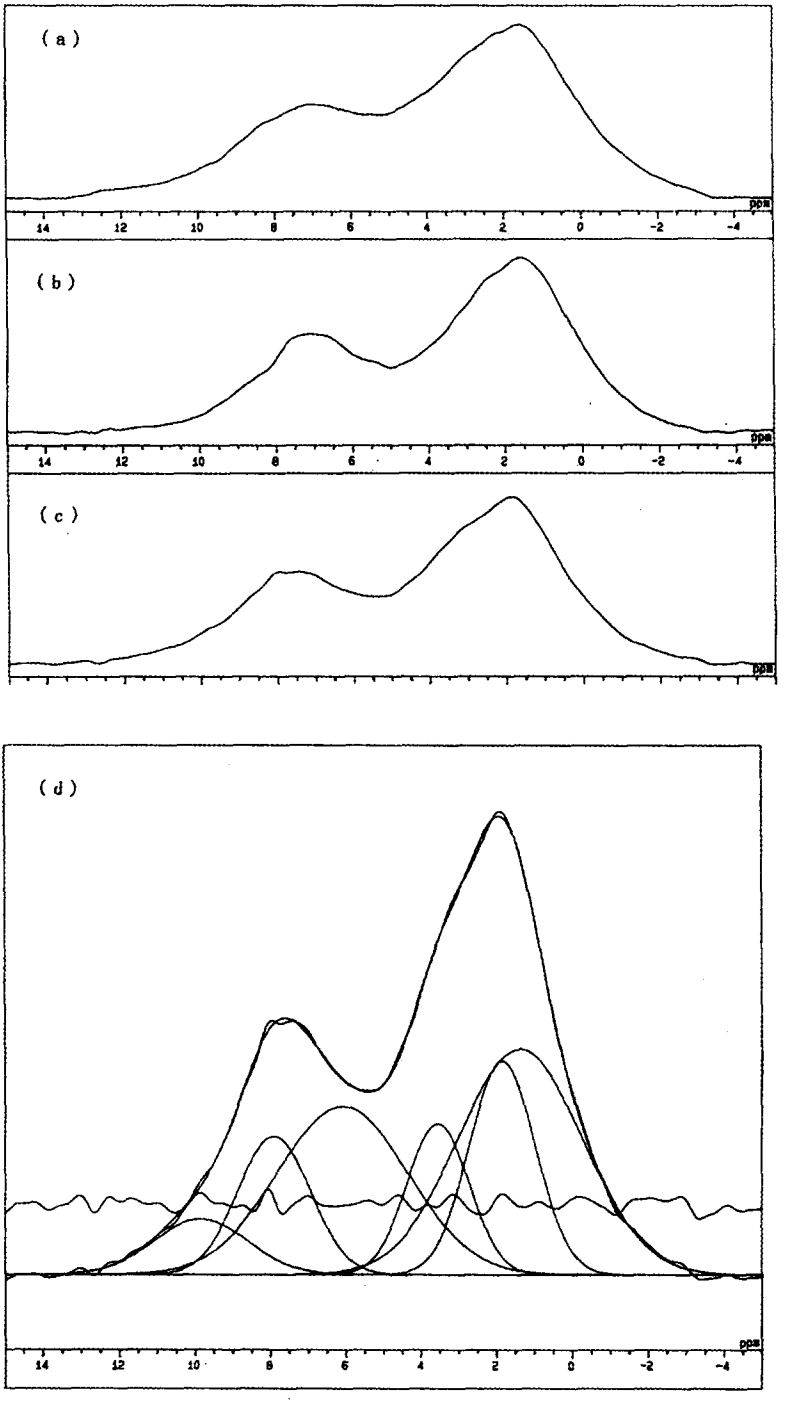

Fig. 31. CRAMPS spectra of coals: (a) raw coal; (b) slow heating coal; (c) rapid heatin coal; (d) deconvoluted contributions for rapid heating coal.

hydrogen-bonded. It is reported that this broad peak is caused by a large dipolar coupling due to a hydrogen-bonded structure, which is indicated by dipolar dephasing data on Blind Canyon coal.[101] According to these and the above-mentioned facts, rapid heating could break the hydrogen bonds.

A model which takes account of the non-covalent bond network structure (cohesion structure) is provided by assuming intermolecular interactions[102] (e.g. hydrogen bonding, $\pi - \pi$ interaction, etc.) to be a dominant factor of coal molecular structure. When taking coal thermal decomposition reactions into account, the importance of intermolecular interactions has been stressed. Rapid heat treatment could be made to control coal thermal decomposition by changing the non-covalent bond network structure. In the case of slow heating with raw coal, the peak intensity of the aliphatic regions is clearly decreasing as shown by the ^{13}C measurements.

Table 4 shows the results obtained by the ^{1}H wide line NMR method. For coal molecular structure, a 'two-phase model' is widely accepted which comprises a high mobility component and a low mobility component.[103] Therefore, the wide line spectra have been analysed using a deconvolution technique that separates spectra into mobile and immobile components. It is clear that the amount of mobile component is increased in the case of both rapid and slow heating treatments. The rapid heating treatment in particular has a large effect on the increase of the mobile component because of the changes to the non-covalent bond network structure and the molecular structure.

Table 5 shows the various relaxation parameters derived for the three kinds of coal. The relaxation times of the ^{13}C nuclei in coal subjected to the rapid heating treatment are shorter than the relaxation times in raw coal. It is likely that the molecular mobility of coal becomes high because of the changes to the non-covalent bond network structure and the molecular structure of relaxation. In general, comparison of the relaxation parameters is difficult in coals because of the influence of various magnetic susceptibilities (some mineral components and some paramagnetic components).[104] The relaxation parameters of ^{1}H nuclei show some change caused by the rapid heating treatment. Because the main relaxation mechanism in coal is time-dependent $^{1}H-^{1}H$ dipolar interactions, two $T_{1\rho}$ values are identified for each of the three coal samples studied, indicating the existence of structural heterogeneity. In

Table 4. Integrated ^{1}H wide-line NMR of the three coals

Coal	Mobile (%)[a]	Immobile (%)[a]
No treatment	45.6	100
Slow heating	54.4	100
Rapid heating	70.1	100

[a] Relative value (%)

Table 5. Relaxation parameters derived for the three coals

Coal	T_1C (s)	(%)[a]	T_1C_ρ (ms)	(%)	T_{CH}[b] (ms)	T_1H (s)	(%)	T_1H_ρ (ms)	(%)
No treatment									
sp2									
slow component	2.44	57	191	68	0.25	0.67	14	12	67
fast component	1.51	43	90	32		0.066	86	3.1	33
sp3									
slow component	0.98	55	29.5	64	0.09	0.38	25	9	68
fast component	0.14	45	13.1	36		0.055	75	3.4	32
Slow heating									
sp2									
slow component	1.95	47	165	47	0.25	0.61	13	5	70
fast component	1.32	53	72	53		0.061	87	2.8	30
sp3									
slow component	0.45	42	24.4	41	0.09	0.29	20	3	70
fast component	0.09	58	8.7	59		0.047	80	2.9	30
Rapid heating									
sp2									
slow component	1.85	40	94	35	0.35	0.34	15	9	71
fast component	1.08	60	47	65		0.050	85	2.5	29
sp3									
slow component	0.27	38	20.5	38	0.13	0.29	23	8	72
fast component	0.07	62	6.1	62		0.047	77	2.1	28

[a] Relative value (%) [b] Average value

particular, the rapid heating treatment has a strong impact on changes in the suppression of structural heterogeneity.

Figure 32(a) show a 3D-SPRITE image of raw coal. The lighter areas in this sample correspond to higher concentrations of the mobile component, as the conditions of this SPRITE experiment were set to the T_2^* value of the mobile component. It is obvious that the SPRITE results give significantly clearer images than those for the same sample obtained by the standard spin-echo imaging sequence with swelling due to pyridine-d_5. Figure 32(b) shows nine representative 2D-images that are sequential planes for rapid heating coal obtained from 3D-SPRITE measurements. There is a significant difference between the results for the raw coal and those for the rapid heating coal concerning the distribution of the mobile component. Table 6 shows that the amount of mobile components in the rapid heating coal (23%) is much more than in the raw coal. In the case of the slow heating coal, Fig. 32(c) shows that there is almost no change in the distribution of the mobile component when compared to raw coal. Thus is appears that changing the non-covalent bond network structure and the molecular structure of relaxation are dominant factors in determining the influence of rapid heating on coal molecular structure.

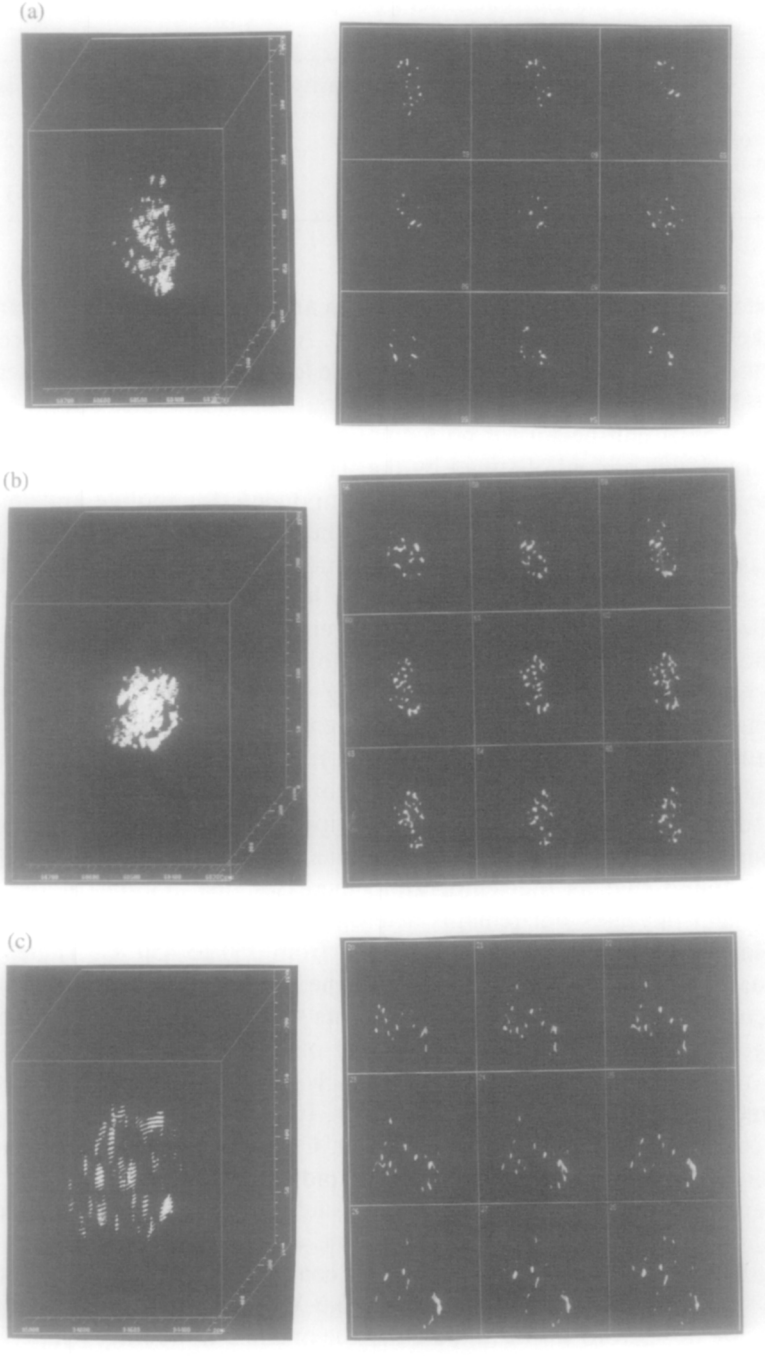

Fig. 32. NMR 3D and 2D images of (a) raw coal; (b) rapid heated coal; and (c) slow heated coal obtained by single-point imaging.

Table 6. Integrated intensities and average sizes of the mobile component from NMR images of the three coals

Coal	Integrated intensity (%)	Average size (μm)
Raw coal	17.1	55
Rapid heated coal	20.9	78
Slow heated coal	18.4	51

It is well known that coals start to soften and melt at about 400 °C and then to cake and carbonize at more than 450 °C. A solid echo pulse sequence with a refocusing of 4 μs was used to minimize the loss of signal due to the dead time of the NMR coil. Figure 33 shows the variations in the rates and their signal half-widths at half-height for both components between 25 °C and 550 °C for the three kinds of coal obtained by the ^{1}H wide line method.

The spectra are deconvoluted into components for mobile and immobile phases. As the temperature increases, the rate of the mobile component increases gradually and shows maximum mobility at about 400 °C for the raw coal, corresponding to a minimum in the half-width values. The rate of the mobile component reduces suddenly at over 475 °C. It is clear that the rate of the mobile component at the maximum mobility temperature is much greater than in both raw coal and slow heating coal. This means that the rapid heating treatment gives some improvement in coal properties in both the softening and the melting temperature range. It is very interesting that changing the non-covalent bond network structure and the molecular structure of relaxation have some relationship to the coal softening and melting temperature range.

It is found that as the temperature increases, the amount of the mobile component increases but remains heterogeneous at first, then the rate of the mobile component increases dramatically from 350 to 450 °C. Therefore, we propose the following mechanism for the softening and melting process. Stretching of the mobile components occurs since some immobile components change to mobile components as a result of the heating process, and at the same time some mobile components, which have good fluidity initially, melt and move slowly to other areas. However, Fig. 34(a) and (b) show images of raw coal and slow heating coal at 400 °C, the temperature of maximum mobility. Figure 34(c) shows images of rapid heating coal, also at 400 °C, the temperature of maximum mobility. It is surprising that the figures show low mobility areas and that there remain some unsoftened areas, in spite of this being the maximum mobility for the raw coal and the slow heating coal. It is likely that low-rank coals for coking, like Witbank, have some inert areas which are difficult to soften and melt at the maximum mobility temperature in this specimen. In the case of rapid heating, the unsoftened areas become much smaller. The fact that the rapid heat treatment of coal raised the DI_{15}^{150} by

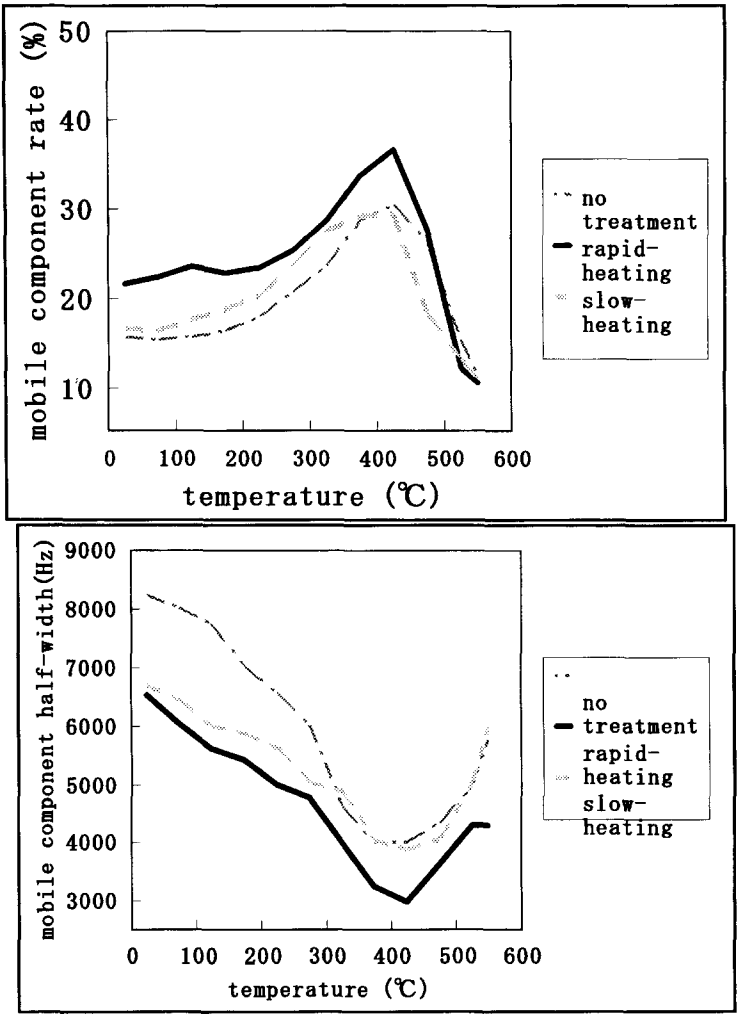

Fig. 33. Relationships between the fractional intensity (or their half-width) of the mobile component and temperature for the three coals; raw coal, rapid heated coal and slow heated coal.

almost six points at 380 °C (compared to the raw sample and the slow heating sample) is mainly caused by a decrease in the unsoftened area. Rapid heat treatment causes the cohesion of coal molecules to relax and the kinetic properties of the molecules to increase. A bridge-forming reaction generated by slow heating is suppressed, the high-mobility component increases and the softening and melting phenomena are accelerated due to coking.

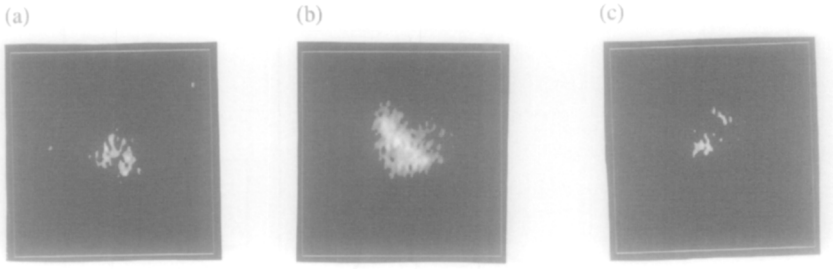

Fig. 34. *In situ* NMR images of the three coals at the maximum mobility temperature, 400 °C: (a) raw coal; (b) rapid heated coal; (c) slow heated coal.

4.3. Clarification of mechanism

A new carbonization process with rapid preheating and coke discharging at medium temperature has been developed. The results using this process show that even when very poor coking coal is present (50 wt%), the coking property is improved and a coking coke with a cold strength usable in a blast furnace can be manufactured with the new carbonization process. The mechanism of the coking property improvement was examined in terms of coal properties using solid-state NMR (^{1}H CRAMPS and ^{13}C DD/MAS, CP/MAS) and NMR imaging (SPRITE imaging, *in situ* imaging). To monitor the dynamic changes in coals with temperature, an *in situ* method must be used, therefore, single-point imaging has been applied to carry out the first systematic *in situ* variable-temperature NMR imaging study of coals between 25 and 500 °C.

The following mechanism is proposed for this rapid heating treatment which produces an improvement in coal properties.

Coals have mobile and immobile components that are based on the non-covalent bond network structure. Rapid heating treatment produces no significant chemical reaction but results in molecular structure relaxation.

Thus the mobile component increases at the maximum mobility temperature giving a signal half-width for the mobile component which decreases at this temperature. Hence the unsoftened area becomes smaller and the softening and melting phenomena accelerate as the time of coking increases.

5. CONCLUSIONS

Coal is a very complex material. Although ^{13}C CP/MAS can provide much information on coals, there are very similar molecular structures in coals, so that an approach using multinuclear NMR is very helpful in understanding

coal structure, overcoming the limited chemical information obtained from ^{13}C CP/MAS. In particular, direct chemical information from nitrogen and proton NMR measurements is helpful in producing a coal structure model. Additionally, spectral editing techniques and advanced MQMAS data show much more chemical information for coals.

Recently modified SPI, single-point ramped imaging with T_1 enhancement (SPRITE), consists of a ramped phase encode gradient in the primary phase encode direction and conventional phase encode gradients in the other directions. The use of a ramped phase gradient permits imaging with greater speed and with a lower dB/dt value, which minimizes gradient vibration when compared with SPI. At the same time, a great time improvement is achieved with samples where T_1 relaxation times are of the order of the gradient rise time. Magnetization preparation is easily incorporated into the SPRITE sequence by sampling a single k-space point after each magnetization filter application. 3D-SPRITE has been shown to be successful for studying short relaxation time systems which are free from distortions due to susceptibility variations for coals at a frequency of 400 MHz. The results obtained are discussed in relation to the three-dimensional distribution of mobile components in several kinds of coal. At the same time, inversion recovery preparation experiments (T_1 mapping) and T_2^* mapping based on SPRITE methods are presented to clarify the chemical heterogeneity of coals. Thermally induced changes in coals are interesting from the standpoints of both fundamental and applied research for the iron-making process. Furthermore, for very inhomogeneous coals, there is a fascination with the influence of thermal dynamic changes. To monitor the dynamic changes in coals with temperature, an *in situ* method must be used because it is well known that the properties of coals change dramatically in the high temperature region (from 350 to 550 °C). This chapter thus reports the first systematic *in situ* high-temperature NMR microimaging study of coals between 25 and 550 °C with systems chosen to clarify the behaviour of the mobile component in coal specimens at high temperatures. Finally, the application of recent NMR techniques to new coking process developments in the 21st century have been demonstrated. It is clear that coal is very inhomogeneous and complex, and at the same time, from the viewpoint of energy, coal is very important. The authors believe that NMR is very powerful, effective and the best tool not only to characterize coal structures and clarify their behaviour at high temperature but also to develop new processes.

ACKNOWLEDGEMENTS

The authors are grateful to Professor Dr B. Bluemich (RWTH-Aachen), and Dr R. E. Botto (Argonne National Laboratory) for helpful discussions and suggestions.

REFERENCES

1. H. L. Retcofsky and T. A. Link, in *Analytical Method for Coal and Coal Products*, Academic Press, San Diego, 1978, Volume 2, Chapter 24.
2. D. H. Scott, *Developments Affecting Metallurgical Uses of Coal*, IEACR/74, IEA Coal Research, London, 1994.
3. R. E. Winans and J. C. Crelling, *Chemistry and Characterization of Coal Macerals*, American Chemical Society Symposium Series No. 252, ACS, Washington, DC, 1984.
4. P. D. Murphy, B. C. Gerstein, V. L. Weinberg and T. F. Yen, *Anal. Chem.*, 1982, **54**, 522.
5. P. C. Newman, L. Pratt and R. E. Richards, *Nature* (London), 1955, **125**, 645.
6. D. L. Vanderhart and H. L. Retcofsky, *Fuel*, 1976, **55**, 202.
7. A. Pines, M. G. Gibby and J. S. Waugh, *J. Chem. Phys.*, 1972, **15**, 1776.
8. V. J. Bartuska, G. E. Maciel, J. Schaefer and E. O. Stejskal, *Fuel*, 1977, **56**, 354.
9. S. L. Dieckman, N. Gopalsami and R. E. Botto, *Energy Fuels*, 1990, **4**, 417.
10. D. C. French, S. L. Dieckman and R. E. Botto, *Energy Fuels*, 1993, **7**, 90.
11. L. Hou, G. D. Cody, P. G. Hatcher, S. Gravina and M. A. Mattingly, *Fuel*, 1994, **73**, 199.
12. D. G. Cody and R. E. Botto, *Energy Fuels*, 1993, **7**, 561.
13. K. S. Vorres, in *Kirk-othmer Encyclopedia of Chemical Technology*, 4th edn, Wiley, New York, 1993, Volume 6.
14. B. C. Gerstein, C. Chou, R. G. Pembleton and R. C. Wilson, *J. Phys. Chem.*, 1977, **81**, 565.
15. C. E. Bronnimann and G. E. Maciel, *Org. Geochem.*, 1989, **14**, 189.
16. D. P. Burum and W. K. Rhim, *J. Chem. Phys.*, 1979, **71**, 944.
17. A. Jurkiewicz, C. E. Bronnimann and G. E. Maciel, *Fuel*, 1989, **68**, 782.
18. A. Jurkiewicz, C. E. Bronnimann and G. E. Maciel, *Fuel*, 1990, **69**, 804.
19. A. Jurkiewicz, C. E. Bronnimann and G. E. Maciel, in *Magentic Resonance of Carbonaceous Solid*, eds R. E. Botto and Y. Sanada, **ACS 229**, American Chemical Society, Washington, DC, 1993, p. 401.
20. K. Saito, M. Hatakeyama and I. Komaki, *Proceedings of Japan NMR Conference*, Kyoto, 1996, **35**, 16.
21. J. Larsen, *J. Am. Chem. Soc. Div. Fuel Chem. Reprint*, 1990, **35**, 376.
22. W. H. Wiser, *J. Am. Chem. Soc. Div. Fuel Chem. Reprint*, 1975, **20**, 122.
23. P. R. Solomon, in *New Approaches in Coal Chemistry*, Symposium Series 169, American Chemical Society, Washington, DC, 1981, 61.
24. J. H. Shinn, *Fuel*, 1984, **63**, 1187.
25. M. S. Solum, R. J. Pugmire and D. M. Grant, *Energy Fuels*, 1989, **3**, 187.
26. L. Dela Rosa, M. Pruski, D. Lang, B. Gerstein and P. R. Solomon, *Energy Fuels*, 1992, **6**, 460.
27. D. E. Axelson, *Solid State Nuclear Magnetic Resonance of Fossil Fuels*, Multiscience, 1985.
28. R. M. Davidson, *Nuclear Magnetic Resonance Studies of Coal*, IEACR/32, IEA Coal Research, London, 1986.
29. M. Alla and E. Lippmaa, *Chem. Phys. Lett.*, 1976, **37**, 260.
30. X. Wu, S. T. Burns and ZK. W. Zilm, *J. Magn. Reson.*, 1994, **A111**, 29.
31. M. Hatakeyama, K. Saito, H. Sugisawa and K. Deguchi, *Proceedings of Japan NMR Conference*, Tokyo, 2000, **39**, 370.
32. K. Stancyzyk, R. Dziembaj, Z. Ptwowarska and S. Witkowshi, *Carbon*, 1995, **33**, 1383.
33. J. C. Facelli, R. J. Pugmire and D. J. Grant, *J. Am. Chem. Soc.*, 1996, **118**, 5488.
34. K. Saito, M. Hatakeyama and I. Komaki, *Proceedings of Japan Coal & Science Meeting*, Tsukuba, 1998, **35**, 343.
35. R. A. Wind, M. J. Duijvestijn, C. van der Lugt, A. Manenshijn, J. Smidt and J. Vriend, *Fuel*, 1987, **66**, 876.
36. R. S. Kelemen, M. L. Gorbaty and P. J. Kwiatek, *Energy Fuels*, 1994, **8**, 896.

37. A. Jurkiewicz, R. A. Wind and G. E. Maciel, *Fuel*, 1990, **69**, 830.
38. K. Kanehashi and K. Saito, *CAMP-ISIJ*, 2000, **13**, 1443.
39. J. R. Barnes, A. D. H. Clague, N. J. Claydent, C. M. Dobson and R. B. Jones, *Fuel*, 1986, **65**, 437.
40. M. A. Wilson, B. C. Young and K. M. Scott, *Fuel*, 1986, **65**, 1584.
41. L. Frydman and J. S. Harwood, *J. Am. Chem. Soc.*, 1995, **117**, 5367.
42. J. P. Amoureux, C. Fernandez and S. Steuernagel, *J. Magn. Reson.*, 1996, **A123**, 116.
43. K. Kanehashi, K. Saito and H. Sugisawa, *Chem. Lett.*, **2000**, 588.
44. K. Kanehashi and K. Saito, *Solid State NMR*, 2001, **6**.
45. S. Hayashi, T. Ueda, K. Hayamizu and E. Akiba, *J. Phys. Chem.*, 1992, **96**, 10922.
46. J. Rocha, *J. Phys. Chem. B*, 1999, **103**, 9801.
47. B. Bluemich and W. Kuhn, eds, in *Magnetic Resonance Microscopy*, VCR, Weinheim, 1992.
48. B. Bluemich, P. Bluemler and K. Saito, in *Solid State NMR of Polymers*, Elsevier, Amsterdam, 1998, p. 123.
49. S. Emid and J. H. N. Creyghton, *Physica*, 1985, **128B**, 81.
50. D. E. Axelson, A. Kantzas and T. Eads, *Can. J. Appl. Spectrosc.*, 1995, **40**, 16.
51. S. D. Beyea, B. J. Balcom, P. J. Prado, A. R. Cross, C. B. Kennedy, R. L. Armstrong and T. W. Bremner, *J. Magn. Reson.*, 1998, **135**, 194.
52. S. Choi, X.-W. Tang and D. G. Cory, *J. Imaging Syst. Technol.*, 1997, **8**, 263.
53. S. Gravina and D. G. Cory, *J. Magn. Reson.*, 1994, **B104**, 53.
54. I. V. Mastikhin, B. J. Balcom, P. J. Prado and C. B. Kennedy, *J. Magn. Reson.*, 1999, **136**, 159.
55. K. Saito, I. Komaki, K. Hasegawa and H. Tsuno, *Fuel*, 2000, **79**, 405.
56. K. Saito, M. Shinohara, K. Hasegawa and H. Tsuno, *Bull. Magn. Reson.*, 1995, **18**, 154.
57. K. Saito, M. Hatakeyama, M. Matsuura and I. Komaki, *Tetsu-to-Hagane*, 1999, **85**, 111.
58. R. E. Winans and J. C. Crelling, *Am. Chem. Ser.*, No. 252, American Chemical Society, Washington, DC, 1984.
59. D. W. van Krevelen, *Coal*, 3rd revised edn, Elsevier: Amsterdam 1993; Chapters 23, 24.
60. B. C. Gerstein, P. D. Murphy and L. M. Ryan, in *Coal Structure*, ed. R. A. Meyers, Academic Press, New York, 1982, Chapter 4.
61. X. Jincheng and G. E. Maciel, *Energy Fuels*, 1997, **11**, 866.
62. I. G. C. Dryden and K. S. Pankhurst, *Fuel*, 1955, **34**, 363.
63. J. Hager, *J. Soc Chem. Ind.*, 1914, **33**, 389.
64. S. Rillingworth, *Fuel*, 1922, **1**, 213.
65. I. G. C. Dryden and K. S. Pankhurst, *Fuel*, 1955, **34**, 363.
66. D. Fitzgerald, *Fuel*, 1956, **35**, 178.
67. D. W. van Krevelen, F. J. Hntjensm and H. N. M. Dormans, *Fuel*, 1956, **35**, 462.
68. H. A. G. Chermain and D. W. van Krevelen, *Fuel*, 1957, **36**, 85.
69. D. Fitzgerald and D. W. van Krevelen, *Fuel*, 1959, **38**, 17.
70. I. G. Dryden and W. K. Joy, *Fuel*, 1961, **40**, 473.
71. K. Ouchi, *Fuel*, 1961, **40**, 485.
72. H. R. Brown and P. L. Waters, P. L., *Fuel*, 1966, **45**, 17.
73. H. R. Brown and P. L. Waters, *Fuel*, 1966, **45**, 41.
74. T. K. Green and J. W. Larsen, *Fuel*, 1984, **63**, 138.
75. K. Miyazawa, T. Yokono and Y. Sanada, *Carbon*, 1979, **17**, 223.
76. T. Parks, L. F. Cross and L. J. Lynch, *Carbon*, 1991, **7**, 921.
77. R. Sakurovs, L. J. Lynch, T. P. Maher and R. N. Banerjee, *Energy Fuels*, 1987, **1**, 167.
78. L. J. Lynch and D. S. Webster, *Am. Chem. Soc. Symp. Ser.*, 1983, No. 230, 353.
79. L. J. Lynch, D. S. Webster, R. Sakurovs, W. A. Barton and T. P. Maher, *Fuel*, 1988, **67**, 579.
80. L. J. Lynch, D. S. Webster and W. A. Barton, *Adv. Magn. Reson.*, 1988, **12**, 385.
81. A. H. Clemens, T. W. Matheson, L. J. Lynch and R. Sakurovs, *Fuel*, 1989, **68**, 1162.
82. R. Sakurovs, L. J. Lynch and W. A. Barton, *Adv. Chem. Ser.*, 1993, No. 229, 229.

83. R. Sakurovs and L. J. Lynch, *Fuel*, 1993, **72**, 743.
84. L. J. Lynch, R. Sakurovs, D. S. Webster and P. J. Redlich, *Fuel*, 1988, **67**, 1036.
85. M. Mercedes Maroto-Valer, J. M. Andresen and C. E. Snape, *Energy Fuels*, 1997, **11**, 236.
86. M. Mercedes Maroto-Valer, J. M. Andresen and C. E. Snape, *Fuels*, 1997, **76**, 1301.
87. K. Hayamizu, S. Hayashi, K. Kamiya and M. Kawamura, *Adv. Chem. Ser.*, 1993, No. 229, 15.
88. M. S. Solum, R. J. Pugmire and D. M. Grant, *Energy Fuels*, 1989, **3**, 187.
89. E. Stach, M.-Th. Mackowsky, M. Teichmuller, G. H. Taylor, D. Chandra and R. Teichmuller, *Stach's Textbook of Coal Petrogy*, 2nd edn, Gebruder Borntaeger, Berlin, 1975.
90. K. Hasegawa, R. Yamakoshi, H. Tsuno and K. Saito, *Proceedings of 13th-ISMAR*, Berlin, 1998, **1**, 396.
91. K. Saito, I. Komaki, K. Hasegawa and H. Tsuno, *Proceedings of 13th-ISMAR*, Berlin, 1998, **2**, 581.
92. R. Turner and R. M. Bowley, *J. Phys. E.*, 1986, **19**, 876.
93. A. Davis, in *Analytical Methods for Coal and Coal Products*, Academic Press, New York, 1978, p. 27.
94. S. Nomura, K. Katoh, I. Komaki, Y. Fujioka, K. Saito and I. Yamaoka, *J. Jpn. Inst. Energy.*, 1998, **77**, 55.
95. K. Saito, M. Shinohara and A. Suzuki, *Proceeding of EENC*, Paris, 1996, **1**, 318.
96. K. Nishioka, *Tetsu-to-Hagane*, 1996, **82**, 353.
97. M. Sasaki, I. Komaki, M. Matsuura, K. Saito and K. Fukuda, *ICSTI-98*, 1998, 33, 44.
98. K. Saito, M. Hatakeyama, M. Matsuura and I. Komaki, *Tetsu-to-Hagane*, 2000, **86**, 79.
99. D. A. Tochia, *J. Magn. Reson.*, 1978, **30**, 613.
100. K. Kidena, S. Murata and M. Nomura, *Energy Fuels*, 1996, **10**, 672.
101. A. Jurkiewick, C. E. Bronnimann and G. E. Maciel, *Fuel*, 1994, **73**, 823.
102. T. Takanohashi, T. Yoshida, T. Iino, K. Katoh and K. Fukada, *Tetsu-to-Hagane*, 1996, **82**, 22.
103. X. Yang, J. W. Larsen and B. G. Silbernagel, *Energy Fuels*, 1993, **7**, 439.
104. J. A. Franz, A. Garcia, J. C. Linehan G. D. Love and C. E. Snape, *Energy Fuels*, 1992, **6**, 598.

NMR Study of Strongly Correlated Superconductors

K. ASAYAMA, Y. KITAOKA, G-q. ZHENG, K. ISHIDA and Y. TOKUNAGA

Department of Physical Science, Graduate School of Engineering Science, Osaka University, Toyonaka, Osaka 560-8531, Japan

1. INTRODUCTION

Since the discovery of the heavy fermion ($CeCu_2Si_2$ 1975)[1] and high-T_c superconductors ($(La, Ba)_2CuO_4$ 1986),[2] a large number of studies have been carried out to explore the magnetic and superconducting properties of these systems. NMR measurements have played an important role in these investigations. Although the magnitude of the superconducting transition temperature, T_c, is different for the heavy-fermion and high-T_c materials, they have a common aspect in the sense that both are strongly correlated electron

ANNUAL REPORTS ON NMR SPECTROSCOPY
VOLUME 44 ISBN 0-12-505344-4

systems. It is clear that the superconductivities in both systems are anisotropic as discussed later, indicating that the attractive force for the Cooper pairs is not due to phonon, but to electron interactions. This review will introduce NMR studies on heavy fermion and high-T_c superconductors together with the related compounds, Sr_2RuO_4 and YNi_2B_2C, which have been performed at Osaka University, including results from other groups. Although some of the results have been reviewed previously,[3] we repeat them here in connection with new results.

2. NMR QUANTITIES IN THE SUPERCONDUCTING STATE

In general the Cooper pairs in conventional superconductors induced by phonons have s-symmetry where the gap opens uniformly on the Fermi surface and the temperature dependence of physical quantities below T_c is exponential. On the other hand, when the attractive force originates from spin or electron charge fluctuations, the Cooper pair has p- or d-wave symmetry where the gap disappears on lines or points on the Fermi surface and the physical quantities have power-law temperature dependences. The quantities that are measured by NMR and nuclear quadrupole resonance (NQR) are the nuclear spin-lattice relaxation rate, $1/T_1$, the Knight shift, K, the spin echo decay rate, $1/T_2$ and the NQR frequency, ν_Q. The most important quantities, K and $1/T_1$ for the determination of the symmetry of the Cooper pairs are reviewed in the following sections.

2.1. Nuclear spin-lattice relaxation rate ($1/T_1$)

$1/T_1$ in the superconducting state is expressed as,

$$\frac{1}{T_1} = \frac{\pi A^2 \alpha(T)}{\hbar} \int \{N_s^2(E) + M_s^2(E)\} f(E)\{1 - f(E)\} dE \tag{1}$$

Here $\alpha(T)$ expresses an enhancement factor due to an electron correlation effect. We neglect the temperature dependence of $\alpha(T)$ for the present. A is the hyperfine coupling constant when the δ function interaction is assumed. In the case when the transferred hyperfine coupling depends on the neighbouring spins, A is no longer constant but wavenumber dependent as will be mentioned later. E and $f(E)$ are the energy of the quasiparticles and the Fermi function, respectively. The density of states of the quasiparticles $N_s(E)$ and the anomalous density of states $M_s(E)$ associated with the coherent effect are expressed as follows:

$$N_s(E) = \frac{N_0}{4\pi} \int_\Omega \frac{E}{\sqrt{E^2 - \Delta^2(\theta, \phi)}} d\Omega \qquad M_s(E) = \frac{N_0}{4\pi} \int_\Omega \frac{\Delta(\theta, \phi)}{\sqrt{E^2 - \Delta^2(\theta, \phi)}} d\Omega \tag{2}$$

For the s-wave with isotropic gap Δ_0, Eq. (2) is simplified to

$$N_s(E) = N_0 \frac{E}{\sqrt{E^2 - \Delta_0^2}} \qquad M_s(E) = N_0 \frac{\Delta_0}{\sqrt{E^2 - \Delta_0^2}} \tag{3}$$

Figure 1 shows the density of states for the isotropic s- and p-waves, and two-dimensional d-wave pairing,[4] respectively. For the isotropic s-wave pairing $N_s(E)$ and $M_s(E)$ have a strong divergence at the gap edge which leads to an increase in $1/T_1$ just below T_c. At low temperatures $1/T_1$ decreases exponentially. When the gap disappears on a line or points on the Fermi surface for p- or d-wave pairing, the divergence at the gap edge is weak, as seen in Fig. 1. In the case of a line node, $N_s(E) \sim E$ for small E which leads to a T^3 dependence in $1/T_1$ at $T \ll T_c$. In the triplet p-wave case $M_s(E) = 0$, and for d-wave pairing $\Delta(\theta, \phi)$ in $M_s(E)$ disappears when averaged over the Fermi surface. Thus, owing to the absence of $M_s(E)$ and the weak divergence of $N_s(E)$ at the gap edge, the coherence peak just below T_c is either small or absent for an anisotropic superconductor of p- or d-symmetry. Even in the case of s-wave

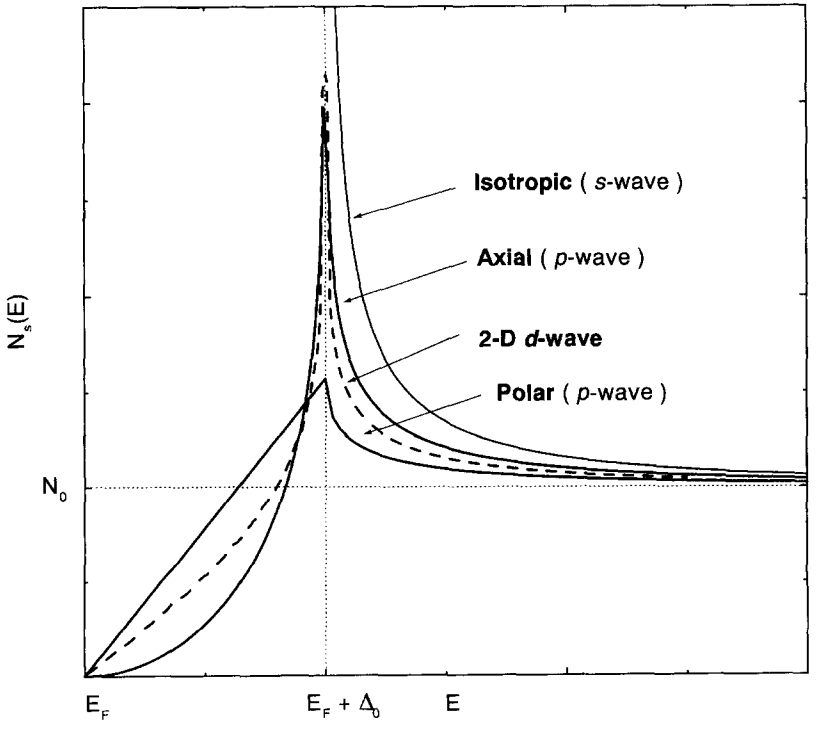

Fig. 1. Density of states for isotropic s-wave and p-wave polar and axial, and the two-dimensional d-wave case.

pairing the coherence peak can be suppressed when the damping of the lifetime of the quasiparticle is large enough to smear the divergence of $N_s(E)$.

2.2. Knight shift

The Knight shift K is composed of the spin part K_s and the Van-Vleck orbital part, K_{VV} in transition metal compounds, where

$$K_s \sim A_s \chi_s / \mu_B \tag{4}$$

$$K_{VV} \sim A_{orb} \chi_{VV} / \mu_B \tag{5}$$

Here A_s and A_{orb} are the hyperfine field due to spin and orbital angular momentum, χ_s and χ_{VV} are the spin and Van Vleck susceptibility, respectively, and μ_B is the Bohr magneton. In a heavy fermion system, where $4f$ or $5f$ electrons play principal roles, the state is specified by $\vec{j} = \vec{l} + \vec{s}$, so that K_s is associated with the ground state (not purely due to spin and temperature dependent in general). K_{VV} is induced from the transition between the ground state and the excited state, and is temperature independent. Each of A_s and A_{orb} includes the spin and orbital hyperfine fields.

For even parity (singlet) pairing, K_s in the superconducting state follows the relation,

$$K_s = A\chi_s = -4A_s\mu_B^2 \int_0^\infty N_s(E) \left(\frac{\partial f}{\partial E} \right) \mathrm{d}E \tag{6}$$

The temperature dependence of K_s at low temperatures is exponential for s-wave pairing. In the case of a d-wave with a line-node gap, the temperature dependence of K_s at low temperatures is linear. $K_{VV} \propto \chi_{VV}$ does not change even below T_c.

For the odd parity (triplet) pairing state in the Anderson–Brinkmann–Morel state, χ_s does not decrease below T_c. When the spin-orbit coupling of the Cooper pairs is strong, the direction of the triplet spin pairs is bound to a crystal axis, which produces no reduction in $\chi_s \sim K_s$ along this axis, while it reduces K_s components perpendicular to this axis. It should be noted that the decrease in the spin Knight shift below T_c is small in the singlet s-wave pairing when the spin flip scattering of the conduction electrons by impurities becomes large.[5] The spin susceptibility in the superconducting state χ_s, normalized by that in the normal state, χ_n, is expressed as follows:

$$\begin{aligned} \frac{\chi_s}{\chi_n} &\simeq 1 - 2\Delta\tau \qquad \text{for } \Delta\tau \ll 1 \\ &\simeq \frac{1}{6\Delta\tau} \qquad \text{for } \Delta\tau \gg 1 \end{aligned} \tag{7}$$

Table 1. Characteristics of superconductivity in several SCES

Characteristic	$CeCu_2Si_2$	UBe_{13}	UPt_3	URu_2Si_2	UPd_2Al_3	UNi_2Al_3	high-T_c	Sr_2RuO_4	YNi_2B_2C
T_c(K)	~0.7	~0.9	~0.55	~1.2	~2	~1	~140 (max)	~1.5	~16
Nucleus for NMR	Cu Si	Be	Pt	Ru Si	Pd Al	Al	Cu O	Ru O	B
c.p.*	no	no	no	no	no	no	no	no	no
$1/T_1$ (low temp.)**	T^3	T^3	T^3	T^3	T^3 (T)	T^3	T^3 (T)	$\sim T^3$ (T)	T
K***	dec.		no	(no)	dec.	(no)	dec.	no	
Parity	even		odd	(odd)	even	(odd)	even	odd	
Symmetry	d		p or f	(p or f)	d	(p or f)	d	p	
Magnetic**** order	comp.		coex.	coex.	coex.	coex.	comp.		

*c.p.: coherent peak. **temperature dependence of $1/T_1$ observed at low temperatures in lower-T_c samples due to the impurity effect. ***dec.: decrease, no: no change. ****comp.: compete, coex.: coexist

where τ is the spin flip time due to impurity scattering and $2\Delta\hbar$ is the energy gap,[5] Recent numerical reanalysis[6] shows that

$$\frac{\chi_s}{\chi_n} \simeq \frac{3}{3+8\Delta\tau} \qquad \text{for all } \Delta\tau \tag{8}$$

For the *d*-wave pairing case, strong impurity scattering destroys the superconductivity itself. The Knight-shift measurement provides the change of χ_s most accurately. However, to distinguish *s* or *d* from the temperature dependence of K is not easy because at low temperatures the dependence is easily affected by impurities in *d*-wave pairing, as discussed later.

In Table 1 are shown the characteristics of the superconductivity in the heavy fermion superconductors, high-T_c superconductors, Sr_2RuO_4 and YNi_2B_2C, which were obtained by NMR measurements. Discussion of each system is given below.

3. HEAVY FERMION (HF) SUPERCONDUCTORS

3.1. Symmetry of the Cooper pairs

At present, the heavy fermion (HF) materials that exhibit superconductivity at ambient pressure are $CeCu_2Si_2$, UBe_{13}, UPt_3, URu_2Si_2, UPd_2Al_3 and UNi_2Al_3. Quite recently, it has been reported that some magnetic Ce compounds such as $CePd_2Si_2$ and $CeIn_3$ show superconductivity at a pressure of ~3 GPa.[7] The temperature dependence of $1/T_1$ in $CeCu_2Si_2$, UPt_3 and UBe_{13} is shown in Fig. 2.[8-10]

In order to discuss the temperature dependence in the superconducting state, it is necessary to know the temperature dependence in the normal state.

$CeCu_6$ and $CeRu_2Si_2$ show neither superconductivity nor magnetic order down to 20 mK. Therefore, the behaviour of $1/T_1$ in these compounds presents a fundamental property of heavy fermion material. As seen in Fig. 3,[11,12] $1/T_1$ is temperature independent above the Kondo temperature, T_K, corresponding to a localized state of the 4*f* electron. At higher temperatures $1/T_1$ is expected to decrease due to the increase in the fluctuation rate of the localized 4*f* spin. Below T_K, $1/T_1$ shows a T_1T = constant behaviour corresponding to the Fermi liquid state.

In $CeCu_2Si_2$, UBe_{13} and UPt_3, $1/T_1$ shows a localized behaviour at high temperatures and starts to show a linear dependence below T_K. Below T_c all the $1/T_1$ values decrease sharply, followed by a T^3 dependence without the coherent peak just below T_c indicating the gap zero on the line. The T^3 behaviour is also seen in other HF superconductors, URu_2Si_2,[13] UPd_2Al_3[14,15]

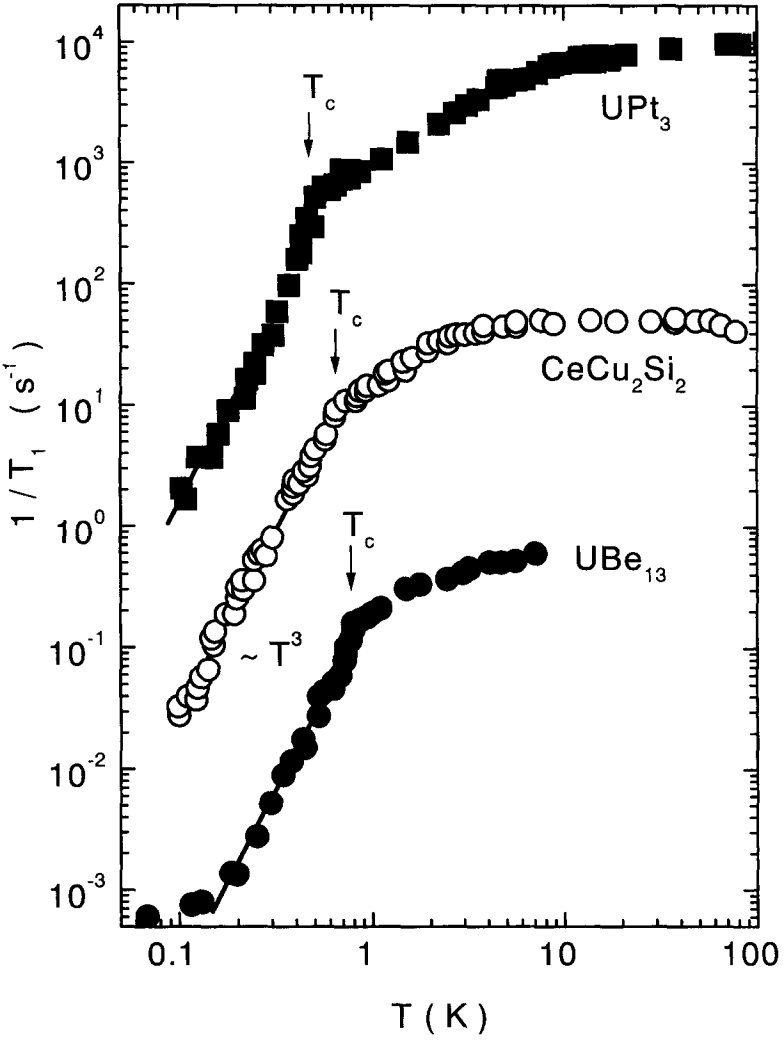

Fig. 2. A plot of $1/T_1$ for Cu in $CeCu_2Si_2$,[8] Be in UBe_{13}[9] and Pt in UPt_3.[10]

and UNi_2Al_3,[16] thus it seems that the line-node gap is common in HF superconductors.

Figure 4 shows the temperature dependence of the Knight shift in $CeCu_2Si_2$.[17] The absolute value of K decreases below T_c. The same decrease in K is also seen in UPd_2Al_3 (Fig. 5),[14] revealing that an even parity pairing (singlet) is realized in $CeCu_2Si_2$ and UPd_2Al_3. The large residual K in UPd_2Al_3 originates from large magnetic moments, as discussed later. Kohori *et al.*[18] have observed that the K value of Pt in UPt_3 does not decrease below T_c in the

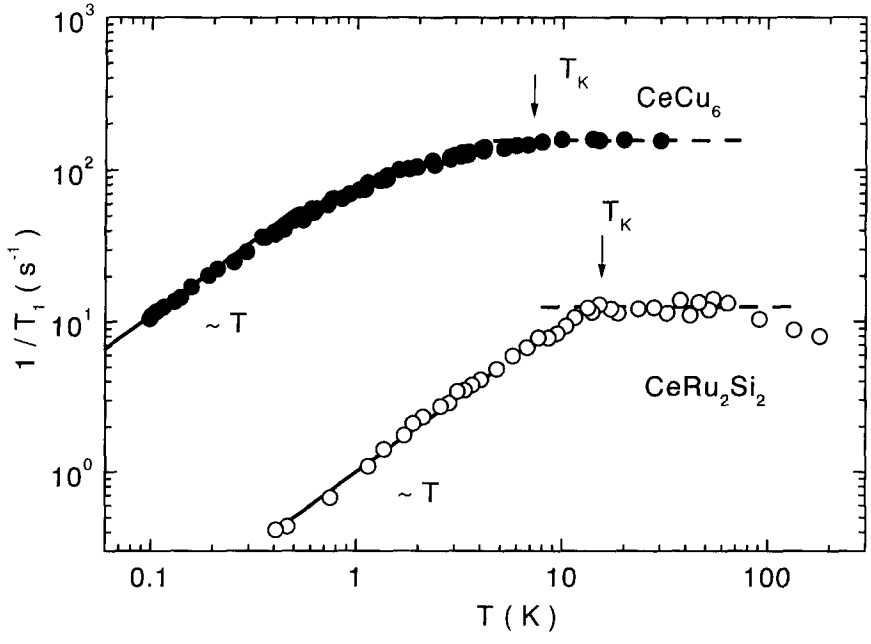

Fig. 3. A plot of $1/T_1$ for Cu in $CeCu_6$[11] and Si in $CeRu_2Si_2$.[12]

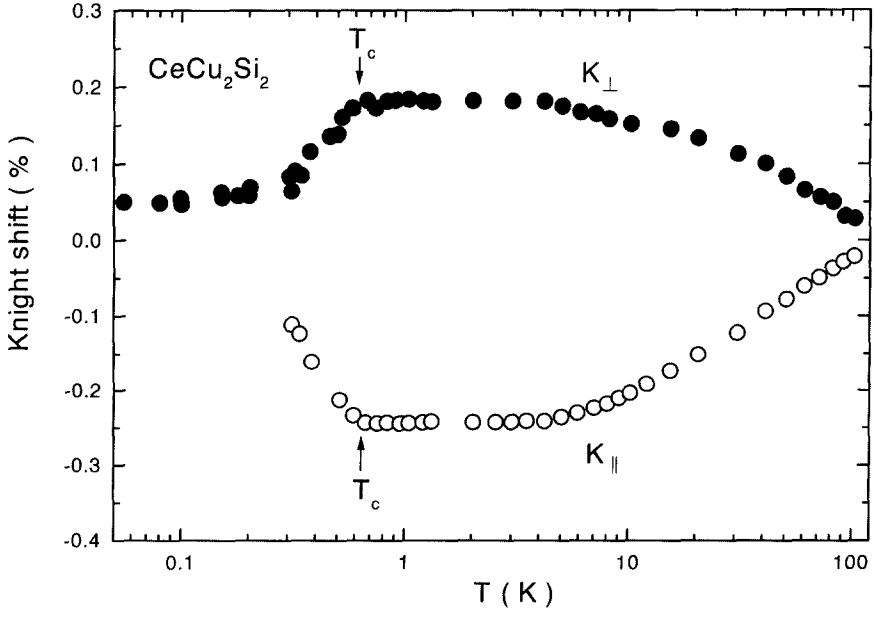

Fig. 4. Knight shift of Cu parallel and perpendicular to the c-axis, $K_\parallel$ and $K_\perp$ in $CeCu_2Si_2$.[17]

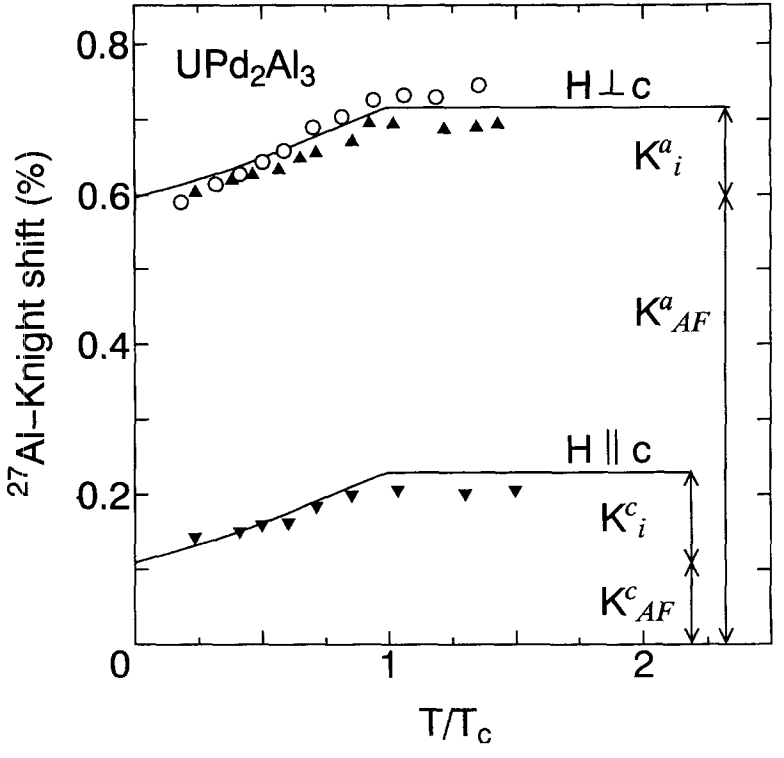

Fig. 5. Knight shift of Al in UPd_2Al_3 along the a- and c-axis. K_i and K_{AF} are the components due to conduction electrons and antiferromagnetically ordered spins, respectively.[14]

powder sample, which suggests an odd parity pairing (triplet). However, the possibility of the even parity (singlet) pairing with strong impurity or surface scattering could not be excluded completely. Tou *et al.*[19] have measured the K value of Pt in a high-quality single-crystal sample of UPt_3 and confirmed no essential change of the Knight shift below T_c in a field above 5 kOe. Along the a-axis (Fig. 6), K does not decrease even below 1.76 kOe, while it starts to decrease below 3.3 and 2.3 kOe along the b and c axes as seen in Fig. 7 (a), (b) and (c). Thus the direction of the triplet spin is concluded to be along the a-axis and the spin-orbit coupling of the Cooper pair is too weak to fix the triplet spins to the crystalline axis. This is the first observation of odd pairing superconductivity.

Since the discovery of the two-step jump in the specific heat in the superconducting transition,[20] many experiments have been carried out to establish the multiplephases A, B and C in the superconducting state in UPt_3.[21] The dashed lines in Fig. 8 show the experimental conditions used for Fig. 7(b).

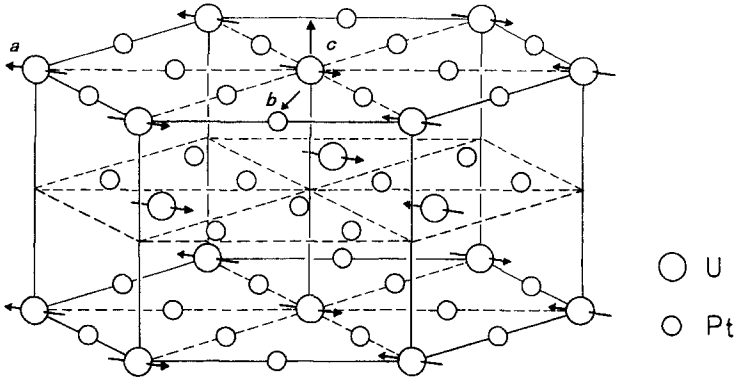

Fig. 6. Crystal structure of UPt_3.

The K value of Si in URu_2Si_2[13,22] and of Al in UNi_2Al_3[23] do not decrease below T_c although the accuracy of the K measurement is not as high as in the case of UPt_3.

Thus from the measurements of $1/T_1$ and K, the superconductivity of $CeCu_2Si_2$ and UPd_2Al_3 are concluded to be due to a d-wave, while for UPt_3

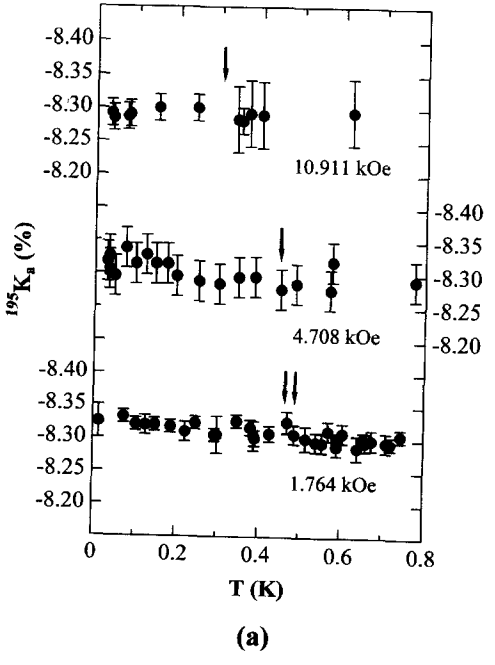

Fig. 7. *Continued.*

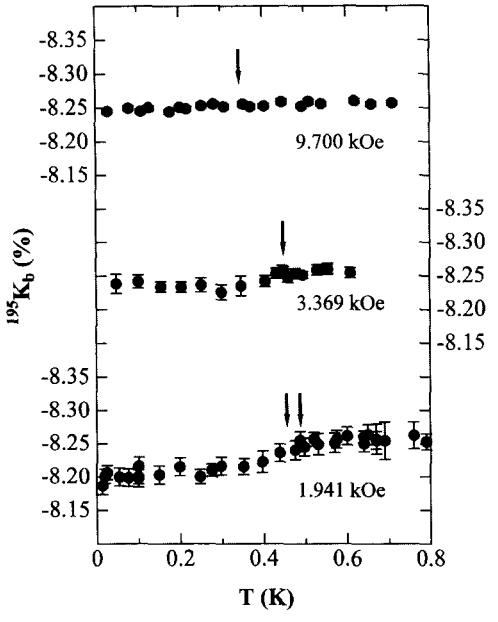

(b)

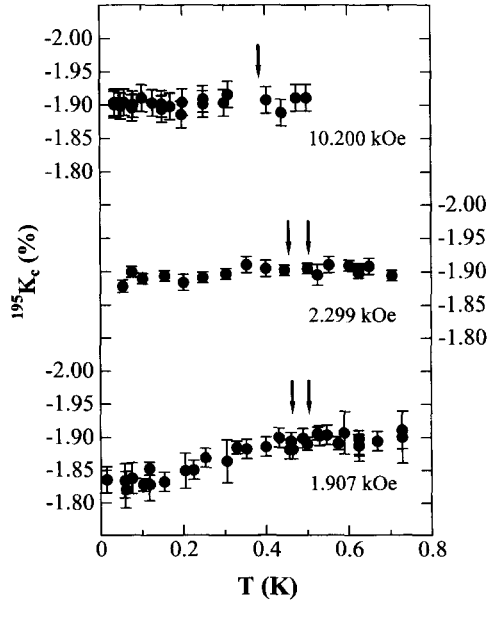

(c)

Fig. 7. (a) Knight shift of Pt in UPt_3 along a-axis. (b) and (c) Knight sl
along b- and c-axis.[19] Arrows (↓) show T_{c1} and T_{c2}.

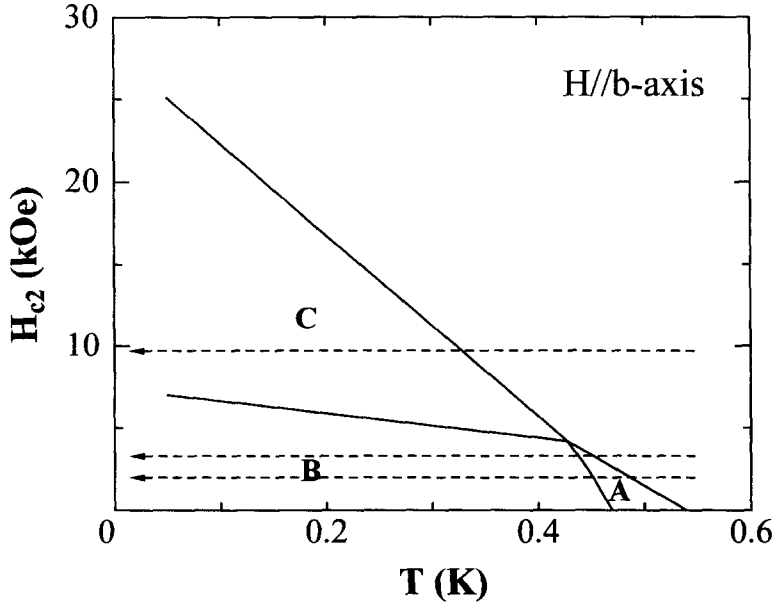

Fig. 8. Superconducting phase diagram in UPt_3 with $H//b$ axis.[21]

it is due to a p- or f-wave, URu_2Si_2, UNi_2Al_3 are probably odd parity superconductors. The symmetry of the Cooper pairs identified by the NMR experiments are listed in Table 1.

3.2. Interplay between superconductivity and magnetic order

In all HF superconductors it has been reported that the magnetic order coexists and/or competes with the superconductivity. The magnetic order seen in HF superconductors is discussed below.

As seen in Fig. 9, a plot of $1/T_1$ for Al in UPd_2Al_3 decreases below T_N corresponding to a magnetic order and then shows a T_1T = constant behaviour. This indicates that a gap appears partially on the Fermi surface associated with the magnetic order. The ungapped part of the Fermi surface is considered to be responsible for the superconductivity.

In the antiferromagnetic (AF) ordered state, a magnetic moment of 0.8 μ_B/U has been observed below 12 K by neutron diffraction measurements.[24] The large magnetic moment is the origin of the residual Knight shift at $T \rightarrow 0$ K. The temperature dependence of $1/T_1$ for Pd near T_N is different from that for Al, i.e. the distinct peak associated with the critical slowing-down of the AF spin fluctuations is observed at the Pd site,[15] whereas it is absent at the Al site. This situation is quite similar to that of Cu and O in high-T_c materials. The difference

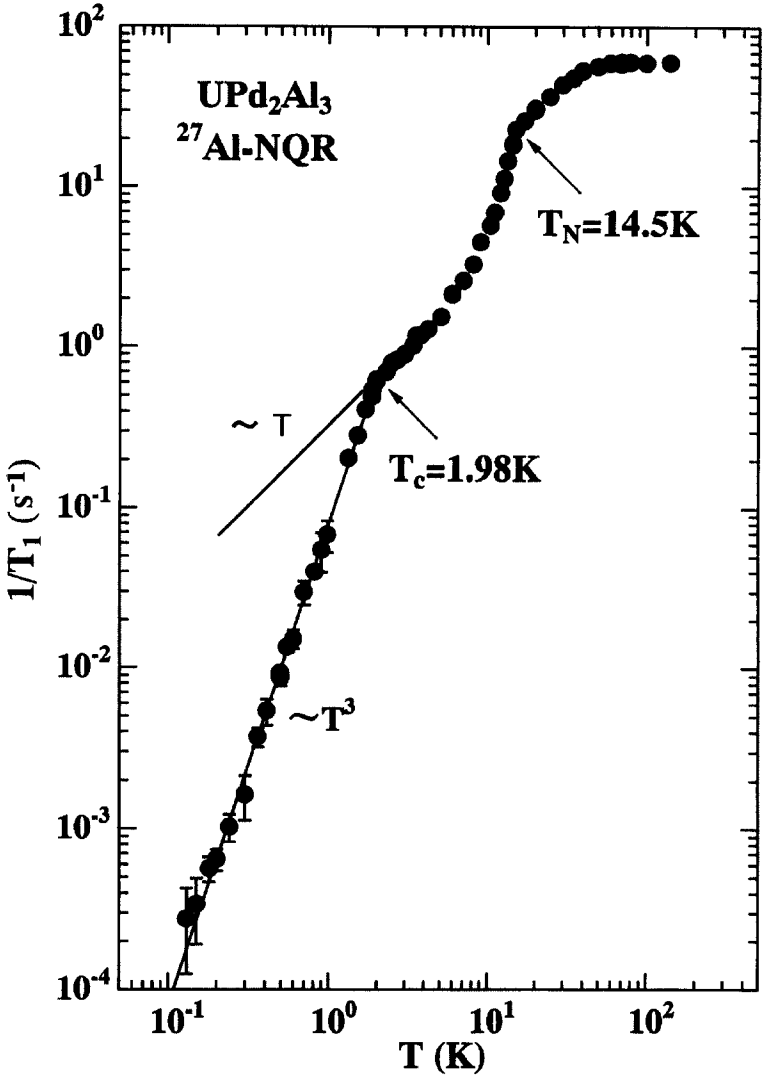

Fig. 9. A plot of $1/T_1$ for Al in UPd_2Al_3 with T_c = 1.98 K. Solid line is $1/T_1$ in the normal state in a field of 3 T.[14]

around T_N is due to the difference in the form factor (as discussed later), which is associated with the wavenumber-dependent hyperfine field. The transferred hyperfine field at the Al site from the AF spin fluctuations of the U moment is cancelled out, while it remains uncancelled at the Pd site, which gives rise to the peak in $1/T_1$ at T_N. Below T_N there appears to be no anomaly in the resonance line of Al while a splitting of the Pd NQR line associated with the $\pm 3/2 \leftrightarrow \pm 1/2$

transition appears, although no splitting appears in the $\pm 5/2 \leftrightarrow \pm 3/2$ transition as seen in Fig. 10, which indicates that the direction of the antiferromagnetically aligned moments is perpendicular to the c-axis.[15] This is consistent with the results of neutron-diffraction measurements. This splitting does not change below T_c, indicating that M_Q, or χ_Q, does not decrease below T_c.

Although, nearly the same $1/T_1$ behaviour as that of Al in UPd_2Al_3 is observed in the $1/T_1$ data of Si and Ru in URu_2Si_2, no broadening associated with an internal field has been detected in the Si NMR spectra. It was reported that a tiny magnetic moment of $\sim 0.02\mu_B$/U is observed by neutron-diffraction experiments,[25] and then it can be considered that the magnetic order observed by neutron-diffraction is not 'static' but fluctuating in time. The same 'dynamic' order may occur in UPt_3, since an antiferromagnetic correlation with a tiny moment of $\sim 0.02\mu_B$/U has been confirmed below 5 K by neutron-diffraction measurements,[26] however no anomaly has been reported from Pt NMR experiments.

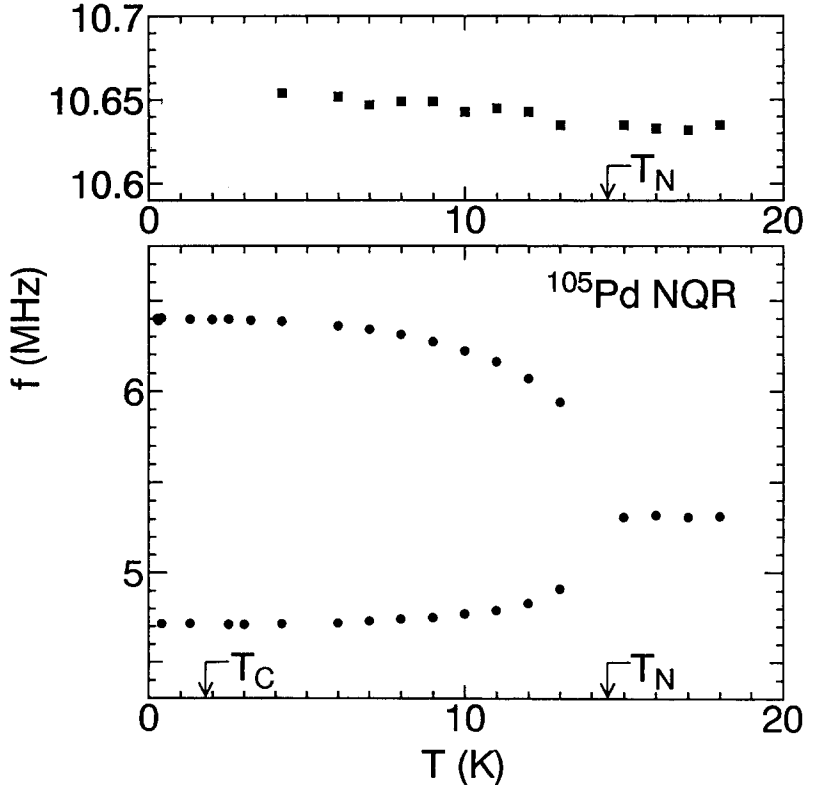

Fig. 10. NQR frequency of Pd in UPd_2Al_3. Upper and lower figures show the transitions $\pm 5/2 \leftrightarrow \pm 3/2$ and $\pm 3/2 \leftrightarrow \pm 1/2$, respectively.[15]

An intricate interplay between magnetism and superconductivity is reported in $CeCu_2Si_2$.[27-30] A magnetic anomaly was first suggested by Nakamura *et al.* from a decrease of the Cu NQR intensity far above T_c without any NQR broadening associated with an internal field upon cooling.[28] The missing phase from the NQR measurements is denoted as the *A*-phase, in which the relaxation times T_1 and T_2 are considered to be extraordinarily short, beyond the measurable limit NQR. The short relaxation times are due to low-lying spin fluctuations with frequencies comparable to the NQR frequency, $\nu_Q \sim 3.4$ MHz, which was actually observed by μSR experiments. The anomaly reported by the NQR study was confirmed by various experiments.[27] On the other hand, the phase observable by NQR shows *d*-wave superconducting behaviour below T_c, which is denoted as the superconducting *S* phase.

These recent detailed investigations, have revealed that the ground state in the compound depends strongly on sample preparation: Ce- or Cu-deficient samples show the magnetic *A*-phase, whereas Ce- or Cu-rich samples tend to show the superconducting *S*-phase. A Cu NQR study of a series of $Ce_xCu_2Si_2$ polycrystal line samples was performed to observe the evolution from the magnetic to the superconducting ground state, and to shed light on the *A*-phase properties.[30] Four samples with different Ce nominal contents were investigated: non-superconducting $Ce_{0.975}Cu_2Si_2$; $Ce_{0.99}Cu_{2.02}Si_2$ dominated by the *A*-phase at low temperature; superconducting $CeCu_{2.05}Si_2$ with $T_c \sim 0.7$ K coexisting with the *A*-phase; and *S*-phase dominant $Ce_{1.025}Cu_2Si_2$ with $T_c \sim 0.6$ K. These samples are denoted Ce0.975, Ce0.99, Ce1.00 and Ce1.025 hereafter, since their ground state does not depend on the stoichiometry of the Cu content y, but mainly on the Ce content.

The temperature dependence of $1/T_1$ for the four samples is shown in Fig. 11.[30] The $1/T_1$ plot for Ce0.975 shows a distinct peak at 0.6 K, below which the FWHM (full width at half maximum) of the Cu NQR signal increases due to the occurrence of the internal field, whereas the NQR intensity remains reduced at low temperatures, suggesting the existence of dynamic fluctuations. These results provide evidence for the onset of the static magnetic order (SMO), coexisting with the *A*-phase. From the increase in the FWHM at low temperatures, the static components of the ordered moments are estimated roughly to be $0.05\mu_B$/Ce by assuming the hyperfine coupling constant $A_{hf} \sim -4.6$ kOe/μ_B. The $1/T_1$ data for Ce1.025 show a T^3 behaviour below T_c, implying a line-node *d*-wave gap. In Ce0.99 and Ce1.00 located in the crossover region, the decrease of the NQR intensity is remarkable below T_m which is far above T_c, and is relevant to the *A*-phase development. The NQR intensity in Ce0.99 at low temperatures decreases to 5% of that above T_m without any trace of SMO, and correspondingly the $1/T_1$ value of the observable signal shows intermediate behaviour between the magnetic and superconducting states. It should be noted that the high quality of the Ce0.99 and Ce1.00 samples is ensured since the FWHM in the Cu NQR spectra, which depends on crystal homogeneity, is 14 kHz for Ce0.99 and 13 kHz for Ce1.00;

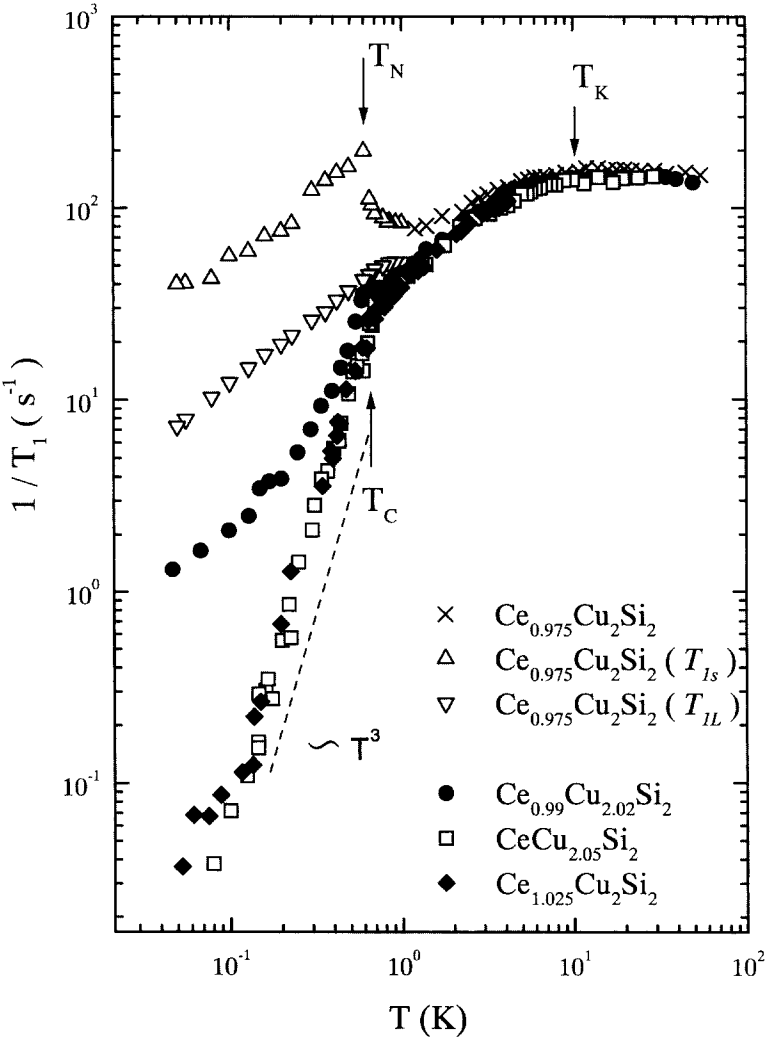

Fig. 11. Temperature dependence of $1/T_1$ for $Ce_xCu_{2+y}Si_2$. Above 1 K, T_1 in $Ce_{0.975}Cu_2Si_2$ is determined by a single component. Below 1 K, short (T_{1S}) and long (T_{1L}) components of $1/T_1$ are shown.

this is narrower than the values 35 and 26 kHz in Ce0.975 and Ce1.025, respectively. This result suggests that the magnetic fluctuations in the *A*-phase are not caused by extrinsic effects such as impurities and disorder, but are inherent to the magnetic properties seen in the compounds in the crossover region. Figure 12 shows a schematic phase diagram for the $Ce_xCu_2Si_2$ system.[30]

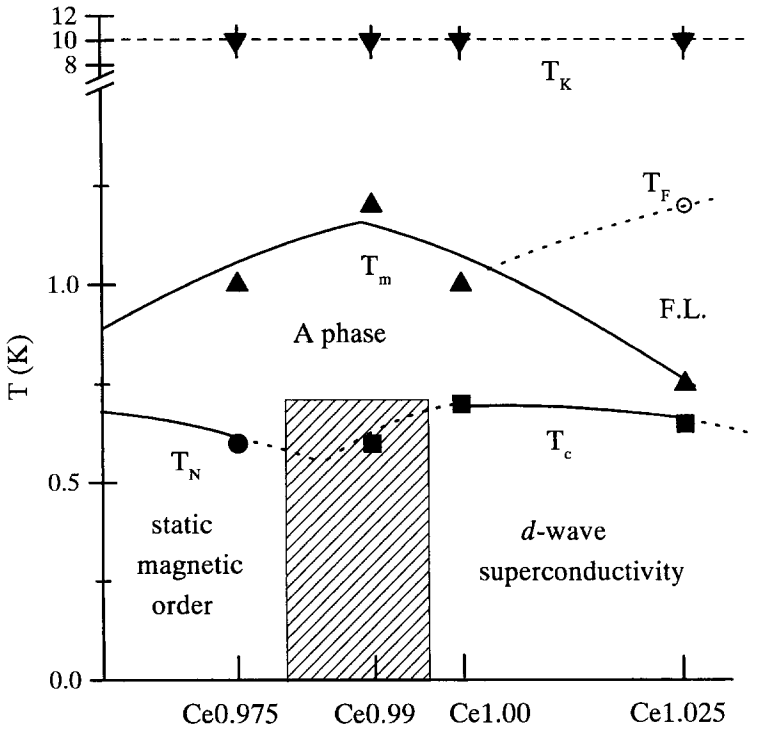

Fig. 12. Schematic phase diagram for $Ce_xCu_2Si_2$. T_K is the Kondo temperature. T_N and T_c are the magnetic and SC transition temperatures, respectively. T_m is the temperature below which $I \cdot T$ starts to decrease (I: NMR signal intensity). T_F is the temperature below which the T_1T = constant relation holds. The region denoted by slanting lines is the critical region where the static magnetic order crossover to the unconventional superconductivity occurs.

Quite recently the pressure effect on Ce0.99 has been investigated by specific-heat and Cu NQR measurements, which revealed that a tiny pressure of 5 kbar changes the A-phase into the S-phase. Furthermore, 2% Ge substitution in Ce1.00 for the Si site, which corresponds to the application of a small negative pressure, makes the Cu NQR spectrum broaden below 0.7 K, indicating the occurrence of SMO. These experimental results suggest that the A-phase state with the low-lying spin correlations may be regarded as an intermediate state between SMO and superconductivity, and that a novel relation between magnetism and superconductivity exists, which is related intimately with the origin of the superconductivity in $CeCu_2Si_2$.

From the anisotropic nature of the superconductivity (d- or p-wave) and the intimate relation between the superconductivity and magnetism, the origin of the attractive force is considered to be due to the antiferro- or ferromagnetic spin fluctuations in HF superconductors.

4. HIGH-T_c SUPERCONDUCTORS

In the following the NMR results of the Cu and O nuclei in the CuO_2 plane will be discussed, these being responsible for the superconductivity. The measurements were carried out systematically on underdoped to overdoped systems, $(La,Sr)_2CuO_4$ (LSCO),[31] $Bi_2Sr_2Ca_2Cu_3O_y$(Bi2223),[32] $Tl_2Ba_2CuO_{6+y}$(Tl2201),[33], $YBa_2Cu_3O_7$(YBCO7 or Y1237),[34] $YBa_2Cu_4O_8$ ($YBCO_8$, Y1248 or Y248),[35] $Tl_2Ba_2Ca_2Cu_3O_{10+y}$ (Tl2223),[36] $Bi_2Sr_2CaCu_2O_8$ (Bi2212),[37] $TlSr_2CaCu_2O_y$ (Tl1212),[38] $HgBa_2Ca_2Cu_3O_{8+y}$ (Hg1223),[39] $HgBa_2Ca_3Cu_4O_{10+y}$ (Hg1234),[40] and $CuBa_2Ca_3Cu_4O_{12-y}$ (Cu1234),[41] together with the effects of impurity, pressure and high field. In this section, we introduce some important NMR results which are necessary to understand the physical properties of high-T_c superconductivity.

4.1. Symmetry of the Cooper pairs and impurity effects

From the temperature dependence of $1/T_1$ for Cu in $YBCO_7$, which is similar to that in HF materials (no coherence peak and T^3-like dependence), together with the decrease in K below T_c, d-wave pairing was originally proposed by Kitaoka *et al.*[42]

Figure 13 shows a plot of $1/T_1$ of Cu, normalized by the value at T_c, against T/T_c,[32,43] in several high-T_c materials which do not show the so-called spin gap behaviour. In order to discuss the superconducting property, it is necessary to know the temperature dependence in the normal state. In these systems $1/T_1T$ is considered to follow the Curie Weiss law at high temperatures and the T_1T = constant law at low temperatures when the superconductivity is destroyed to give the normal state. Different from the HF materials, the value of H_{c2} is so high in high-T_c materials that the destruction of superconductivity by the magnetic field to give the normal state is difficult. Nevertheless the application of the T_1T = constant relation at low temperatures is concluded as discussed in detail.[3(d)]

As seen in Fig. 13, the experimental points are located on a single line below T_c. Above T_c this is not the case due to the difference in the Weiss temperatures. Below T_c, $1/T_1$ does not show the coherence peak, but decreases in proportion to T^3 except at lower temperatures. The dashed line indicates the calculation based on a two-dimensional d-wave model using the density of states in Fig. 1 with the gap parameter $\Delta(\phi) = \Delta_0 \cos 2\phi$, $2\Delta_0 = 8k_BT_c$. The agreement between the calculation and the experiment is satisfactory although there appear to be deviations at lower temperatures. The scaling of $1/T_1$ below T_c in Fig. 13 implies that the value of $2\Delta_0/k_BT_c \sim 8$ is common for these materials. Similar dependence of $1/T_1$ on temperature is also seen in ^{17}O substituted in the CuO_2 plane. Hammel *et al.* first measured $1/T_1$ of ^{17}O in $YBCO_7$ and found that the temperature dependence of $1/T_1$ for ^{17}O and Cu

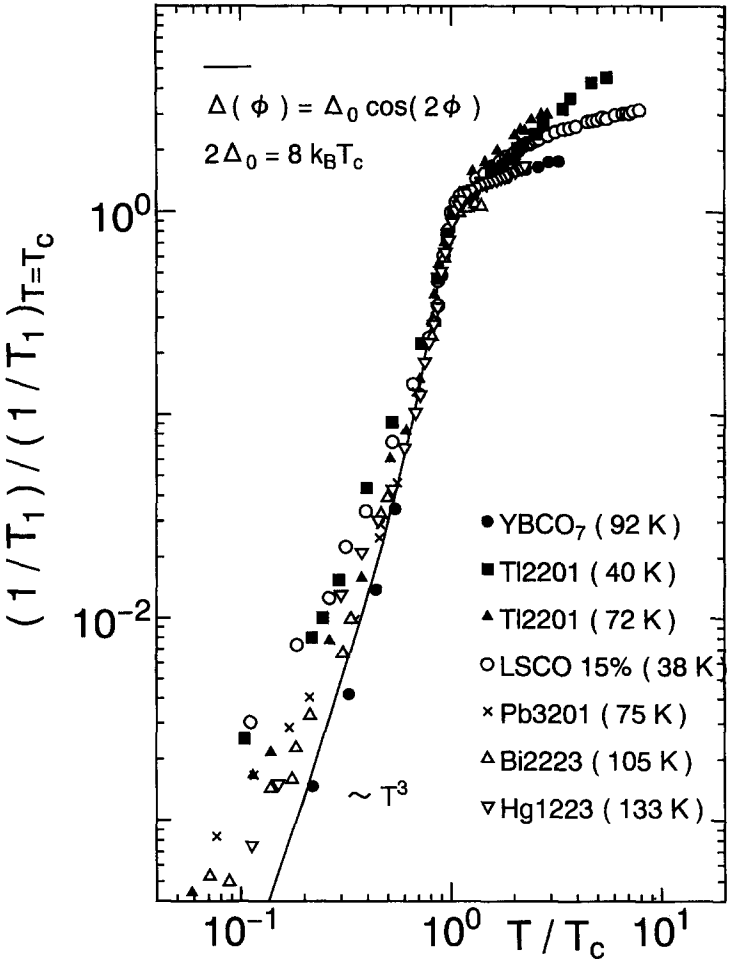

Fig. 13. A plot of $1/T_1$ for Cu in the CuO_2 plane in high T_c material, normalized by the value at T_c, against T/T_c.[43]

coincides with each other below T_c.[44] A similar result has also been obtained by Kohori *et al.*[45] The temperature dependence of $1/T_1$ for Cu and O above T_c are different from each other which is due to the difference in the form factor at the Cu and O sites as seen in Eqs (29), (30) and (31), i.e. $1/T_1$ for Cu reflects χ_Q, while $1/T_1$ for ^{17}O does not because the AF spin fluctuation is cancelled at the O site.

The Knight shift of Cu in high-T_c materials decreases below T_c indicating the singlet pairing as in Fig. 14. The temperature dependence of the Knight shift is also reproduced by the same $N_s(E)$ as in the case of $1/T_1$ as shown in Fig. 16.

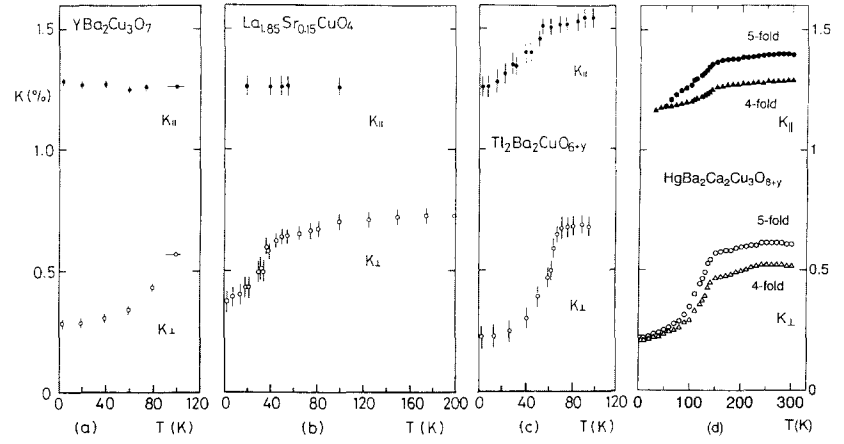

Fig. 14. Knight shift of Cu in LSCO,[46] $YBCO_7$,[47] Tl2201[33] and Hg1223.[39]

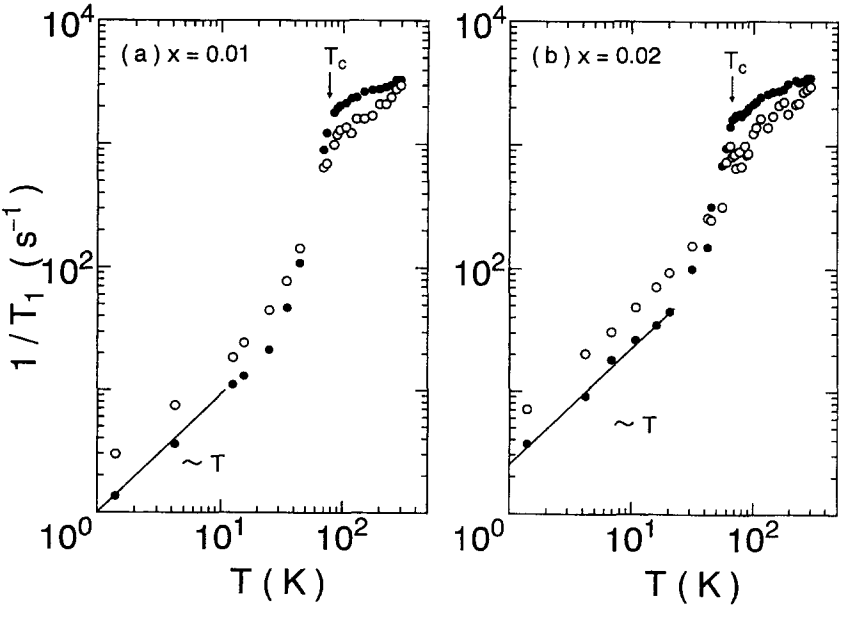

Fig. 15. A plot of $1/T_1$ for Cu in the CuO_2 plane in $YBa_2(Cu_{1-x}Zn_x)O_7$[48]. ● and ○ correspond to Cu nuclei located far from and close to Zn, respectively.

The *d*-wave model has also been supported strongly by the impurity effect. Ishida *et al.* found a linear temperature dependence of Cu on $1/T_1$ at low temperatures, when Zn is added as an impurity to $YBCO_7$, as seen in Fig. 15, and proposed a residual density of states to appear for $E \rightarrow 0$ as in the inset of

Fig. 16.[48] This residual density of states was pointed out theoretically to appear in the unitarity limit scattering by non-magnetic impurities in p- or d-wave superconductors in a heavy fermion study.[49] From this result it became possible to explain the BCS-like temperature dependence of the penetration depth, λ,[50] which supported strongly the s-wave pairing model in high-T_c superconductors at an early stage, in terms of the d-wave + impurity model.[51-53]

In addition to $1/T_1$ they found that the Knight shift also has a residual part with Zn doping as in Fig. 16. It should be noted that the temperature dependence of K, which is linear at low temperatures for $x = 0$, changes seemingly to that of the BCS s-wave case. (λ and K have the same temperature dependence below T_c.)

In $YBCO_7$ with Zn, the $1/T_1$ values are not unique at low temperatures but have a distribution. However, each component of $1/T_1$ follows the T_1T = constant law. The part having larger values of $1/T_1T$ corresponds to nuclei close to Zn, while the smaller values correspond to those far from Zn. The

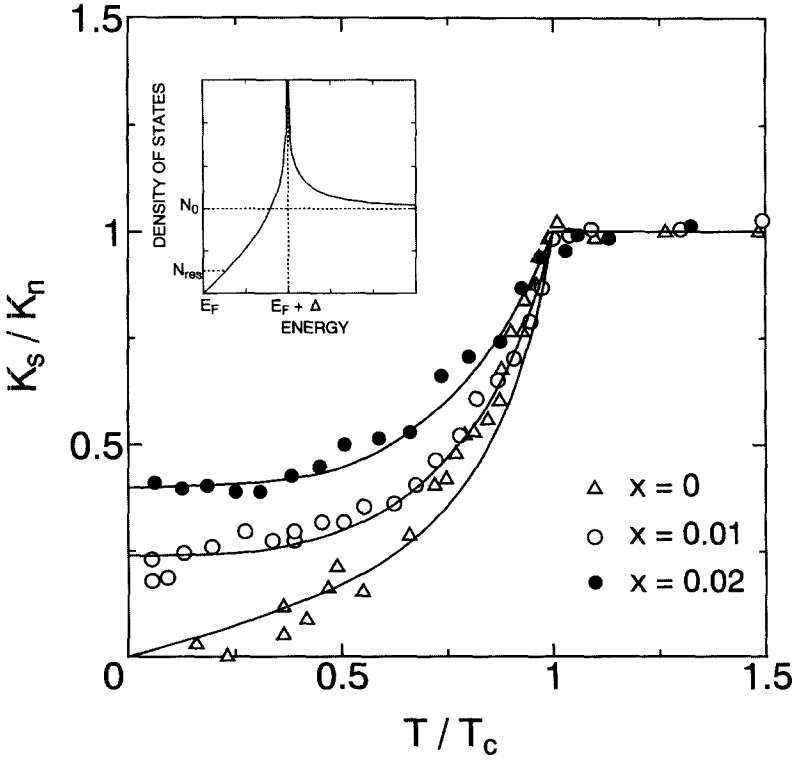

Fig. 16. Knight shift of Cu in the CuO_2 plane in $YBa_2(Cu_{1-x}Zn_x)O_7$.[48] Inset shows the density of states in the 2-D d-wave model with the pair-breaking effect due to impurity scattering in the unitarity limit.

linear behaviour in $1/T_1$ at low temperatures is more obvious in some high-T_c materials than others. Figure 17 shows similar plots to those in Fig. 13 in the case where the effect of the impurities and imperfections are appreciable in several compounds. The symbols F and N in Fig. 17 denote nuclei far from and near to the Zn impurity in the $YBCO_7 + Zn$ system, respectively.

The distribution of the residual density of states has theoretically been calculated by Onishi *et al.*[54] In Fig. 17 the behaviour of the T_1T = constant plot for Bi2212[37] and Tl2223[36] are attributed to crystal imperfections. Non-annealed as-grown Tl2223 has a T_c of 115 K where the linear part in $1/T_1$ is

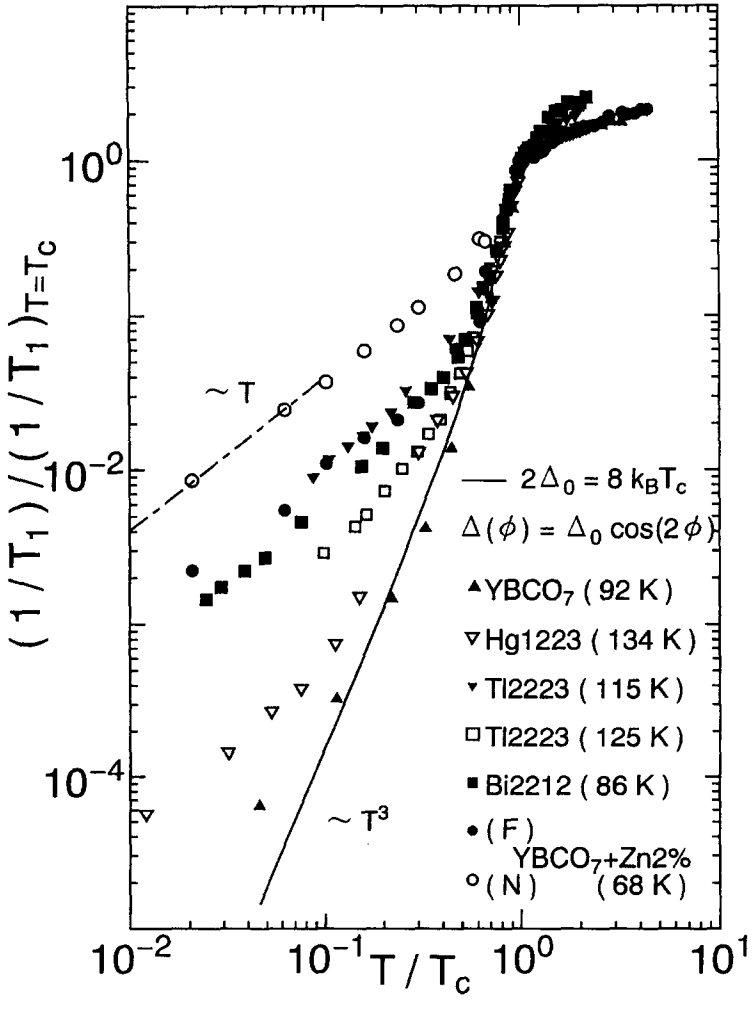

Fig. 17. A plot of $1/T_1$ for Cu in the CuO_2 plane, normalized by the value at T_c, against T/T_c in high T_c materials with impurity or imperfection.

larger, while T_c goes up to 125 K by annealing, together with a decrease in the linear part as shown in Fig. 17. Annealing for the suppression of crystal imperfections causes pair breaking to decrease with an increase in T_c.

Figure 18 shows the relations between T_c and the residual density of states N_{res}[55] that are obtained from the expressions,

$$\left(\frac{N_{res}}{N_0}\right)^2 = \frac{(T_1T)_{T_c}}{(T_1T)_{T\to 0}} \tag{9}$$

and

$$\frac{N_{res}}{N_0} = \frac{K_s(T\to 0)}{K_s(T_c)} \tag{10}$$

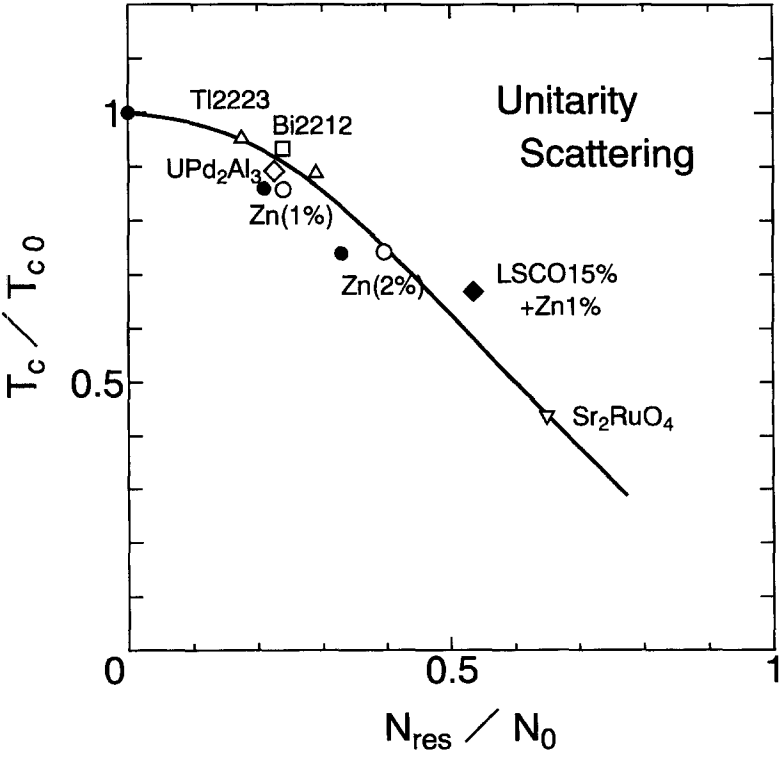

Fig. 18. T_c plotted against the residual density of states obtained from $1/T_1$(●) and K(○) in $YBa_2(Cu_{1-x}Zn_x)O_7$, from $1/T_1$ in Tl2223, Bi2212, UPd_2Al_3, $La_{1.85}Sr_{0.15}CuO_4$ + Zn1% and Sr_2RuO_4.

Here N_0 is the density of states in the normal state. $1/T_1$ is distributed so that the average of the distributed values is plotted. The N_{res} values obtained both from K and $1/T_1$ agree fairly closely with each other. In the figure the solid line is the theoretical curve produced by Hotta.[56] The agreement between the observed and theoretical values is good.

Now, K_s is proportional to the uniform susceptibility χ_0, while $1/T_1$ is governed mainly by the staggered susceptibility χ_Q enhanced largely by the antiferromagnetic spin fluctuations as follows

$$\chi_Q = \frac{\chi_Q^0}{1 - I\chi_Q^0} \tag{11}$$

Here I is the electron–electron interaction energy, χ_Q^0 the staggered susceptibility when $I = 0$. For an s-wave, χ_Q^0 decreases with decreasing temperature so that the enhancement factor for $1/T_1$ ($\alpha(T)$ in Eq. (1)) decreases, while χ_Q^0 is not suppressed for a d-wave as pointed out by Moriya *et al.*[57] and Bulut and Scalapino,[58] providing no appreciable change occurs in $\alpha(T)$, because $q \sim (\pi, \pi)$ connects two gapless regions of the Fermi surface. This assures the relations (9) and (10) and is the reason why the N_{res}/N_0 values obtained from K and $1/T_1$ agree with each other.

The value of $1/T_1$ for Cu is governed by χ_Q^0 while at the ^{17}O site the effect of χ_Q^0 is filtered by a form factor, nevertheless both of the T_1 values of Cu and O have approximately the same temperature dependence below T_c. Furthermore the K_s and $1/T_1$ values of Cu are consistent with a calculation using the same gap parameter $2\Delta/k_B T_c \sim 8$. These facts are consistently explained when χ_Q^0 does not decrease below T_c and support the d-wave pairing model implicitly.

Bulut and Scalapino[58] calculated the Gaussian spin echo decay rate, $1/T_{2G}$ which is proportional to χ_Q^0 in the s and d-wave model and proposed the measurement of $1/T_{2G}$ to distinguish between the d- or s-wave. The experiment by Itoh *et al.*[59] coincided well with the calculation on the d-wave model.

4.2. Hole distribution

4.2.1. Hole distribution in high-T_c cuprates

Zheng *et al.*[60] have obtained the hole numbers at the Cu and O sites separately in the CuO_2 planes in various high-T_c materials. They followed the analyses proposed by Hanzawa *et al.*[61] and Ohta *et al.*[62] from the NQR frequencies of Cu and ^{17}O, neglecting the contributions from outside of the positions of the atoms concerned.

The NQR frequency for Cu is composed of

$$^{63}\nu_Q = {}^{63}\nu_{3d} + {}^{63}\nu_{4p} \tag{12}$$

where $^{63}\nu_{3d}$ arises from Cu-3d holes and $^{63}\nu_{4p}$ is due to the 4p electrons the amount being 0.1. $^{63}\nu_{4p}$ is estimated to be -69 MHz which is assumed to be constant for the materials studied. The hole numbers in the $|x^2-y^2>$ and $|3z^2-r^2>$ orbitals are given as

$$n_{x^2-y^2}=\frac{1}{2}\left(\sqrt{1+\frac{\eta^2}{3}}+1\right)\frac{^{63}\nu_{z3d}}{^{63}\nu_Q^0} \tag{13}$$

$$n_{3z^2-r^2}=\frac{1}{2}\left(\sqrt{1+\frac{\eta^2}{3}}-1\right)\frac{^{63}\nu_{z3d}}{^{63}\nu_Q^0} \tag{14}$$

here

$$\nu_\alpha=\frac{3eQ}{2I(I-1)}\frac{\partial^2 V}{\partial\alpha^2} \tag{15}$$

$$\nu_Q=\nu_z\left(1+\frac{\eta^2}{3}\right)^{1/2} \tag{16}$$

where η is the asymmetry parameter of the electric field gradient at the site of the nucleus concerned, and $^{63}\nu_Q^0$ is the NQR frequency due to one Cu d-hole and is described as

$$^{63}\nu_Q^0=\frac{1}{2}\frac{^{63}Q}{h}\frac{e^2}{4\pi\varepsilon^2}\frac{4}{7}\langle r^{-1}\rangle_{3d}=117.1\ \text{MHz} \tag{17}$$

For Cu in the CuO_2 plane, $\eta\simeq 0$ so that

$$n_{x^2-y^2}=\frac{^{63}\nu_{z3d}}{^{63}\nu_Q^0} \tag{18}$$

For the oxygen site, since η is finite, holes should reside on more than one p-orbital. For the hole number n_α in the orbital in the α direction ($\alpha=x,y,z$), we have

$$^{17}\nu_a=\ ^{17}\nu_Q^0\left(n_x-\frac{n_y+n_z}{2},\ n_y-\frac{n_x+n_z}{2},\ n_z-\frac{n_x+n_y}{2}\right) \tag{19}$$

with

$$^{17}\nu_Q^0 = \frac{3}{24}\frac{^{17}Q}{h}\frac{e^2}{4\pi\varepsilon_0}\frac{4}{5}\langle r^{-3}\rangle_{2p}$$

$$= 3.646 \text{ MHz}$$

$$\eta = \frac{(3/2)n_{p\pi}}{n_{p\sigma} - (1/2)n_{p\pi}} \tag{20}$$

$$\eta_{p\sigma} = \left(1 + \frac{\eta}{3}\right)\frac{^{17}\nu_z}{^{17}\nu_Q^0} \tag{21}$$

$$\eta_{p\pi} = \frac{2}{3}\eta\frac{^{17}\nu_z}{^{17}\nu_Q^0} \tag{22}$$

The hole numbers thus obtained are shown in Table 2.[60] The plausibility of these results is confirmed by the Van Vleck susceptibility which is given by

$$\chi_{VV} = \frac{8\mu_B^2}{E_{xy} - E_{x^2-y^2}} n_{x^2-y^2} \tag{23}$$

along the c-axis. If we assume that the energy difference between the ground state and the excited state, $E_{d_{xy}} - E_{d_{x^2-y^2}}$, does not depend on the materials, χ_{VV} should be proportional to $n_{d_{x^2-y^2}}$.

$K_{orb} \propto \chi_{VV}$ is plotted against the hole numbers at the Cu site in Fig. 19.[60] The points are approximately on a straight line intercepting the origin, which is consistent with the relation given by Eq. (23).

The hole numbers govern several physical quantities such as T_c, the antiferromagnetic spin-fluctuations strength in high-T_c materials. Figure 20 shows T_c plotted against $n_{x^2-y^2} + 2n_{p\sigma}$ and $n_{p\sigma}/n_{x^2-y^2}$. There are optimum values in $n_{x^2-y^2}$ and $n_{p\sigma}$ which give a maximum value for T_c, when $n_{x^2-y^2} + 2n_{p\sigma} \sim 1.4$, $n_{x^2-y^2}/2n_{p\sigma} \sim 1$. The $\chi_Q\Gamma_Q$ values are considered to be largest around these hole numbers.[60]

4.2.2. Hole redistribution under pressure

NQR/NMR measurements have been carried out in an attempt to reveal the hole distribution under pressure and its relevance to the change of T_c.[63,64] In $YBa_2Cu_4O_8$,[63] it was found that ν_Q(Cu) decreases in the CuO chain but increases in the CuO_2 plane (Fig. 21), which indicates that the number of holes decreases at the chain site but increases at the plane site. A similar result was

Table 2. $^{63}\nu_Q = {}^{63}\nu_z(1 + ({}^{63}\eta^2/3))^{1/2}$ for various high-T_c materials. Value in parentheses for $YBa_2Cu_3O_7$ is that for O(3). For $Tl_2Ba_2Ca_2Cu_3O_{10}$, the data correspond to the pyramidal CuO_2 plane. 4-(5-) fold in $HgBa_2Ca_2Cu_3O_{8+y}$ and $HgBa_2Ca_3Cu_4O_{10+y}$ denotes the Cu site coordinated by 4-(5-) fold oxygens

Material		T_c(K)	$^{63}\nu_Q$ (MHz)	$^{17}\nu_Z$ (MHz)	$^{17}\eta$	$n_x^2 - \frac{2}{y}$	$n_{p\sigma}$	$n_{p\pi}$
$La_{1.925}Sr_{0.075}CuO_4$		22	34.2	0.60	0.40	0.848	0.19	0.05
$La_{1.85}Sr_{0.15}CuO_4$		38	35.8	0.69	0.36	0.862	0.21	0.05
$La_{1.76}Sr_{0.24}CuO_4$		18	37.4	0.81	0.31	0.875	0.25	0.05
$YBa_2Cu_3O_{6.6}$		60	28.9	0.889	0.224	0.837	0.262	0.036
$YBa_2Cu_4O_8$		80	29.8	0.90	0.23	0.844	0.27	0.04
$YBa_2Cu_3O_7$		92	31.5	0.986	0.237	0.859	0.292	0.043
				(0.966)	(0.214)			(0.038)
$Tl_2Ba_2Ca_2Cu_3O_{10}$		115	17.4	1.12	0.37	0.738	0.34	0.08
$Bi_2Sr_2CaCu_2O_8$		86	19	1.14	0.36	0.75	0.35	0.08
$TlSr_2CaCu_2O_7$		64	21.9	—	—	0.777	—	—
$Tl_2Ba_2CuO_6$		80	21.5	1.154	0.36	0.77	0.354	0.076
$Tl_2Ba_2CuO_6$		10	26.9	1.22	0.34	0.82	0.37	0.08
$HgBa_2Ca_2Cu_3O_{8+y}$	(4-fold)	133	10.2			0.68		
	(5-fold)	133	16.1			0.73		
$HgBa_2Ca_3Cu_4O_{10+y}$	(4-fold)	123	9.68			0.67		
	(5-fold)	123	17.8			0.74		

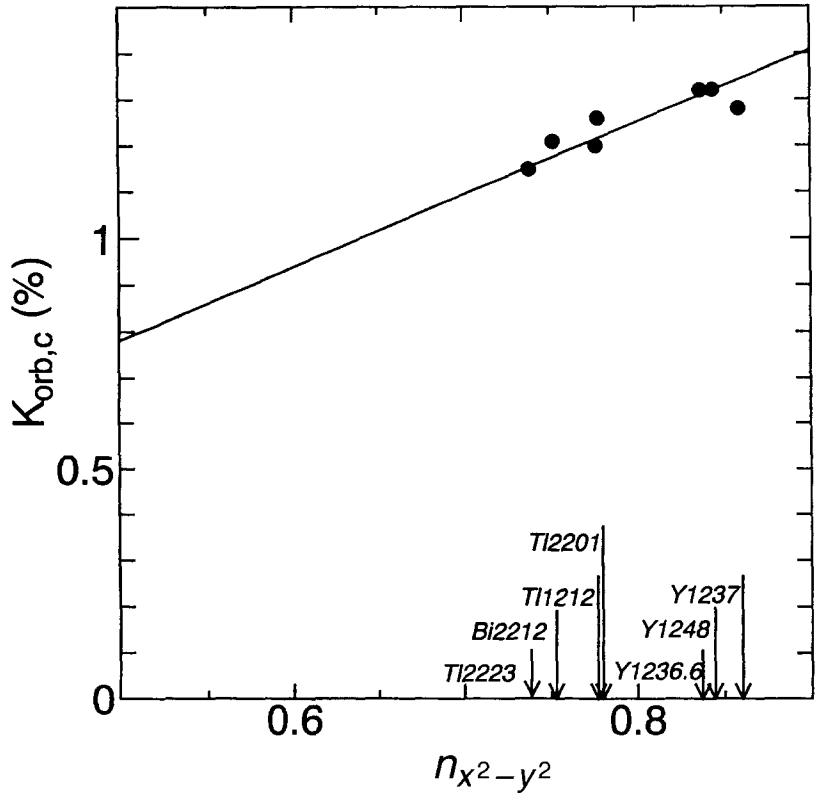

Fig. 19. $K_{orb,c}$ plotted against hole number at the Cu site.[60]

also obtained by Zimmermann *et al.*[65] This is consistent with the Madelung potential calculation which suggests that such a hole redistribution is favoured since the bonding between the apex oxygen and the plane is much shortened compared to the overall compression of the lattice.[66] The Knight shift measurement supports such a change of hole density in the planar Cu site.[64] As seen in Fig. 22, the shift decreases under pressure, suggesting that the spin susceptibility is increased since the hyperfine coupling constant is negative. However, $1/T_1$ does not change, within experimental uncertainty, under a pressure of 13 kbar (Fig. 23). This may be due to the fact that the hole removed from the chain also enters the planar oxygen site. Thus, a pressure effect is suggested, as shown by the arrow in Fig. 20(b). In $La_{1.85}Sr_{0.15}CuO_4$, ν_Q(Cu) was found to decrease with pressure,[63] indicating a decrease of the hole at the Cu site (Fig. 24). It is believed that the total hole number does not change under pressure since there is no chain site in this compound. It is then suggested that the hole is removed from the Cu site and put onto the oxygen site,

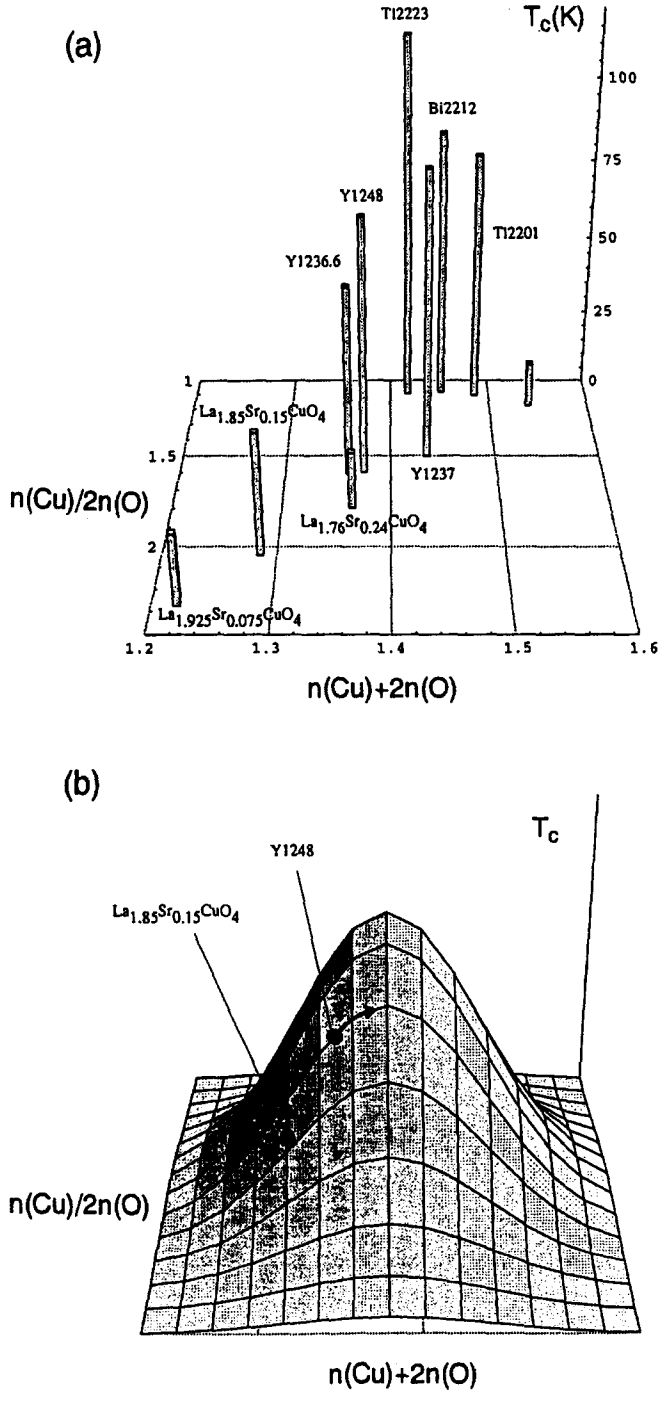

Fig. 20. (a)T_c plotted against $n(\mathrm{Cu}) + 2n(\mathrm{O})$ and $n(\mathrm{Cu})/2n(\mathrm{O})$.[60] (b) Schematic dependence of T_c on $n(\mathrm{Cu}) + 2n(\mathrm{O})$ and $n(\mathrm{Cu})/2n(\mathrm{O})$. The arrow indicates the change produced by applying pressure.

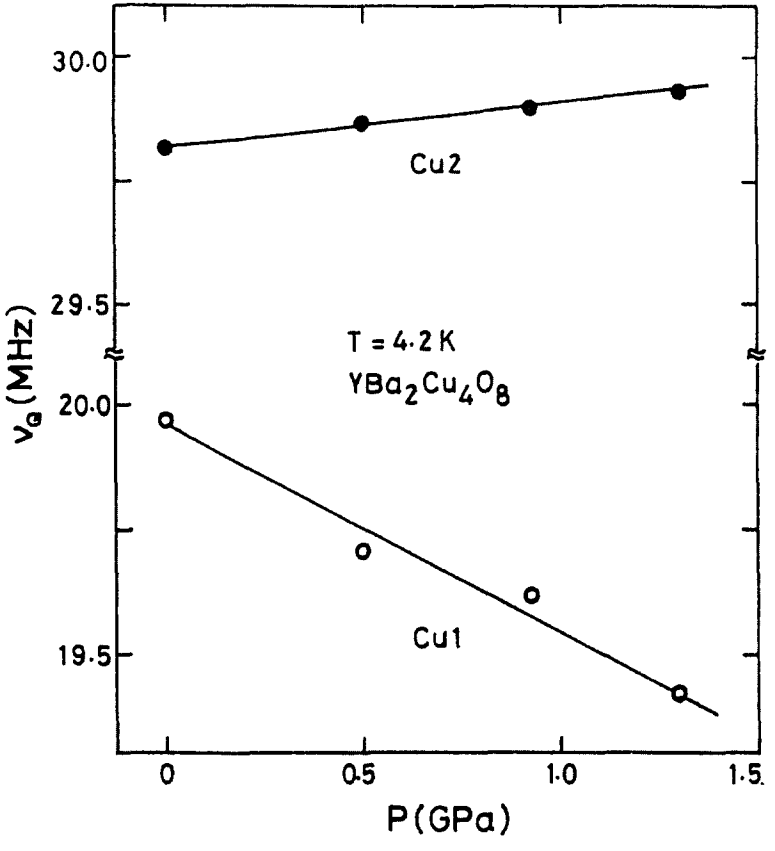

Fig. 21. Pressure dependence of ν_Q at Cu sites in $YBa_2Cu_4O_8$.[63]

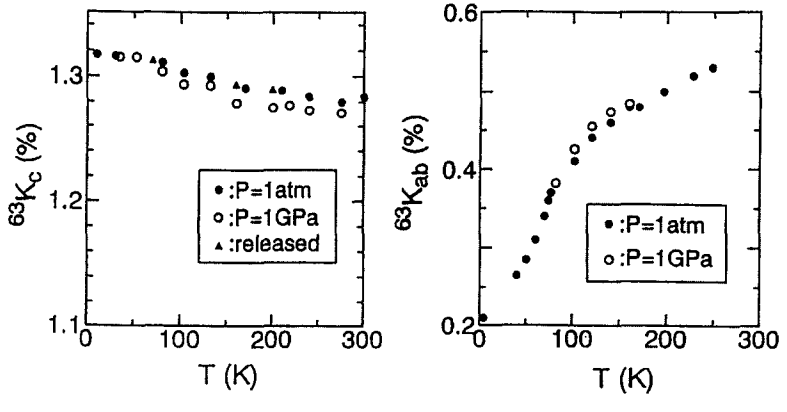

Fig. 22. Knight shift of $YBa_2Cu_4O_8$ at ambient and high pressures.[64]

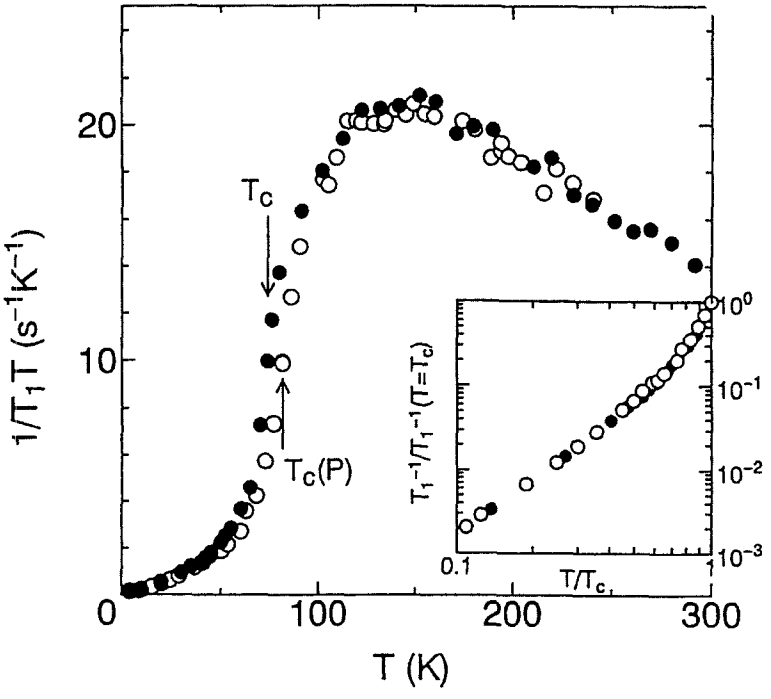

Fig. 23. A plot of $1/T_1T$ for $YBa_2Cu_4O_8$ at ambient (closed circles) and high pressures (open circles). Inset shows $1/T_1$ normalized to its value at T_c.[64]

as depicted by the arrow in Fig. 20(b). That is, hole redistribution occurs in the CuO_2 plane. $1/T_1$ measurements (Fig. 25), which show a decrease under pressure, support such a suggestion.[64]

4.3. Superconductivity mechanism

The *d*-wave pairing in high-T_c superconductors suggests that the mechanism for superconductivity is magnetic in origin. In the following some direct evidence for the mechanism to be magnetic is introduced. Tokunaga *et al.*[67] measured the $1/T_1$ value of Cu in $YBa_2(Cu_{1-x}Ni_x)_3O_7$ and found that $1/T_1$ increases with x, but falls on a single curve when plotted against T/T_c, as shown in Fig. 26(a) and (b), at temperatures above T_c. For $x = 0.03$ the scaling holds even below T_c. At temperatures above T_c, T_1 is uniquely determined, while at temperatures below T_c, T_1 values are distributed and show upturns at low temperatures. Ni has a localized moment of $S = 1/2$ according to susceptibility measurements.[68] The behaviour at low temperatures with large x is attributed to the direct effect of localized Ni spins which start to order at

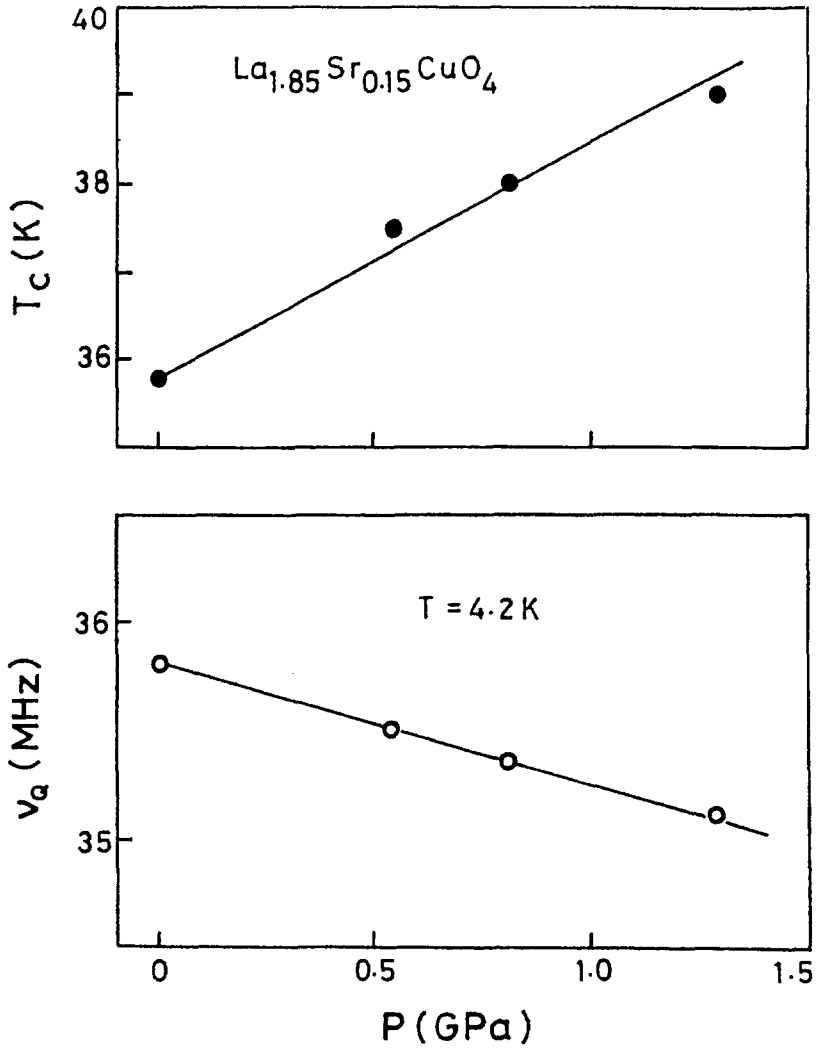

Fig. 24. Pressure dependence of T_c and ν_Q at Cu sites in $La_{1.85}Sr_{0.15}CuO_4$.[63]

low temperatures. However, the increase in $1/T_1$ above T_c is not due to a direct effect from the localized spins.[67]

It is well known that the $1/T_1$ value of Cu in high-T_c materials is governed by the antiferromagnetic spin fluctuation (AFSF) of Cu. Therefore, the increase in $1/T_1$ with x is concluded to be due to the change of AFSF with x. The fact that $1/T_1$ is scaled by T/T_c indicates an intimate correlation between T_c and AFSF.

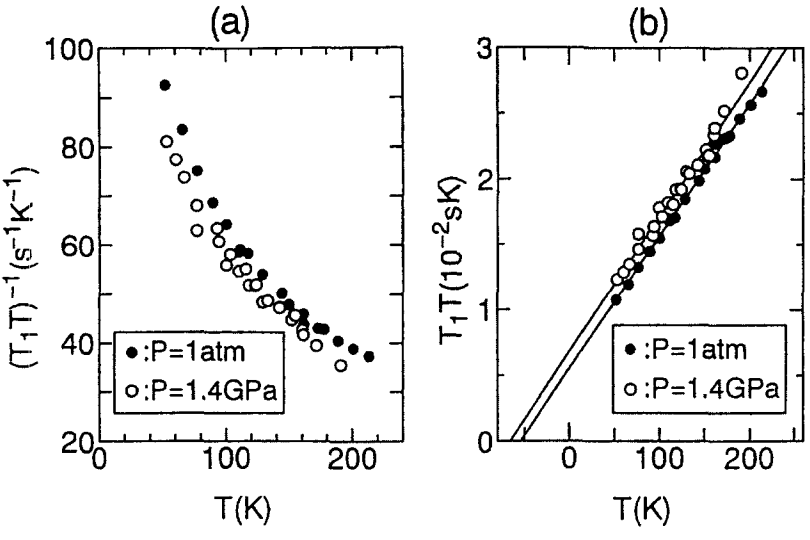

Fig. 25. A plot of $1/T_1T$ for $La_{1.85}Sr_{0.15}CuO_4$ at ambient and high pressures.[64]

$1/T_1$ is, in general, expressed as

$$\frac{1}{T_1T} \propto \sum_q A_q^2 \frac{\chi_\perp''(q, \omega, T)}{\omega} \tag{24}$$

which leads to

$$\frac{1}{T_1(x)t} \propto \sum_q A_q^2 \frac{\chi_\perp''(q, \omega, t, x)}{\omega} T_c(x) \tag{25}$$

with $t \equiv T/T_c$. Experiment shows that the left-hand side of Eq. 25 is constant with x, if we fix t, so that

$$T_c(x) \propto \left[\sum_q A_q^2 \frac{\chi_\perp''(q, \omega, t, x)}{\omega} \right]^{-1} \tag{26}$$

A_q is a constant except for the Cu close to Ni. The relation (26) is direct evidence for the attractive force being due to spin fluctuation, irrespective of any theoretical model. In the conventional superconductor, the isotope effect provides direct evidence for phonon-mediated superconductivity. The relation (26) is considered to correspond to the isotope effect in a phonon-mediated superconductivity model.

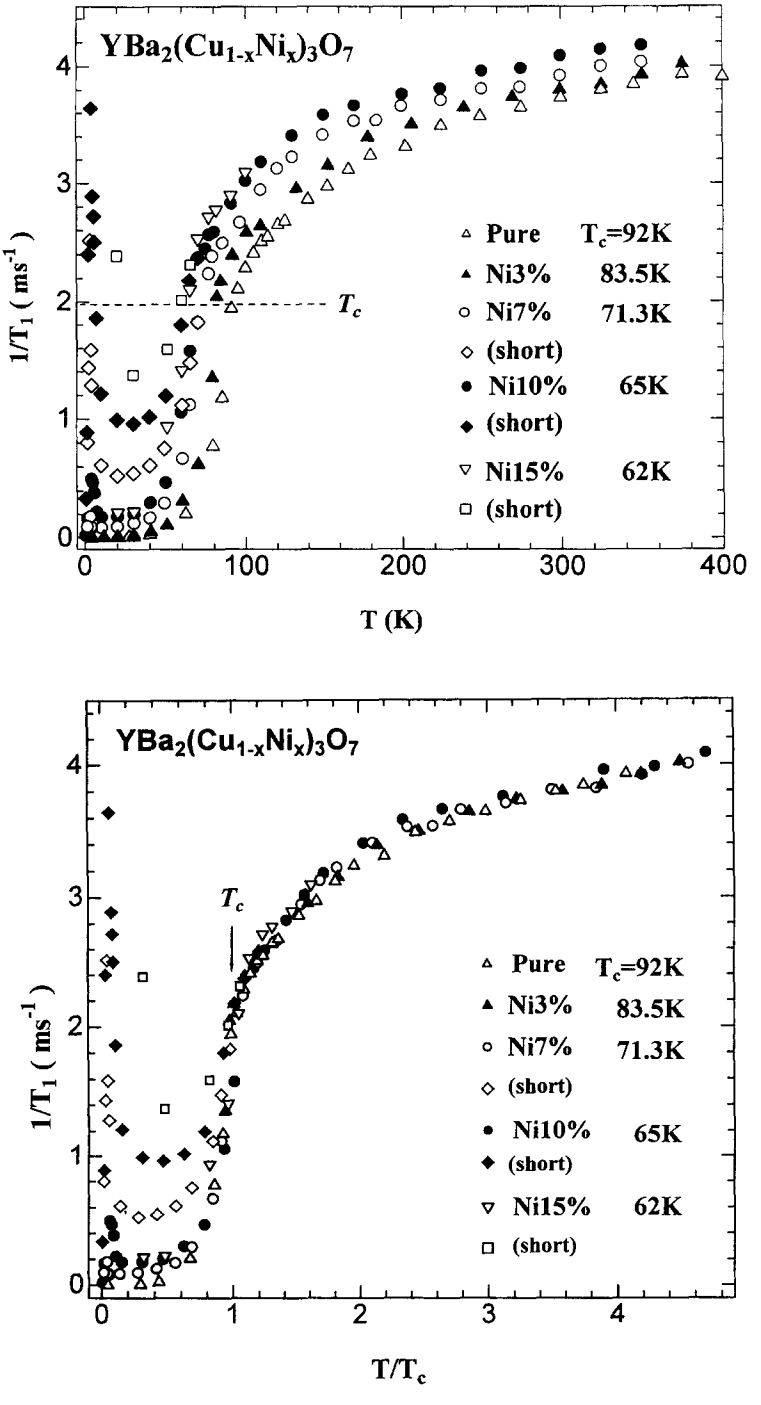

Fig. 26. A plot of $1/T_1$ for Cu in the CuO_2 plane in $YBa_2(Cu_{1-x}Ni_x)_3O_7$ against T (a) and T/T_c (b).[67]

According to Mila and Rice,[69] the $1/T_1$ value for Cu for the quantization axis c and the a, b axes are respectively,

$$\left(\frac{1}{T_1T}\right)_c \propto \sum_q F_{a,b}(q)^2 \frac{\chi''_\perp(q,\omega_n)}{\omega_n} \tag{27}$$

$$\left(\frac{1}{T_1T}\right)_{a,b} \propto \frac{1}{2}\sum_q [F_{a,b}(q)^2 + F_c(q)^2] \frac{\chi''_\perp(q,\omega_n)}{\omega_n} \tag{28}$$

$$F_{a,b}(q) = A_{a,b} + 2B[\cos q_x a + \cos q_y a] \tag{29}$$

$$F_c(q) = A_c + 2B[\cos q_x a + \cos q_y a] \tag{30}$$

$1/T_1$ of ^{17}O is given by

$$\frac{1}{T_1T} \propto \sum_q F(q) \frac{\chi''_\perp(q,\omega_n)}{\omega_n} \qquad \text{with} \qquad F(q) = 2C \cos q_x a/2 \tag{31}$$

Here $A_{a,b}$, A_c are the on-site hyperfine field, and B and C are the transferred hyperfine field from the neighbouring Cu spin. When $\chi(q,\omega)$ has a sharp peak at $q = Q$ and Lorentzian-type energy dependence, $\chi(q,\omega)$ is expressed as

$$\chi(q,\omega) = \frac{\chi_Q}{1 + (q-Q)^2\xi^2 - i\hbar\omega/\Gamma_Q} \tag{32}$$

where χ_Q, ξ, and Γ_Q are the staggered susceptibility, magnetic coherence length and the energy of the antiferromagnetic spin fluctuations, respectively. By summing in the two-dimensional q space, Eq. (27) is reduced to

$$\frac{(1/T_1T)_c}{(A_{a,b} - 4B)^2} \propto \frac{\chi_Q}{\Gamma_Q\xi^2} \tag{33}$$

In $YBCO_{6-7}$, $A_{a,b}$, A_c and B are estimated to be 37 kOe, -158 kOe and 39 kOe, respectively from $A_{a,b} + 4B$, $A_c + 4B$ and $A_{a,b} - 4B$ which are obtained by the K–χ plot along the c and ab axes[70] and the internal field in the AF ordering state.[71]

With increasing Ni content x, A_i ($i = c$ and a, b) and B are not changed except for Cu atoms close to Ni and the ratio χ_Q/ξ^2 is considered to be constant.

Then Eq. (25) leads to

$$\frac{1}{T_1(x,t)t} \propto \frac{1}{\Gamma_Q(x,t)} T_c(x) \tag{34}$$

The left-hand side of Eq. (34) is constant when t is fixed which gives $T_c(x) \propto \Gamma_Q(x, t)$. This means that $\Gamma_Q(x, t)$ at each value of t is proportional to $T_c(x)$. Thus the decrease in T_c upon Ni substitution in $YBCO_7$ is attributed to the decrease in $\Gamma_Q(t)$.

Now due to the well-known isotope effect, the change of T_c with the change of nuclear mass upon isotopic exchange, provides direct evidence for the phonon-mediated mechanism in the BCS superconductor. Since the discovery of high-T_c materials, many effects have been shown in isotope effect studies. There exist small isotope exponents, $\alpha = -\log T_c/\log M$, 0.12 and 0.04 for LSCO and $YBCO_7$, respectively. The non-zero isotope exponent produces doubts about the exclusion of a phonon-mediated model although the discussion above supports strongly the spin-fluctuation-mediated model.

Recently Raffa *et al.*[72] measured the $1/T_1$ value of Cu in $YBCO_8$ where ^{16}O is partly replaced by ^{18}O. They found that $1/T_1$, ν_Q of Cu, and the lattice constant change slightly with the exchange and that the decrease in the spin gap temperature, T^*, scales to the decrease in T_c thus indicating that the isotope exchange induces changes not only in the phonon frequency but in the electronic state. Ohno *et al.*[73] found that $1/T_1$ values above T_c scale to T/T_c over all of the temperatures measured as in Figs 27(a)[72] and (b),[73] indicating that T_c decreases with the decrease in $\Gamma_Q(t)$, similar to $YBCO_7 + Ni$. To see the scaling more clearly, the change in $1/T_1$ due to the $^{16}O-^{18}O$ exchange is plotted in the inset of the figures.[73] It is proposed that the decrease in T_c due to the exchange does not arise from the increase in the atomic mass which would decrease the phonon frequency, but is due to the decrease in the spin fluctuation energy. In Fig. 28 the isotope exponent α is plotted against $1/T_1T(A-4B)^2 \sim 1/\Gamma_Q$.[73] α is larger for smaller Γ_Q values.

One also finds that the $1/T_1$ value in Ni 2% substituted $YBCO_8$ also scales reasonably well with T/T_c, as seen in Figs 29(a) and (b).[74]

One of the most promising mechanisms for high-T_c superconductivity is given by the antiferromagnetic spin-fluctuation(AFSF)-mediated superconducting model proposed by Moriya *et al.*[57] and Pines *et al.*[75] In both theories, T_c is proportional to $\Gamma_Q\xi^2$. Moriya *et al.* adopt the value of $1/T_1$ and the resistivity to estimate T_c, while Pines *et al.* use $1/T_1$ and $1/T_{2G}$.[76] Their estimates for $YBCO_7$ agree well with the experimental result. Here we show the results obtained by Zheng *et al.*[36] and Magishi *et al.*[39] in Tl2223, Hg1223, etc. following the discussion provided by Pines *et al.*

The Gaussian spin echo decay rate $1/T_{2G}$ through the spin fluctuations is expressed as

$$\left(\frac{1}{T_{2G}}\right)^2 \propto \left(\sum_q F_c(q)^4\chi(q)^2 - \left[\sum_q F_c(q)^2\chi(q)\right]^2\right) \tag{35}$$

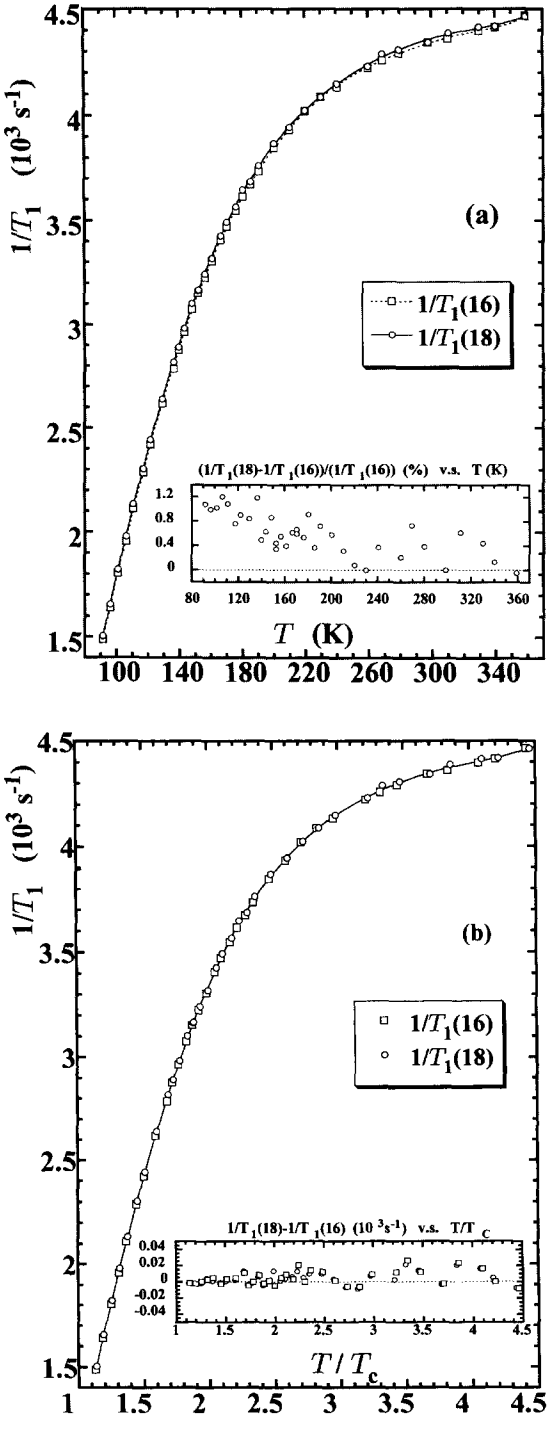

Fig. 27. A plot of $1/T_1$ for Cu in the CuO_2 plane in $YBCO_8$ with $(1/T_1(18))$ ar without $(1/T_1(16))$ ^{18}O against T(a) and T/T_c(b).

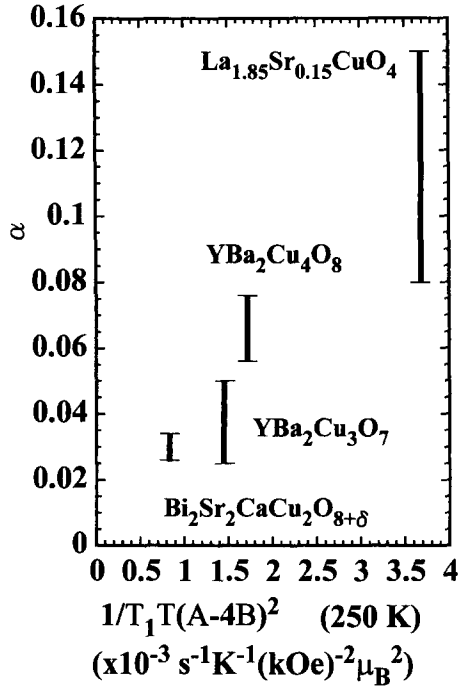

Fig. 28. Isotope exponent α plotted against $1/T_1T(A-4B)^2 \sim 1/\Gamma_Q$ at 250 K.

which is, by using (32) with two-dimensional q-summation, reduced to

$$\frac{1}{T_{2G}} \propto (A_c - 4B)^2 \frac{\chi_Q}{\xi} \tag{36}$$

Thus, combining Eqs (33) and (36), one obtains

$$\frac{(1/T_1T)_c}{(1/T_{2G})^2} \propto \frac{(A_{a,b} - 4B)^2}{(A_c - 4B)^4} \frac{1}{\Gamma_Q \chi_Q} \tag{37}$$

Figure 30 shows

$$\frac{\chi_Q}{\xi^2 \Gamma_Q} \propto \frac{1}{(A_{a,b} - 4B)^2} \left(\frac{1}{T_1T}\right)_c \tag{38}$$

plotted against temperature in several high-T_c materials. Figure 31 shows $1/T_{2G}$ values for several compounds. By using Eq. (37) with the data given in

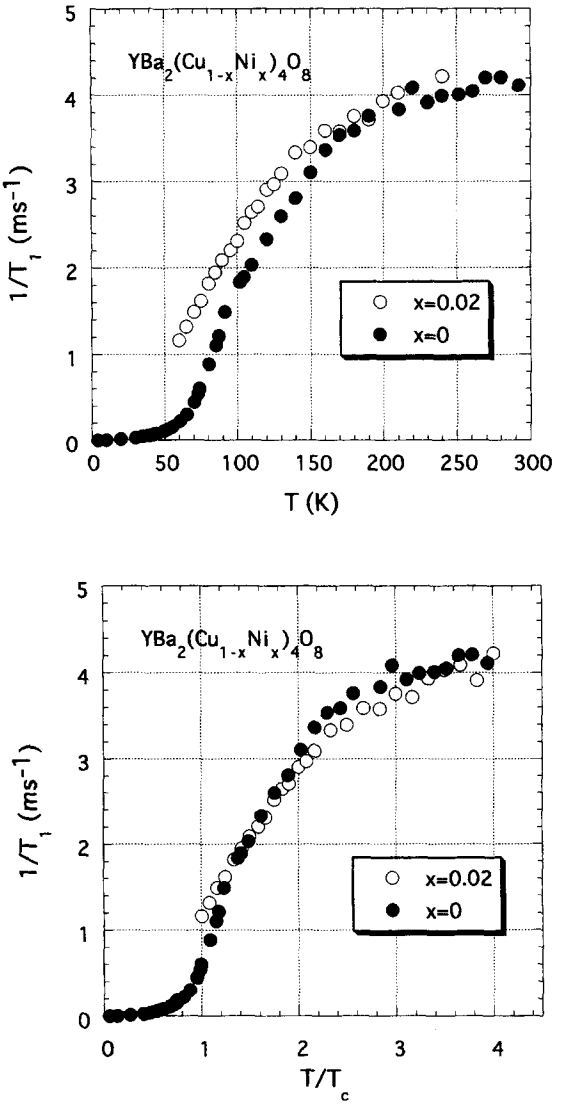

Fig. 29. A plot of $1/T_1$ for Cu in the CuO_2 plane in $YBCO_8$ with Ni against (a)T and (b)T/T_c.[74]

Figs 30 and 31, $\chi_Q\Gamma_Q$ values are obtained as shown in Fig. (32). Figure 33, shows T_c plotted against $\chi_Q\Gamma_Q$.[36,39] In Tl2223 and Hg1223, there exist two CuO_2 layers, 4 and 5-fold CuO_2 planes having different $\chi_Q\Gamma_Q$ values, as in Fig. 32. In Fig. 33 the larger value of $\chi_Q\Gamma_Q$ is adopted. The value of $\chi_Q\Gamma_Q$ in $YBa_2Cu_4O_8$ decreases with increasing temperature. Here the value at high

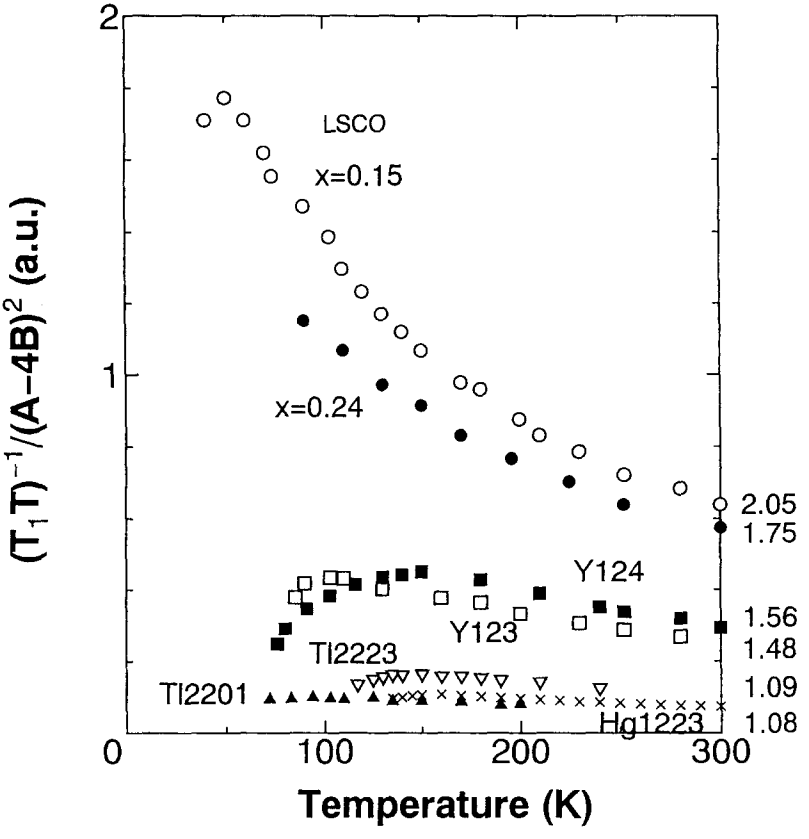

Fig. 30. A plot of $1/(T_1T)\cdot 1/(A-4B)^2 \propto \chi_Q/\Gamma_Q\xi^2$ against T. The numbers on the right side indicate the number of holes at the Cu site obtained from the NQR frequency as mentioned in reference 74.

temperature is used, where $\chi_Q\Gamma_Q$ approaches a constant value above 500 K.[77] Now χ_Q is proportional to ξ^2, $\chi_Q/\xi^2 = D$. If we assume the D values are almost the same for all high-T_c materials, T_c is nearly proportional to $\Gamma_Q\xi^2$, as seen in Fig. 33, which supports the AFSF-mediated superconducting model.

Figures 34(a) and (b) show $1/T_{2G}$ values plotted against temperature and T/T_c in the $YBCO_7$ + Ni system.[78] $1/T_{2G}$ is scaled to T/T_c indicating that χ_Q/ξ is independent of x, when t is fixed. In the $YBCO_7$ + Ni system χ_Q/ξ^2 is considered to remain constant with x so that $\chi_Q/\xi = \xi$ is independent of x when t is fixed. Then combining Eq. (34) with this result, $T_c \propto \Gamma_Q\xi^2$ is confirmed, which supports again the AFSF-mediated superconductivity model. The temperature dependence of $\Gamma_Q\xi^2$ and the relation between T_c and $\Gamma_Q\xi^2$ are also shown in Figs 32, 33 and 35, respectively.

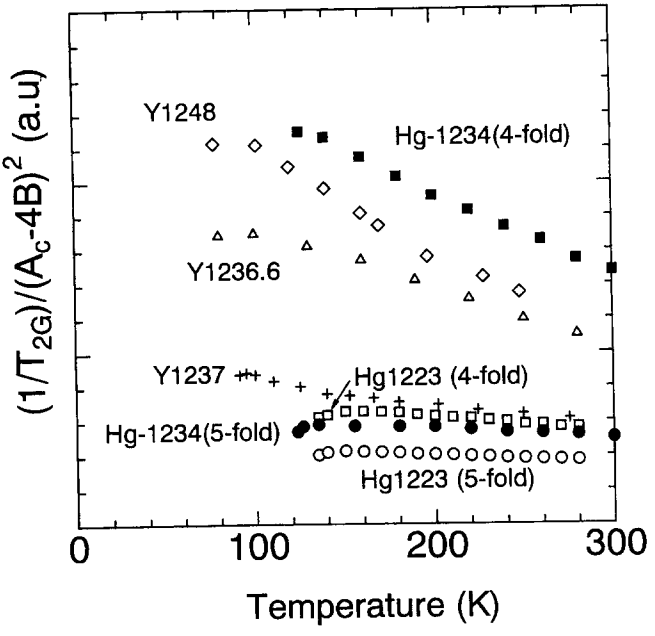

Fig. 31. A plot of $(1/T_{2G})/(A_c - 4B)^2$ for several high-T_c materials.

The value of $T_c = 123$ K in Hg1234 is lower than the 134 K found in Hg1223. Hg1234 has four CuO_2 layers: two 4-fold and two 5-fold layers. As seen in Fig. 36, the $1/T_1T$ value of the 4-fold Cu is larger than the 5-fold Cu.[40] The values of $1/T_1$ show a spin gap behaviour which is characteristic of the underdoped system. $T_1T/(T_{2G})^2$ is temperature independent at the 5-fold site, while T_1T/T_{2G} is constant with temperature at the 4-fold site, as seen in Fig. 37, indicating that the holes are lightly doped at the 4-fold and heavily doped at the 5-fold site. The $\chi_Q\Gamma_Q$ value at the 5-fold site is lower than at the 4-fold site in Hg1223. Thus T_c is considered to be determined by the spin fluctuation of the 4-fold site. The slightly lower T_c value of Hg1234 compared with that of Hg1223 is attributed to the low hole doping at the 4-fold Cu site. If more holes could be introduced by doping at the 4-fold site, the value T_c would increase above that for Hg1223. The electronic states in multilayered high-T_c cuprates are discussed in detail later.

4.4. Spin gap in high-T_c superconductors

In the previous Section we analysed the normal-state properties of high-T_c superconductors, based on the Fermi-liquid picture. In this Section we discuss some aspects which seemingly contradict the Fermi liquid theory, in particular

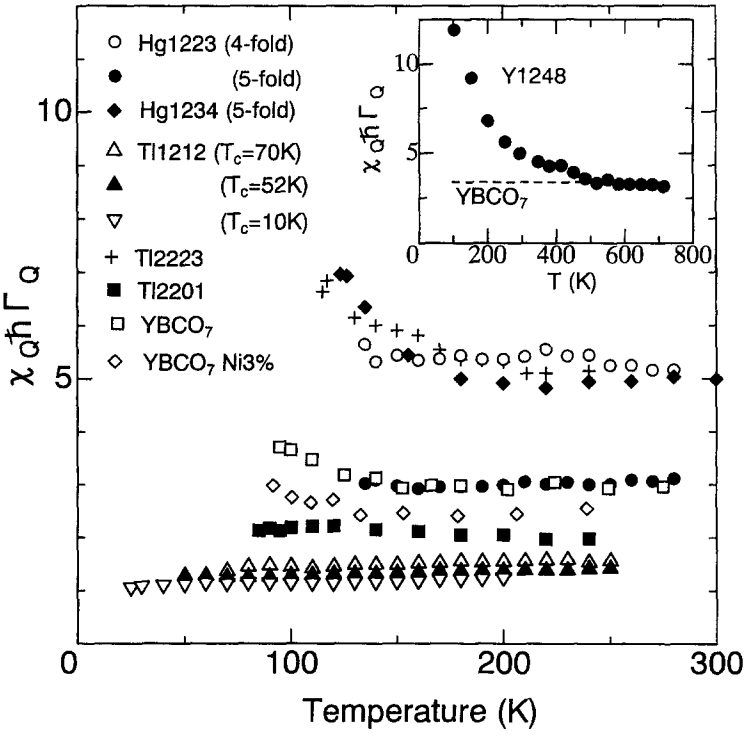

Fig. 32. A plot of $\chi_Q \Gamma_Q \propto (A_{a,b} - 4B)^2 (T_1 T)_c / (A_c - 4B)^4 T_{2G}^2$.[3(e)]

in the underdoped region. Among these, the so-called spin gap or pseudogap, which is a phenomenon of spectral weight suppression below a characteristic temperature T^*, has attracted much attention in recent years. We review the impurity effect on the pseudogap in the underdoped regime, the carrier density dependence of the spin gap in Bi2212 and the high magnetic field responses of the pseudogaps.

4.4.1. Impurity effect in underdoped regime

The effect of impurities on the pseudogap[79] in the underdoped regime has provided the following insights. (1) Decrease in the susceptibility at $q = 0$ and $q = Q$, both of which are independently ascribed to some kind of pseudogap, arising from different origins. (2) Substitution of a non-magnetic impurity for Cu enhances the χ_Q value below T^*. This result reconciled two long-standing, divergent streams of identifying pseudogap temperatures. One of them identifies the pseudogap temperature with the temperature at which χ_0 decreases while the other identifies with the temperature at which χ_Q or $1/T_1 T$ shows a broad peak. Since these two temperatures differ considerably, they

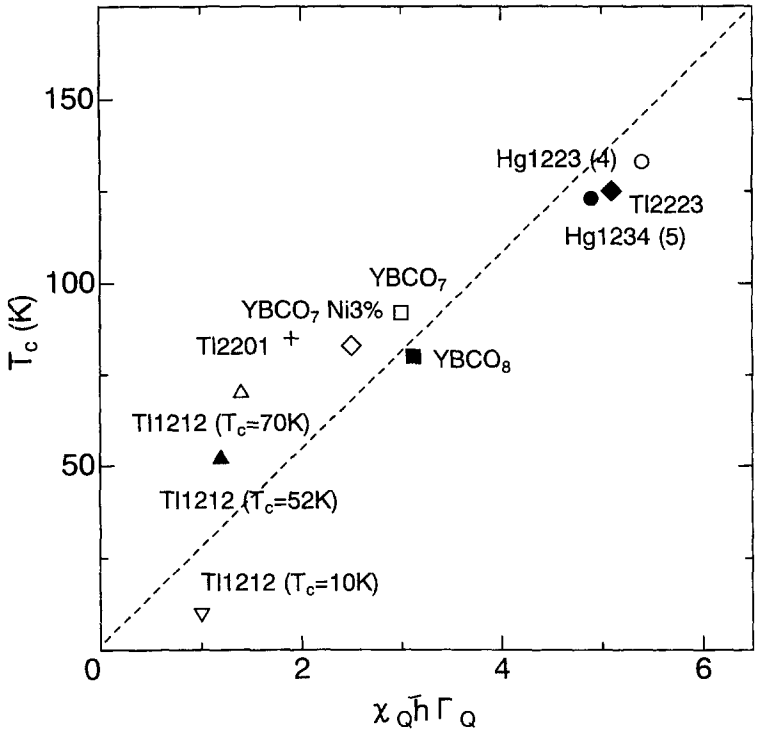

Fig. 33. T_c plotted against $\chi_Q \Gamma_Q$.

have caused considerable confusion in the literature concerning the pseudogap temperature.

Figure 38 shows the temperature-dependence of the Knight shift in pure and Zn-doped $YBa_2Cu_4O_8$: no effect of Zn is seen on the Knight shift. Figure 39 shows $1/T_1T$ plotted as a function of temperature, T, and the concentration of Zn. In contrast to the Knight shift result, it is seen that the pseudogap behaviour is sensitive to impurities, in particular it is very susceptible to the non-magnetic impurity Zn. Substitution of 1% of Zn for Cu enhances χ_Q so strongly that the pseudogap becomes invisible.

A similar enhancement of χ_Q by Zn impurity was reported from neutron scattering experiments. Kakurai *et al.*[80] and Harashina *et al.*[81] found a substantial number of low energy excitations that emerge upon substituting 5% of Zn in $YBa_2Cu_3O_{6.6}$, which is a compound similar to $YBa_2Cu_4O_8$ in many respects. Recent reports have confirmed such a 'filling up' of the pseudogap.[82–84] These results are consistent with our findings since $1/T_1T$ probes the initial slope of the imaginary part of χ_Q. It is still unclear if this enhancement of χ_Q is due to a new state induced within the gap[85] or if it is due to collapse of the pseudogap.[86]

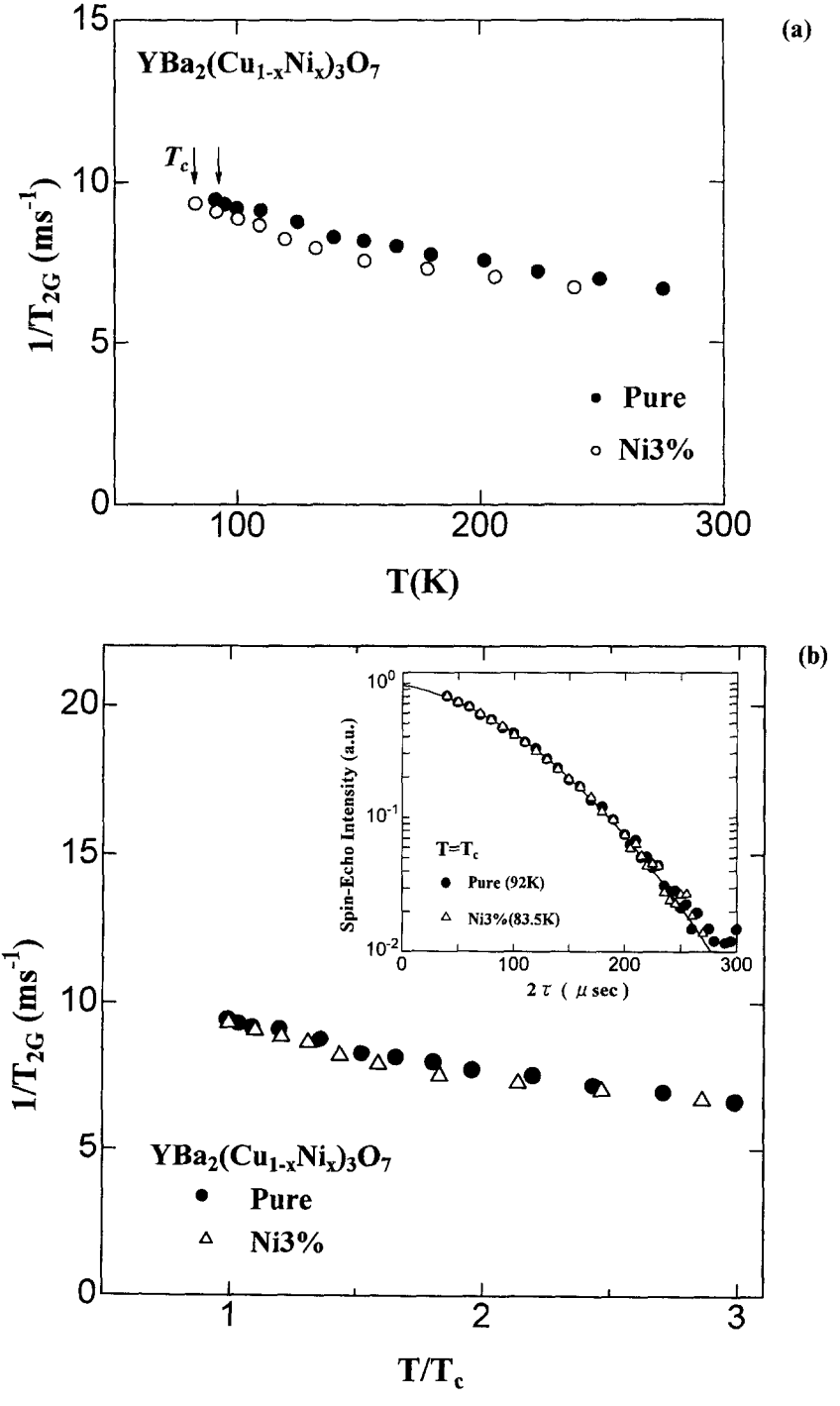

Fig. 34. A plot of $1/T_{2G}$ for Ni-doped $YBCO_7$ against (a) T and (b) T/T_c.[78] The inset shows the spin echo decay curve at T_c values for $x = 0$ and 3%.

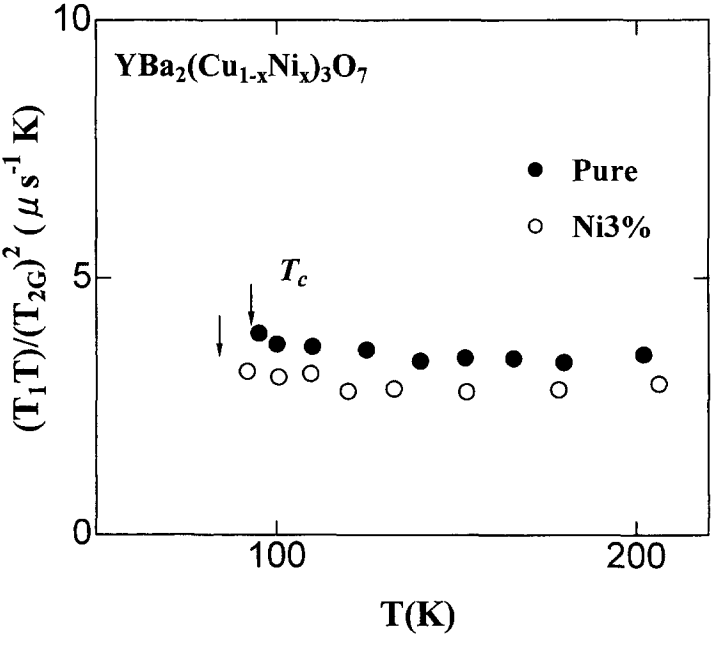

Fig. 35. $T_1T/(T_{2G})^2 \propto \Gamma_Q\xi^2$ plotted against T in Ni-doped $YBCO_7$.[78]

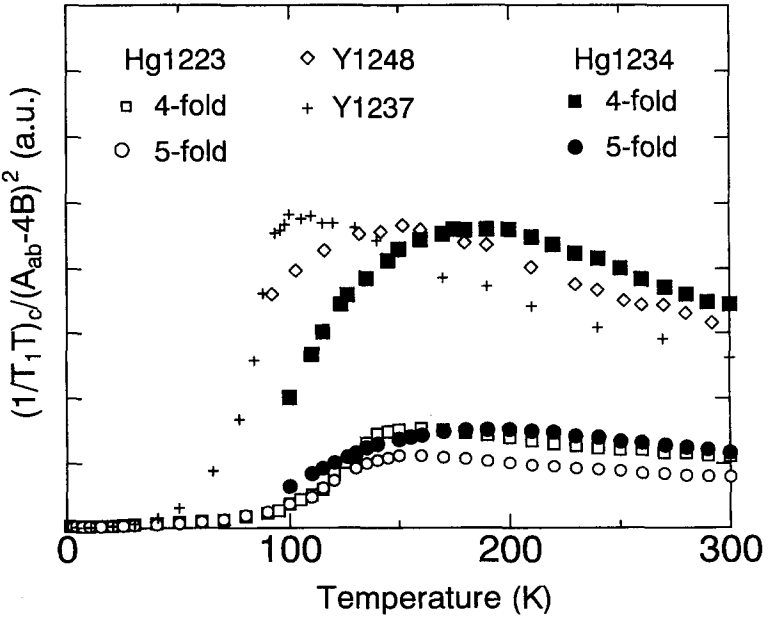

Fig. 36. A plot of $1/T_1T(A-4B)^2$ for Cu at the 4-fold and 5-fold sites in Hg1234 and Hg1223.[40]

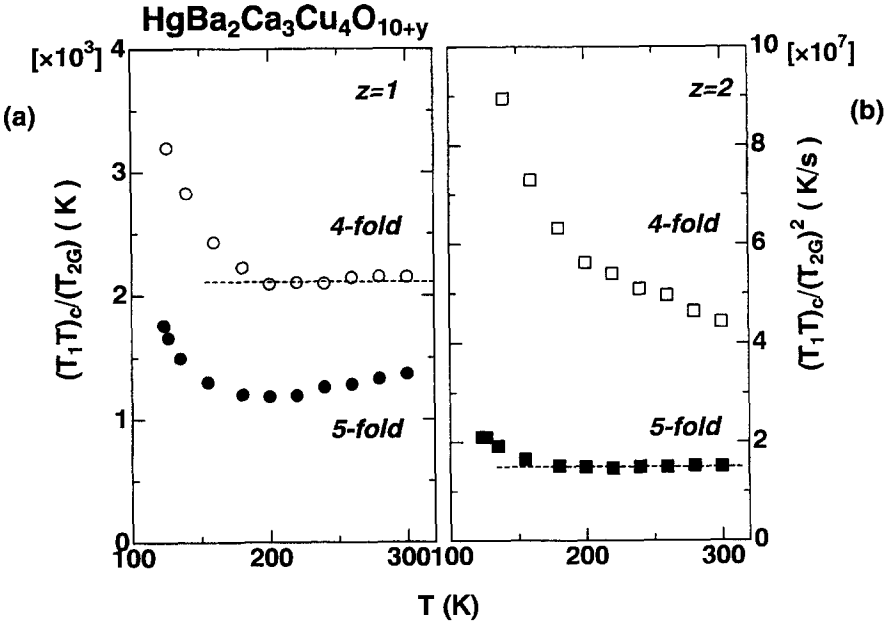

Fig. 37. (a) $(T_1T)_c/T_{2G}$ and (b) $(T_1T)_c/(T_{2G})^2$ plotted against T for 4- and 5-fold Cu in Hg1234.[40]

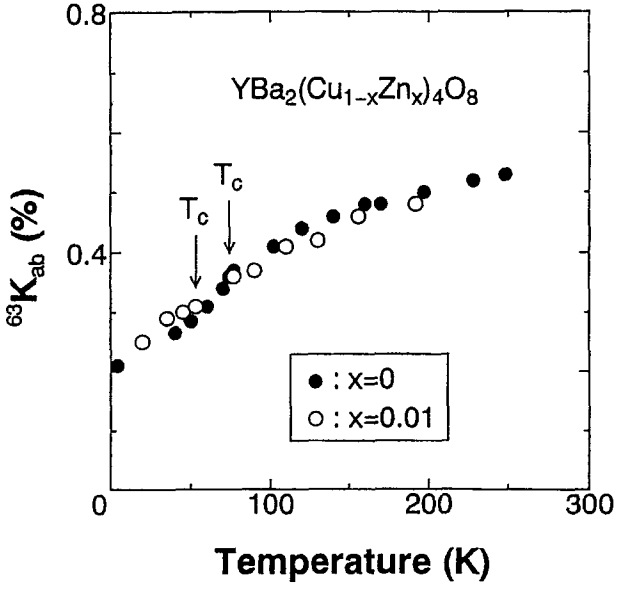

Fig. 38. Knight shift in pure and Zn-substituted $YBa_2Cu_4O_8$.[79]

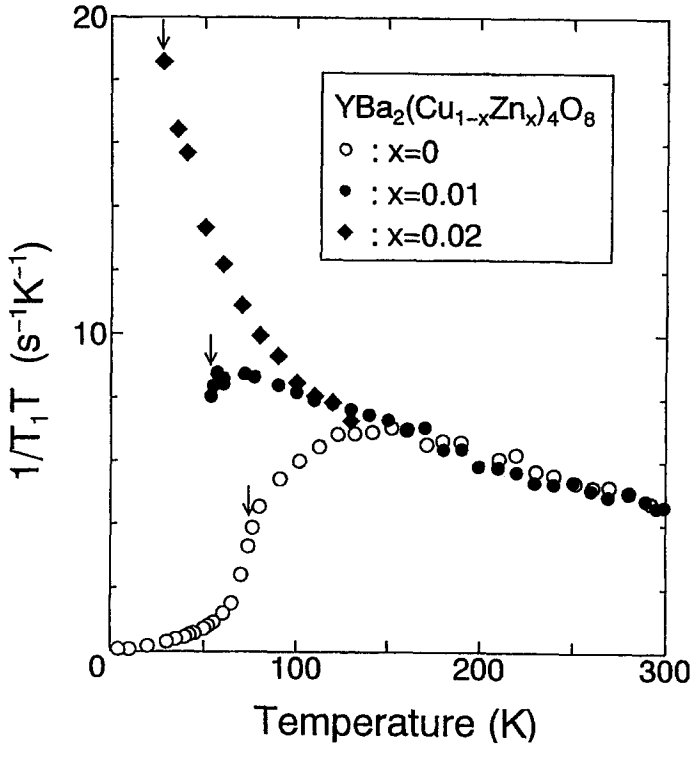

Fig. 39. A plot of $1/T_1T$ for pure and Zn-substituted $YBa_2Cu_4O_8$.[79] The arrows indicate respective T_c values.

4.4.2. Carrier density dependence of the spin gap in Bi2212

Figures 40(a) and 41 show the temperature dependence of $1/T_1T$ and K in Bi2212.[87] In Fig. 41, the K values of ^{17}O are indicated by open circles.[88] The T^* value below which K starts to decrease is far above the temperature at which $1/T_1T$ begins to decrease. Ishida *et al.*[87] have shown that the T^* values for $1/T_1T$, K and electric resistivity[89] and those determined from an angle-resolved photoemission spectroscopy (ARPES)[90,91] study, where a pseudogap of $d_{x^2-y^2}$ symmetry starts to open, all agree with each other if one adopts a temperature below which K starts to decrease sharply, which is shown in Fig. 41 as T^*. This indicates that the pseudogap opens not only in the low-energy components of the AFSF, but in the density of states of the one-electron energy spectrum. The temperature below which χ_s or K_s begin to decrease is not attributed to the opening of the spin gap but to a decrease in χ_0 associated with an increase in χ_Q.

Figure 42 shows the temperature-dependence of $1/T_{2G}$ for under-, optimally and overdoped Bi2212.[92] The increase in $1/T_{2G}$ upon cooling moderates as the hole content increases. This indicates that ξ decreases with increasing hole

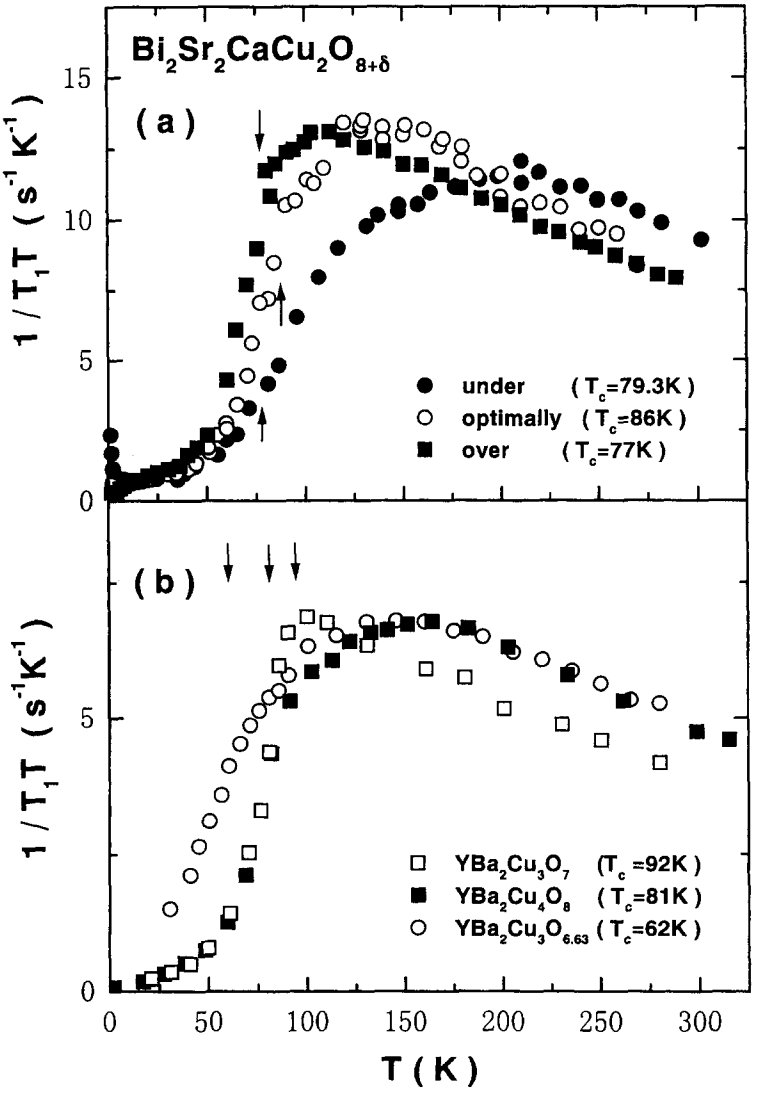

Fig. 40. A plot of (a) $1/T_1T$ for Cu in under-, optimally and overdoped Bi2212.[87] (b) $1/T_1T$ in YBCO6.6, Y1248 and Y1237.[102]

content. Below 300 K, $1/T_{2G}$ increases gradually with decreasing temperature, and saturates below T^* in the underdoped and optimally doped Bi2212. The fact that $1/T_{2G}$ remains almost constant below T^* is indicative of the saturation of the magnetic correlation length ξ. In other words, the spectral weight of AFSF is transferred from the low- to the high-energy range in this temperature region. With a further decrease in temperature, $1/T_{2G}$ starts to

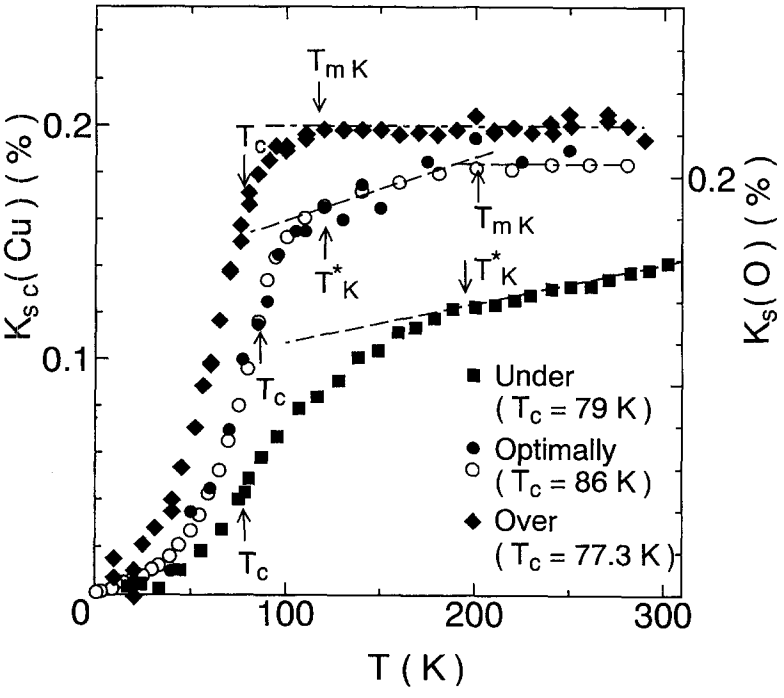

Fig. 41. A plot of K for Cu in under-, optimally and overdoped Bi2212.[87] K for ^{17}O is given in reference 88.

decrease below T_c^* but successively below T_c. This is corroborated by the $1/T_1T$ and K_s data. Below T_c^*, the density fluctuation of the Cooper pairs is suggested to emerge regardless of the doping level.[92]

The values of T_{mK}, T^* and T_c^* obtained using several kinds of measurement are shown in Fig. 43 for Bi2212 plotted against the hole content.[87,92] T_{mK} and T^* are both progressively increased with decreasing hole content towards the AFM-SC phase boundary. However, the T_c^* value shows a moderate doping dependence and tends to saturate in the underdoped regime.

4.4.3. Magnetic field effect on the spin gap

Application of a strong magnetic field beyond 20 T, which was recently performed by Zheng, has contrasted the pseudogap property sharply in the underdoped and overdoped regimes.[93–95]

Figure 44 shows $1/T_1T$ values and the Knight shift K_c of ^{63}Cu as a function of temperature under zero and strong magnetic fields parallel to the c-axis in the slightly overdoped material $TlSr_2CaCu_2O_{6.88}$ ($T_c = 68$ K).[93] The arrows, from right to left, indicate T_{cH} values at elevated fields. At high temperature $1/T_1T$ increases with decreasing temperature down to

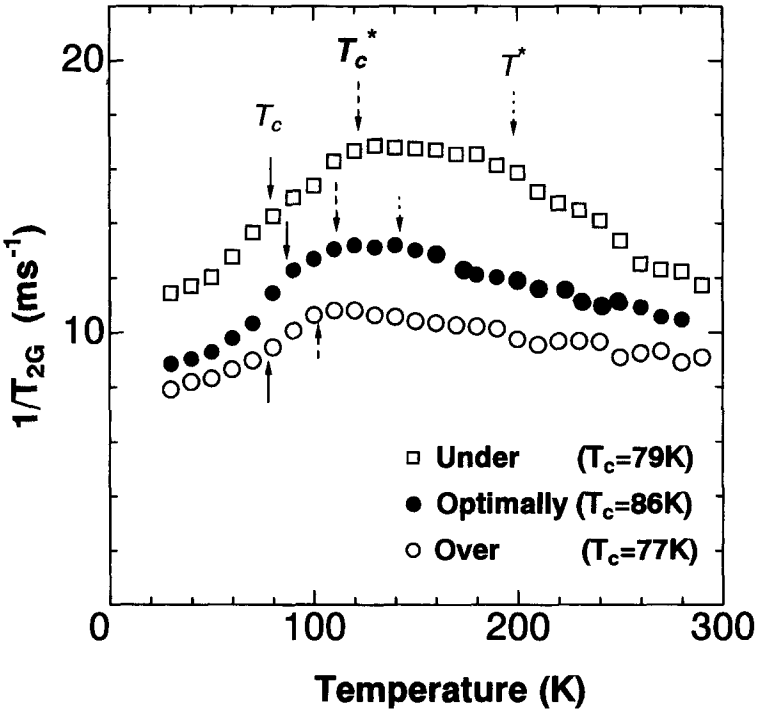

Fig. 42. Temperature dependence of $1/T_{2G}$ for under-, optimally and overdoped Bi2212.

$T^* = 85$ K, and can be fitted to a Curie–Weiss (CW) relation. This is understood to be due to the development of an antiferromagnetic spin correlation. The deviation of $1/T_1T$ from the CW relation has widely been attributed to the loss of low-energy spectral weight, i.e. opening of a spin gap or a pseudogap. As seen in Fig. 44(a), upon applying magnetic fields, T^* is shifted to lower temperature; $1/T_1T$ is strongly field dependent below 85 K. Similar field dependence is observed in the Knight shift, K_c: K_c is constant at high temperature and, as seen in Fig. 44(b), starts to decrease at temperatures above T_{cH}, with no apparent singularity at T_{cH}. The temperature at which K_c starts to deviate from a constant value depends on the field, much like the $1/T_1T$ values.

From such a field dependence of the pseudospin gap, it is concluded that the pseudogap in the overdoped regime is due to the effects of the fluctuating Cooper pair density above T_c; the effect of the strong magnetic field is to quench the superconducting fluctuations.[93]

In contrast, the field response of the pseudogap is quite different in the underdoped material $YBa_2Cu_4O_8$.[95] Figure 45 shows the temperature dependence of $1/T_1T$ for ^{63}Cu in the CuO_2 plane in $YBa_2Cu_4O_8$ at various magnetic field strengths.[84] At high temperature, the $1/T_1T$ value increases with

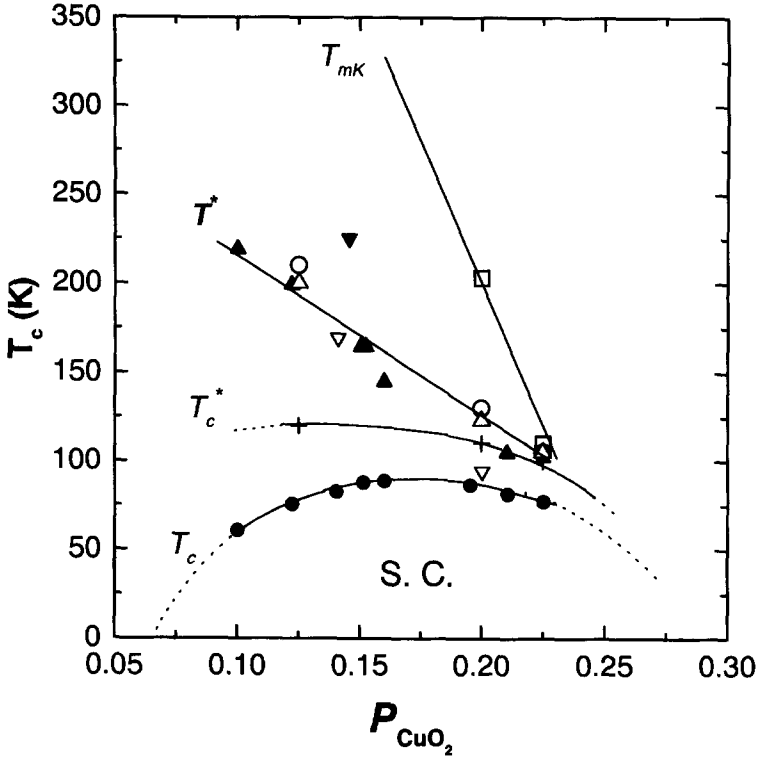

Fig. 43. T_c and T^* plotted against hole content in Bi2212 determined by several measurements.[87,92] (●: T_c; ○: T^* at which $1/T_1T$ shows a broad peak; △: T_K^* at which K shows a sharp decrease as seen in Fig. 41; ▲: T_ρ^* at which the resistivity deviates downward from the linear relation;[89] T_{ARPES}^* at which the opening of the pseudogap was found by Ding *et al.*[90] (▼) and Harris *et al.*[91] (▽); □: T_{mK} at which K starts to decrease. +: T_c^* below which $1/T_{2G}$ decreases markedly, but successively below T_c.)

decreasing temperature down to $T^* = 160$ K, and can be fitted to a CW relation. Even though a magnetic field of 23.2 T reduces T_c by 20 K and the properties below T_{cH} are strongly dependent on the field strength, the pseudogap is not affected by the field. This property of the spin gap, together with its response to impurities, may put a constraint on theories for the pseudogap in the underdoped regime.

The contrasting response of the pseudogap in different doping regimes may suggest that a crossover either in the magnetic nature of the coupling strength takes place in high-T_c cuprates upon doping.[95] If the pseudogap in the underdoped regime is due to electron–electron correlations, the results imply that such a pseudogap terminates at some point before entering the overdoped regime. However, one may also view the results as indicating a smooth crossover of the cuprates from a strong coupling regime in the underdoped region to a weak coupling regime in the overdoped region.[96] More work needs

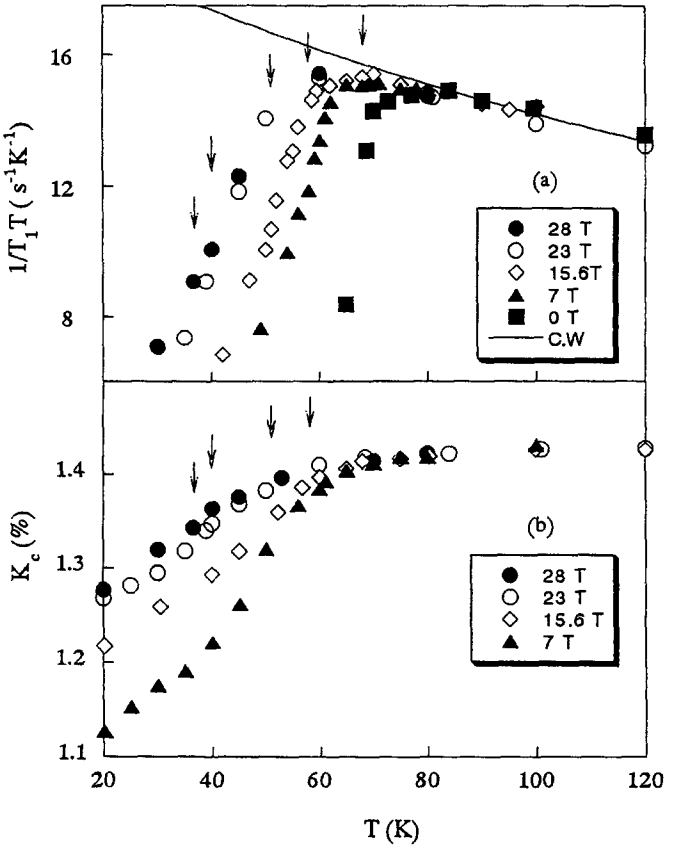

Fig. 44. Temperature and field dependence of $1/T_1T$ and the Knight shift in overdoped $TlSr_2CaCu_2O_{6.88}$ at fields up to 28 T.

to be done to clarify this important issue concerning the fundamental properties of the normal state of high-T_c superconductors.

As for the origin of the pseudogap behaviour, there are controversial discussions at present based upon the following:

(1) singlet formation associated with the RVB state;[97]
(2) precursor to superconductivity;[96,98]
(3) nesting effect;[99]
(4) spin fluctuation;[100]
(5) short range magnetic order.[101]

Although there is no decisive evidence to distinguish the origin at the present, the following experimental facts may be important.

(1) As shown in Fig. 46 the $1/T_1T$ value at the 4-fold site is larger than that at the 5-fold site, indicating that the Cu at the 4-fold site is doped with

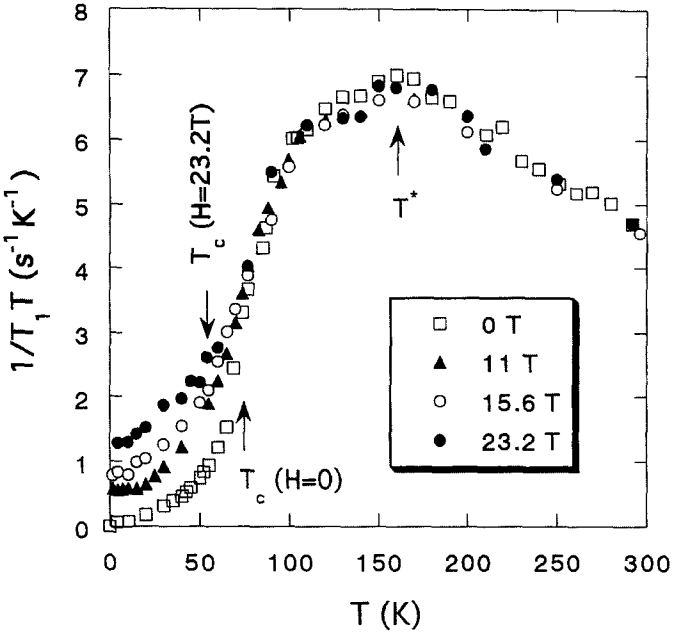

Fig. 45. Temperature and field dependence of $1/T_1T$ in underdoped $YBa_2Cu_4O_8$.[95]

fewer holes thus belonging to the underdoped system. However as shown in the inset of Fig. 46 the ratio of $1/T_1T$ at the 4-fold site to that at the 5-fold site has no anomaly around T^* indicating that the pseudogap opens at both sites.[40] This means that a gap is induced even at an optimally doped site when a gap opens at neighbouring sites.

(2) Raffa *et al.*[72] found that the decrease in $1/T_1T$ scales to T_c when ^{16}O is replaced by ^{18}O in $YBCO_8$, indicating that T_c is strongly correlated to T^*.

(3) As shown in Fig. 40(a) and (b), the maximum value of $1/T_1T$ is almost the same for each of the systems, YBCO and Bi2212. The gap seems to open when $1/T_1T$ or $\chi_Q/\Gamma_Q\xi^2$ reaches a critical value for each system.[102]

(4) A magnetic field reduces the spin gap behaviour in overdoped materials but not in underdoped materials.

4.5. Effect of hole distribution on superconducting characteristics of multilayered systems

$CuBa_2Ca_3Cu_4O_{12+y}$ (Cu-1234) is one of the promising systems for a high performance superconductor because of a low superconducting (SC) anisotropy and high T_c superconductivity with high hole concentration in the overdoped region.[103] Recently, Cu NMR measurements on Cu-1234 were performed, and it was revealed that their remarkable SC characteristics

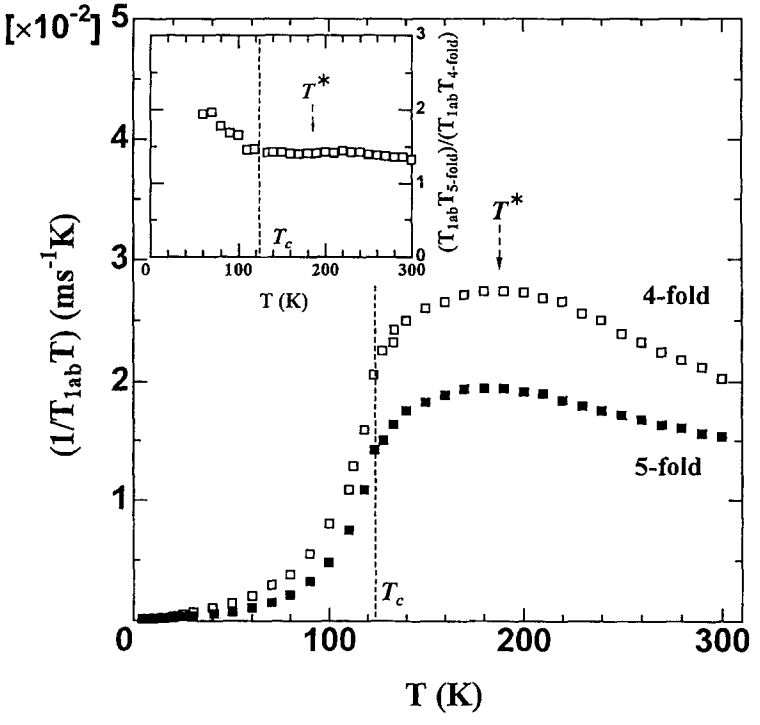

Fig. 46. A plot of $1/T_1T$ for Cu at 4- and 5-fold Cu sites in Hg1234. Their ratio is shown in the inset.[40]

originate from the difference in local hole concentration between two inequivalent kinds of CuO_2 planes.[41]

Holes are homogeneously doped into the planes in mono- or bi-layer high-T_c cuprates, since all planes are crystallographically equivalent. This is, however, not the case in multilayered high-T_c cuprates which include three or more CuO_2 planes in a unit cell. In these compounds, there exist two inequivalent CuO_2 planes in a unit cell, i.e. the outer CuO_2 planes (denoted as OP) with a pyramidal (five) oxygen coordination and the inner plane (IP) with a square (four) oxygen coordination.

Tokunaga *et al.* found that a linear relation exists between the spin Knight shift and the hole number in the CuO_2 plane, δ, obtained from ν_Q values in mono- and bi-layer cuprates,[60] $\delta = 0.0462 + 0.502K_s^{300K}(\%)$, as shown in Fig. 47. Using this relation, they obtained the hole number at each plane, δ_{IP} and δ_{OP} from the spin Knight shift of Cu at $T = 300$ K perpendicular to the c-axis, K_s^{300K} at each plane in Hg- and Cu-based multilayer cuprates.[104] These are plotted against the average value $\delta_{av} = (2\delta_{IP} + (n-2)\delta_{OP})/n$ in Fig. 48. In all of the samples, it is found that $\delta_{IP} < \delta_{OP}$. The difference between δ_{IP} and δ_{OP} increases in going from

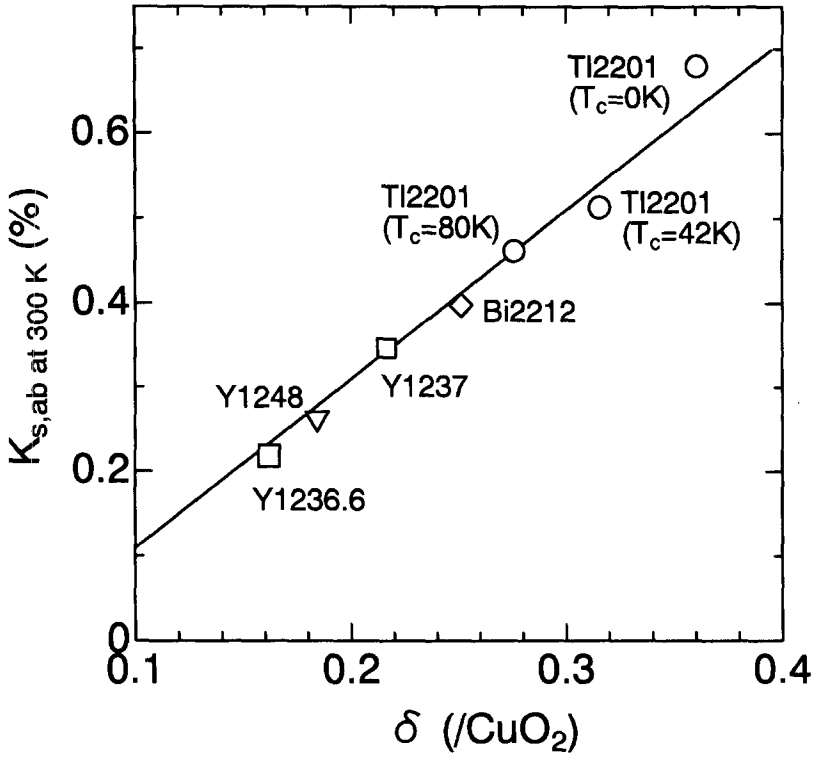

Fig. 47. The spin Knight shift of Cu at $T = 300$ K. K_s^{300K} values perpendicular to the c-axis are plotted against the hole number in the CuO_2 plane, δ, obtained from ν_Q[60] in mono- and bi-layer cuprates. The solid line shows a linear relation between K_s^{300K} and δ, $\delta = 0.0462 + 0.502K_s^{300K}(\%)$.

the under- to overdoped regions. Furthermore, one can see that the inhomogeneity is also enhanced by an increase in the number of CuO_2 planes, n. The ratio $R_h = \delta_{OP}/\delta_{IP}$ is $R_h = 1.14$ ($n = 3$), 1.49 ($n = 4$) and 1.64 ($n = 5$), respectively at $\delta_{av} \sim 0.21$. It should be noted that strong inhomogeneity of the hole distribution is observed in overdoped Cu-1234 ($n = 4$, $\delta_{av} = 0.25$), where the OP is in the overdoped region, while the IP is still in the underdoped region.

Figure 49 shows the temperature dependences of (a) K_s, and (b) the T-derivatives, dK_s/dT for the IP and the OP in overdoped Cu-1234.[41] The K_s value for IP markedly decreases below $T_c = 117$ K, whereas that for the OP decreases gradually below T_c but markedly below 60 K. As a result, the temperature-derivative, dK_s/dT shows a distinct peak just below T_c in the IP, while it is at 60 K in the OP. The different temperature dependence of K_s in the SC state indicates that the SC order parameter does not develop simultaneously between the IP and the OP.

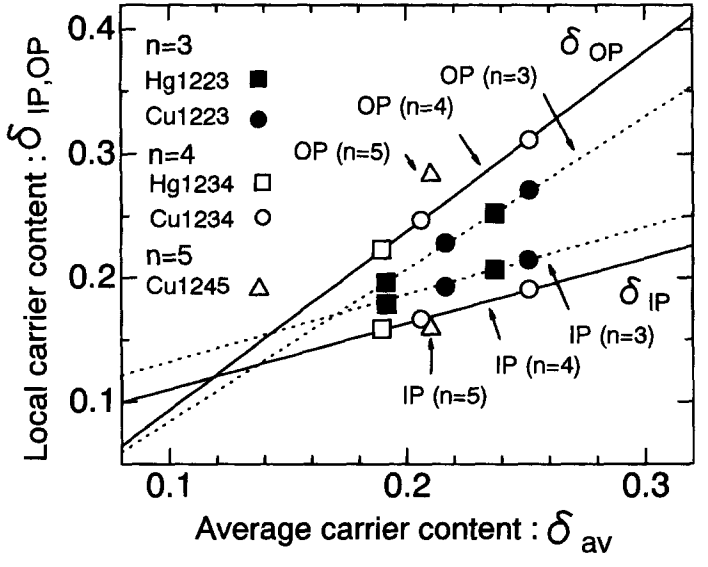

Fig. 48. The doping dependence of the local hole number at the IP and the OP in $n = 3$, 4, and $n = 5$ multilayer cuprates.[104]

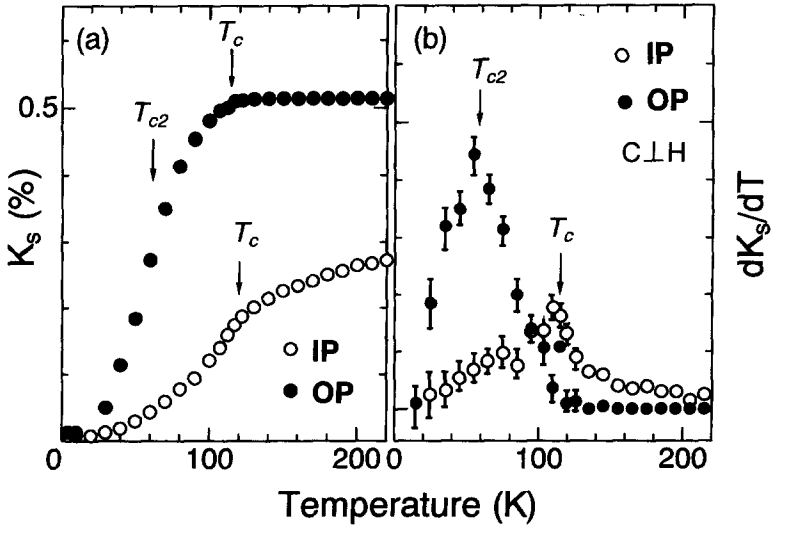

Fig. 49. The temperature-dependences of (a)K_s and (b) the temperature-derivative changes, dK_s/dT, for the IP and the OP in overdoped Cu-1234.[41]

In order to deduce the temperature dependence of the SC gap $\Delta(T)$ below T_c, $K_s(T)/K_n$ is normalized by the value K_n at $T_c = 117$ K and is plotted against T/T_c in Fig. 50. It is clear that $\Delta(T)$ in the OP does not fully develop down to T_{c2} in contrast to that found for the IP. A two-dimensional (2D) *d*-wave model has been applied to fit the data for the OP. A model with $\Delta_{MF}(T)$ following a conventional mean-field (MF) type is not in accord with the dull decrease of $K_s(T)/K_n$ in the OP between $T_{c2} = 60$ K and $T_c = 117$ K. Alternatively, the agreement between the experiment and the calculation seems to be satisfactory when it is assumed that $\Delta(T)/\Delta(0)$ increases linearly down to $T_{c2} = 60$ K and follows the MF type below T_{c2}, as shown by the solid line in the inset of Fig. 50. This result shows that the gap in the OP does not fully develop below $T_c = 117$ K but does so below $T_{c2} = 60$ K.

The decoupling of SC characteristics among the CuO_2 planes is a novel phenomenon in high-T_c superconductors, and suggests that the strength of the SC pairing interaction can be determined individually at each plane, when the difference between their doping levels becomes large. Noting that the doping

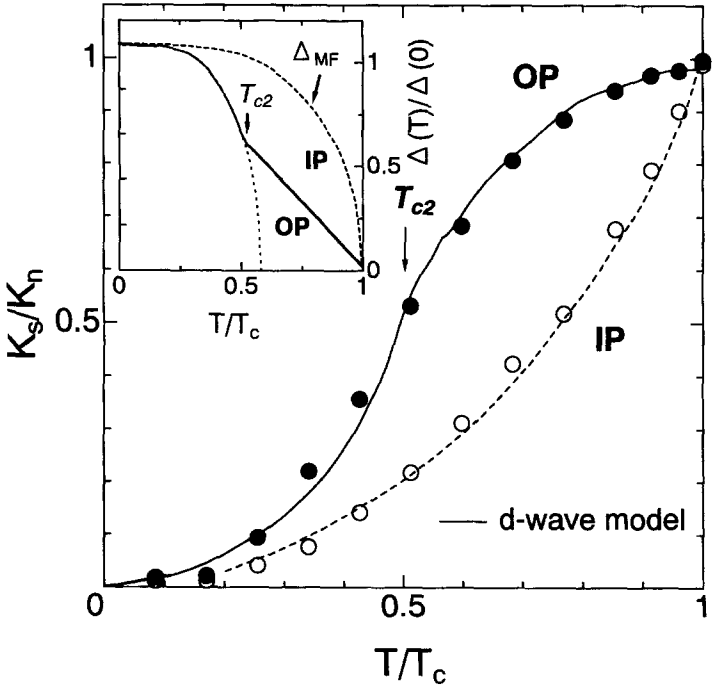

Fig. 50. $K_s(T)/K_n$ vs T/T_c plot for the IP and the OP. $K_s(T)$ and K_n are the Knight shift in the superconducting region and at T_c, respectively. $K_s(T)/K_n$ for the OP is reproduced by the *d*-wave model assuming a linear increase of $\Delta(T)$ below T_c and follows the BCS form below T_{c2} as shown in the inset.[41]

level in the OP is compatible with those in overdoped Tl-1212 with T_c = 64 K and Tl-2201 with T_c = 43 K, we propose that the crossover temperature, T_{c2} = 60 K corresponds to an inherent SC transition temperature of the OP which originates from the overdoped hole concentration. In Cu-1234, it has been reported that the T_c values are sustained above 116 K even in the overdoped region where the hole concentration per CuO_2 plane is three times larger than the optimum doping value.[105] This insensitivity of T_c to the hole doping seems to be quite unique when compared with other cuprates in which the T_c values are decreased drastically by increasing the hole concentration in

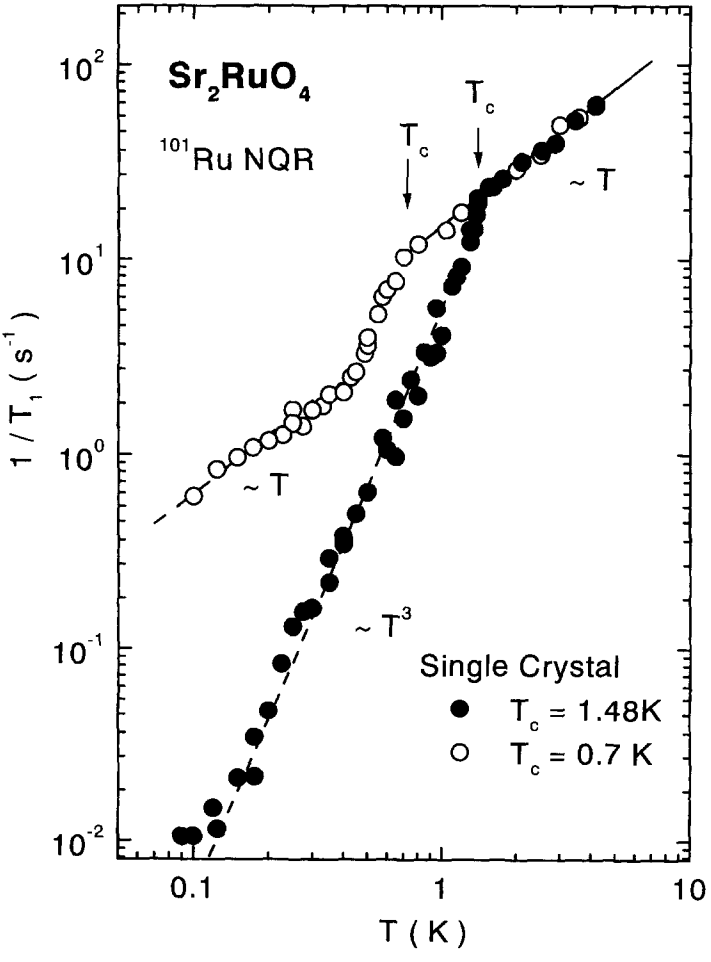

Fig. 51. A plot of $1/T_1$ for ^{101}Ru in single crystals of Sr_2RuO_4 with T_c = 0.7 K[107] and T_c = 1.48 K.[110]

the overdoped region. What the present NMR studies have clarified is that the OP is overdoped, with its doping level being variable, whereas the IP is still in the underdoped region and thus sustains a higher T_c value above 116 K in Cu-1234.

In high-T_c cuprates, it has been proposed that an increase in the number of CuO_2 sheets ($=n$) is a key factor in increasing T_c. However, as shown in Fig. 48, the increase of n induces strong inhomogeneity of hole distribution among the CuO_2 planes, which consequently induces decoupling of the SC characteristic among them. The homogeneous hole doping over all of the CuO_2 plane in large-n systems may be another key factor in increasing the value of T_c in high-T_c cuprates.

5. RELATED COMPOUNDS

NMR results in superconducting Sr_2RuO_4 and YNi_2B_2C are introduced, which have been carried out to determine the symmetry of the Cooper pairs in these compounds.

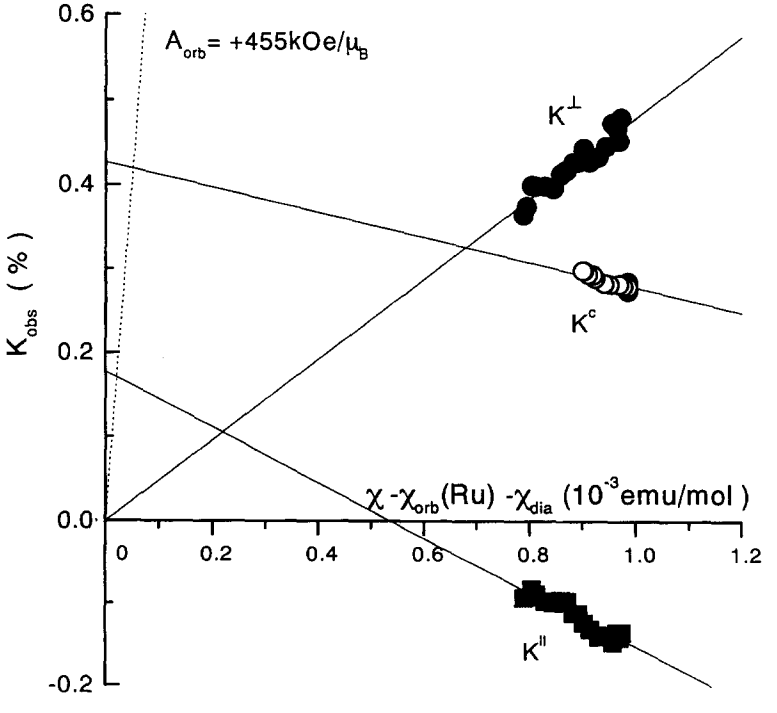

Fig. 52. ^{17}O Knight shift components parallel and perpendicular to the c-axis in Sr_2RuO_4.[112]

5.1. Sr_2RuO_4

Maeno *et al.*[106] found superconductivity in a sample of Sr_2RuO_4 ($T_c \sim 1$ K). This has the same crystal structure as La_2CuO_4 and attracts much attention in exploring the nature of the superconductivity in relation to the Cu oxide high-T_c superconductor.

The spin susceptibility derived from the χ and K values at T_c is enhanced by a factor of ~5.4 as compared with that estimated from the band calculation due to ferromagnetic spin fluctuation,[107,108] and the related cubic compound

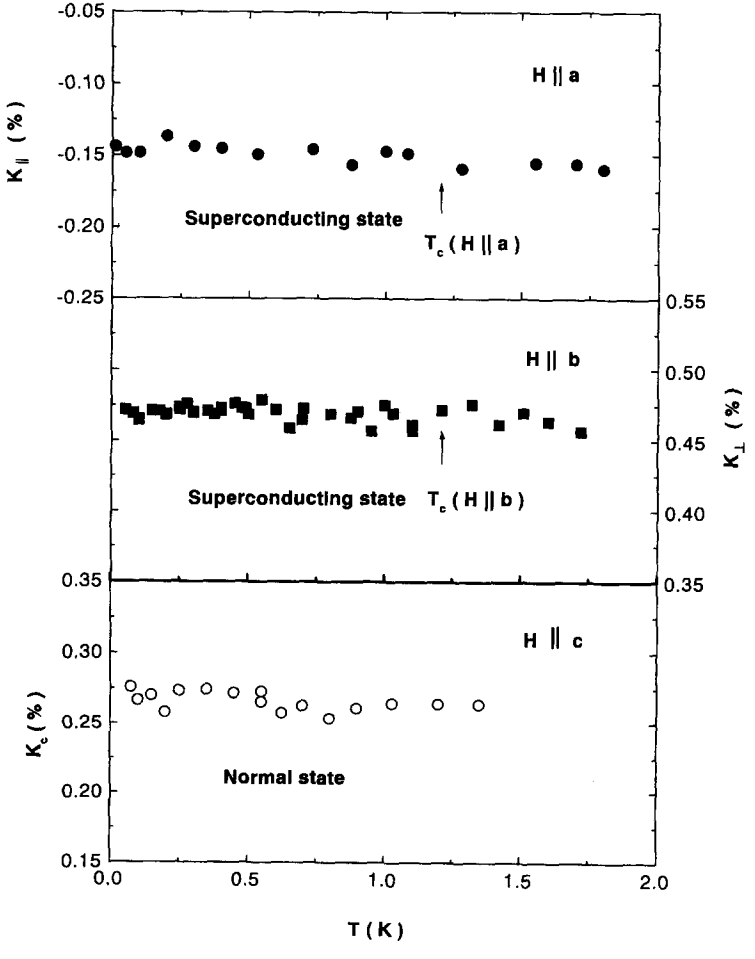

Fig. 53. Temperature-dependence of the ^{17}O Knight shift for Sr_2RuO_4 with $T_c = 1.48$ K.[111] $K_{\parallel}$, $K_{\perp}$ and K_c denote K values along and perpendicular to the Ru—O—Ru bonding axis, and K along the c-axis, respectively.

$SrRuO_3$ is a ferromagnetic metal with a Curie temperature of ~160 K. On the basis of these experimental results, together with the physical background of Ru^{4+}, Rice and Sigrist suggested that the Cooper pairs in Sr_2RuO_4 would be in the spin-triplet state analogous to ^3He, which contrasts with the spin-singlet d-wave pairing in high-T_c superconductors.[109]

Figure 51 shows the temperature-dependence of the value of $1/T_1$ of Ru in high-quality single crystals of Sr_2RuO_4 with $T_c \sim 1.5$ K together with those from previous crystals with a lower $T_c \sim 0.7$ K.[107, 110] In both sets of crystals,

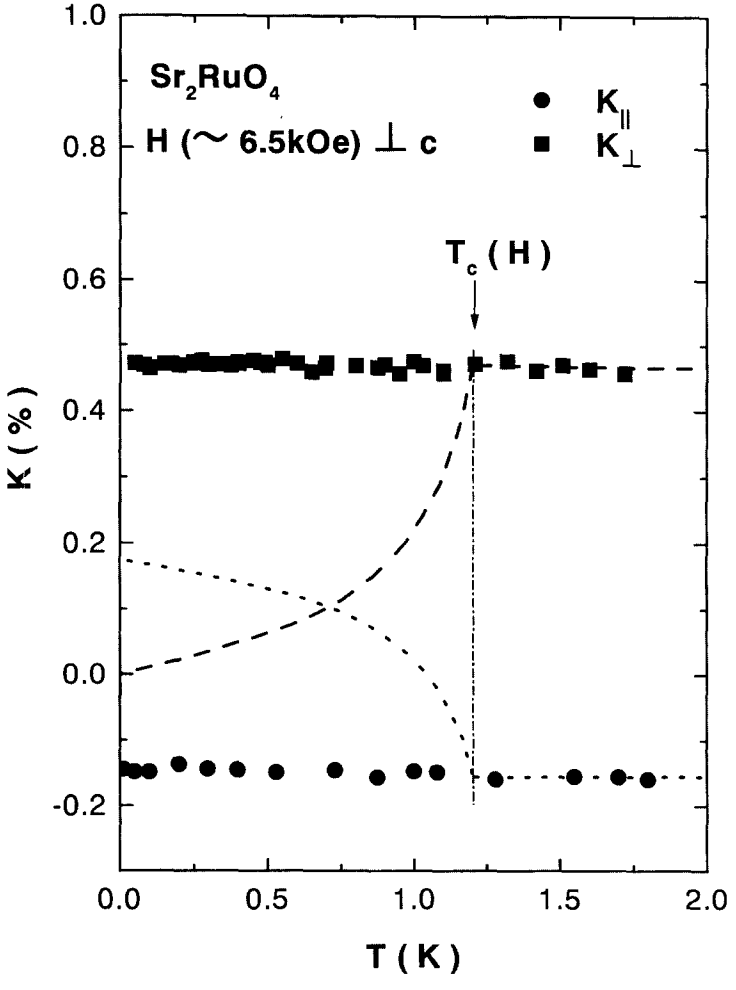

Fig. 54. Temperature dependence of $K_{||}$ and $K_{\perp}$ at low temperatures. Broken lines below T_c indicate the calculation for the spin-singlet d-wave model with parameters to explain the temperature dependence of K in $YBa_2Cu_3O_7$.

$1/T_1$ has no coherence peak, followed by a sharp decrease below T_c. The large linear part, associated with the pair-breaking effect due to the imperfection of the crystal, is seen in the lower-T_c crystals. The relation between T_c and N_{res} agrees well with the theory as shown in Fig. 18 where $T_{c0} = 1.5$ K is adopted, consistent with the present high-T_c crystals. In high-T_c crystals, the T^3 behaviour has been observed below 1 K down to 0.15 K, which implies the formation of the line-node gap. The $1/T_1$ behaviour can be well interpreted by the line-node-gap model $\Delta(\phi) = \Delta_0 \cos(\phi)$ with $2\Delta_0/k_B T_c \sim 4$. The results for $1/T_1$ indicate p- or d-wave pairing.

In order to distinguish between d- or p-waves, measurement of the Knight shift for ^{17}O-substituted high-T_c crystals was carried out.[111] Figure 52 shows the value of K along the c-axis (K_c) and K along ($K_{||}$) and perpendicular ($K_\perp$) to

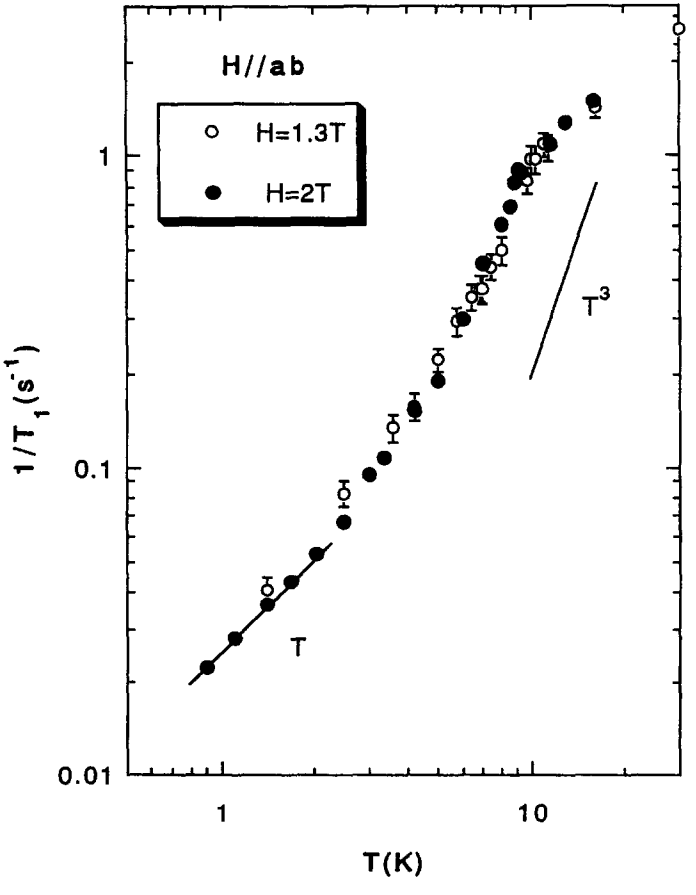

Fig. 55. A plot of $1/T_1$ for B in YNi_2B_2C.[117]

the Ru—O—Ru bond axis, plotted against the bulk susceptibility.[112] The anisotropy of the Knight shift is due to the anisotropy of the hyperfine coupling. The orbital part is almost zero for $K_{\|}$ while it has a large value for both $K_{\perp}$ and K_c. As shown in Fig. 53, the Knight shift in each direction does not decrease below T_c. Since the crystals would be in the SC state under the experimental condition where $K_{\|}$ and $K_{\perp}$ were measured, the invariant Knight shift below T_c indicates that the Cooper pairing is of a spin-triplet p-wave type.[111] Figure 54 shows the temperature dependence of $K_{\|}$ and $K_{\perp}$ at low temperatures. Broken lines below T_c indicate the calculation for the spin-singlet d-wave state in two dimensions with $d_{x^2-y^2}$ symmetry, using the parameters $\Delta(\phi) = \Delta_0 \cos(2\phi)$ and $2\Delta_0 = 8k_B T_c$ which explains the Knight-shift behaviour in the SC state of $YBa_2Cu_3O_7$. Recently, an invariant Knight shift on passing through T_c was also observed by Ru NMR measurements.[113]

In addition to the Knight-shift results, muon-spin-rotation (μSR) experiments have revealed the existence of a spontaneous magnetic field below T_c, suggesting that the time-reversal symmetry is broken in the SC state.[114] These experimental results provide evidence that Sr_2RuO_4 is a spin-triplet p-wave superconductor with a finite angular momentum of the pairs, $L = 1$. It has been pointed out theoretically that the promising p-wave superconducting vectors have $\boldsymbol{d}(\boldsymbol{k}) = \hat{z}\Delta_0(\sin k_x + i \sin k_y)$ with a strongly anisotropic gap[115] or $\boldsymbol{d}(\boldsymbol{k}) = \hat{z}\Delta_0(k_x + ik_y)\cos(ck_z)$ with line nodes[116] if the non-magnetic impurity effect is incorporated.

5.2. YNi_2B_2C

Figure 55 shows the temperature dependence of $1/T_1$ ^{11}B in YNi_2B_2C.[117] The value of $1/T_1$ decreases without a coherence peak below T_c with a large linear temperature dependence. The result is consistently explained by d-wave pairing with some imperfection or impurity in the specimen. It has also been suggested that the antiferromagnetic spin fluctuation governs the temperature-dependent $1/T_1T$ value in the Ni-Boroncarbides.[118,119] These spin fluctuations may play an important role in the occurrence of anisotropic superconductivity.

6. CONCLUSIONS

(1) It is concluded from the temperature dependence of $1/T_1$ and the Knight shift that the nature of the superconductivity in strongly correlated electron systems is anisotropic: d-wave symmetry in $CeCu_2Si_2$, UPd_2Al_3 and high-T_c materials and p- or f-wave in UPt_3 and Sr_2RuO_4.

(2) The local hole numbers at the Cu and O sites in the CuO_2 plane in high-T_c materials have been obtained from analysis of the NQR frequencies of Cu and ^{17}O. These hole numbers are correlated with several physical

quantities, such as the magnitude of the AFSF, T_c etc. There are optimum hole numbers at the Cu and O sites to give the highest T_c value.

(3) The anisotropic nature of the superconductivity suggests that the mechanism of the superconductivity is magnetic in origin. In particular, the scale of $1/T_1$ to T/T_c in $YBCO_7$ with Ni impurities provides direct evidence for the attractive force to be due to spin fluctuation. This is irrespective of the theoretical models which correspond to the isotope effect in phonon-mediated superconductivity. The small isotope exponent obtained by $^{16}O-^{18}O$ isotope exchange in $YBCO_8$ can also be explained as due to a decrease in the energy of the antiferromagnetic spin fluctuation.

(4) Analysis of the $1/T_1T$ and $1/T_{2G}$ data in several high-T_c materials with moderate hole doping provides a value of $\chi_Q\Gamma_Q$ which is approximately proportional to T_c. This strongly supports the AFSF-mediated superconductivity model proposed by Moriya *et al.*[57] and Pines *et al.*[75]

(5) Regarding the pseudogap phenomena, the gap opening temperatures for $1/T_1T$ and K agree with each other if one adopts the temperature at which K starts to decrease sharply. This temperature agrees with those obtained by other measurements, indicating that the gap opens not only in χ_Q but also in the density of states of the one-electron energy spectrum. At present, there are several controversial suggestions for the origin of the spin gap, which has yet to be decided.

(6) The difference in the doping level in each CuO_2 layer in the CuO_2 multilayer system increases with increasing total holes and layer numbers. The SC characteristics in the CuO_2 layers are decoupled from each other to an extent depending upon the local doping level.

REFERENCES

1. F. Steglich, J. Aarts, C. D. Bredl, W. Lieke, D. Meschede, W. Franz and H. Schafer, *Phys. Rev. Lett.*, 1979, **43**, 1892.
2. J. G. Bednorz and K. A. Muller, *Z. Phys. B*, 1986, **64**, 189.
3. For example, Heavy fermion superconductors
   (a) K. Asayama, *Frontiers in Solid State Science* vol. 1 *Selected Topics in Superconductivity* eds L. C. Gupta and M. S. Malik, World Science, 1993, pp. 583–623.
   (b) Y. Kuramoto and Y. Kitaoka, *Dynamics of Heavy Electron*, Int Ser. Mon. Phys., Oxford, 2000.
   High T_c-superconductors
   (c) Y. Kitaoka, K. Ishida, S. Ohsugi, K. Fujiwara, G.-q. Zheng and K. Asayama, *J. Appl. Magn. Resonance*, 1992, **3**, 549.
   (d) K. Asayama, Y. Kitaoka, G.-q. Zheng and K. Ishida, *Prog. NMR Spectroscopy*, 1996, **28**, 221.
   (e) K. Asayama, Y. Kitaoka, G.-q. Zheng, K. Ishida, K. Magishi and Y. Tokunaga, Proc. LT21, *Czech. J. Phys.*, 1996, **46** suppl. 3087.
4. H. Monien and D. Pines, *Phys. Rev. B*, 1990, **41**, 6297.

5. (a) R. A. Ferrell, *Phys. Rev. Lett.*, 1959, **3**, 262. (b) P. W. Anderson, *Phys. Rev. Lett.*, 1959, **3**, 325.
6. K. Miyake and K. Asayama, *Phys. Rev. B*, 2000, **62**, 11363.
7. N. D. Mathur, F. M. Grosche, S. R. Julian, I. R. Walker, D. M. Freye, R. K. W. Haselwimmer and G. G. Lonzarich, *Nature*, 1998, **394**, 39.
8. Y. Kitaoka, K. Ueda, T. Kohara, K. Asayama, Y. Onuki and T. Komatsubara, *J. Magn. Magn. Mater.*, 1985, **52**, 341.
9. D. E. MacLaughlin, C. Tien, W. G. Clark, M. D. Lan, Z. Fisk, J. L. Smith and H. R. Ott, *Phys. Rev. Lett.*, 1984, **53**, 1833.
10. Y. Kohori, T. Kohara, H. Shibai, Y. Oda, Y. Kitaoka and K. Asayama, *J. Phys. Soc. Jpn*, 1988, **57**, 395.
11. Y. Kitaoka, K. Fujiwara, Y. Kohori, K. Asayama, Y. Ōnuki and T. Komatsubara, *J. Phys. Soc. Jpn*, 1985, **54**, 3686.
12. Y. Kitaoka, H. Arimoto, Y. Kohori, K. Asayama, *J. Phys. Soc. Jpn*, 1985, **54**, 3236.
13. T. Kohara, Y. Kohori, K. Asayama, Y. Kitaoka, M. B. Maple and M. S. Torikachvili, *J. Appl. Phys.*, 1987, **26** 1247. K. Matsuda, Y. Kohori and T. Kohara, *J. Phys. Soc. Jpn*, 1996, **65**, 679.
14. M. Kyogaku, Y. Kitaoka, K. Asayama, C. Geibel, C. Schank and F. Steglich, *J. Phys. Soc. Jpn*, 1992, **61**, 2660. H. Tou, Y. Kitaoka, K. Asayama, C. Geibel, C. Schank and F. Steglich, *J. Phys. Soc. Jpn*, 1995, **64**, 725.
15. Y. Kohori, K. Matsuda and T. Kohara, *Solid State Commun.*, 1995, **95**, 121. K. Matsuda, Y. Kohori and T. Kohara, *Phys. Rev. B*, 1997, **55**, 15223.
16. H. Tou, Y. Kitaoka, T. Kamatsuka, K. Asayama, C. Geibel, F. Steglich, S. Sullow and J. A. Mydosh, *Physica B*, 1997, **230–232**, 360.
17. Y. Kitaoka, H. Yamada, K. Ueda, Y. Kohori, T. Kohara, Y. Oda and K. Asayama, *Jpn. J. Apply. Phys. Suppl.*, 1987, **26**, 1221. K. Ueda, Y. Kitaoka, H. Yamada, Y. Kohori and K. Asayama, *J. Phys. Soc. Jpn*, 1987, **56**, 867.
18. Y. Kohori, T. Kohara, H. Shibai, Y. Oda, Y. Kitaoka and K. Asayama, *J. Phys. Soc. Jpn*, 1988, **57**, 395.
19. H. Tou, Y. Kitaoka, K. Asayama, N. Kimura, Y. Ōnuki, E. Yamamoto and K. Maezawa, *Phys. Rev. Lett.*, 1996, **77**, 1374, *ibid.*, 1998, **80**, 3129.
20. R. A. Fischer, S. Kim, B. F. Woodfield, N. E. Phillips, L. Taillefer, K. Hasselbach and J. Flouquet, *Phys. Rev. Lett.*, 1989, **62**, 1441. K. Hasselbach, L. Taillefer and J. Flouquet, *Phys. Rev. Lett.*, 1989, **63**, 93.
21. L. Taillefer, J. Flouquet and G. G. Lonzarich, *Physica B.*, 1991, **169**, 257.
22. Y. Kohori, K. Matsuda and T. Kohara, *J. Phys. Soc. Jpn*, 1996, **65**, 1083.
23. K. Ishida *et al.*, unpublished.
24. A. Krimmel, P. Fisher, B. Roessli, H. Maletta, C. Geibel, C. Schank, A. Grauel, A. Loidl and F. Steglich, *Z. Phys. B*, 1992, **86**, 161.
25. C. Broholm, H. Lin, P. T. Matthews, T. M. Mason, W. J. L. Buyers, M. F. Collon, A. A. Menovsky, J. A. Mydosh and J. K. Kjems, *Phys. Rev. B*, 1991, **43**, 12809.
26. G. Appeli, E. Bucher, C. Broholm, J. K. Kjem, J. Baumann and J. Hufnagl, *Phys. Rev. Lett.*, 1988, **60**, 615.
27. F. Steglich, B. Buschinger, P. Gegenwart, M. Lohmann, R. Helfrich, C. Langhammer, P. Hellmann, L. Donnevert, S. Thomas, A. Link, C. Geibel, M. Lang, G. Sparn and W. Assmus, *J. Phys. Cond. Matter*, 1996, **8**, 9909.
28. H. Nakamura, Y. Kitaoka, T. Iwai, H. Yamada and K. Asayama, *J. Magn. Magn. Mater*, 1988. **76–77**, 676; *J. Phys. Cond. Matter*, 1992, **4**, 473.
29. P. Gegenwart, C. Langhammer, C. Geibel, R. Helfrich, M. Lang, G. Span and F. Steglich, *Phys. Rev. Lett.*, 1998, **81**, 1501.
30. K. Ishida, Y. Kawasaki, K. Tabuchi, K. Kashima, Y. Kitaoka, K. Asayama, C. Geibel and F. Steglich, *Phys. Rev. Lett.*, 1999, **82**, 5353.
31. K. Ishida, Y. Kitaoka and K. Asayama, *J. Phys. Soc. Jpn*, 1989, **58**, 36. S. Ohsugi, Y. Kitaoka, K. Ishida and K. Asayama, *J. Phys. Soc. Jpn*, 1991, **60**, 2351.

32. K. Fujiwara, Y. Kitaoka, K. Asayama, H. Sasakura, S. Minamigawa, K. Nakanishi, M. Kogachi, N. Fukuoka and A. Yanase, *J. Phys. Soc. Jpn*, 1989, **58**, 380.
33. K. Fujiwara, Y. Kitaoka, K. Asayama, Y. Shimakawa, T. Manako, Y. Kubo and A. Endo, *Physica B*, 1990, **165–166**, 1295.
34. M. Mali, D. Brinkmann, L. Puli, J. Roos, H. Zimmermann and J. Hullinger, *Phys. Lett. A.*, 1987, **124**, 112. W. W. Warren. Jr., R. E. Walstedt, G. F. Brennert, G. P. Espinosa and J. P. Remeika, *Phys. Rev. Lett.*, 1987, **59**, 1860.
35. H. Zimmermann, N. Mali, D. Brinkmann, J. Karpiinski, E. Kaldis and S. Rusiecki, *Physica C.*, 1989, **159**, 681.
36. G.-q. Zheng, Y. Kitaoka, K. Asayama, K. Hamada, H. Yamauchi and S. Tanaka, *J. Phys Soc. Jpn*, 1995, **64**, 3184; *Physica C*, 1996, **260**, 197.
37. K. Ishida, Y. Kitaoka, K. Asayama, T. Mochiku and K. Kadowaki, *J. Phys Soc. Jpn*, 1994, **63**, 1104.
38. K. Magishi, Y. Kitaoka, G.-q. Zheng, K. Asayama, T. Kondo, Y. Shimakawa, T. Manako and Y. Kudo, *Phys. Rev. B*, 1996, **54**, 10131.
39. K. Magishi, Y. Kitaoka, G.-q. Zheng, K. Asayama, K. Tokiwa, A. Iyo and H. Ihara, *J. Phys. Soc. Jpn*, 1995, **64**, 4561.
40. Y. Tokunaga, K. Ishida, K. Magishi, S. Ohsugi, G.-q. Zheng, Y. Kitaoka, K. Asayama, A. Iyo, K. Tokiwa and H. Ihara, *Physica C*, 1999, **259–261**, 571.
41. Y. Tokunaga, K. Ishida, Y. Kitaoka, K. Asayama, K. Tokiwa, A. Iyo and H. Ihara, *Phys. Rev. B*, 2000, **61**, 9707.
42. Y. Kitaoka, S. Hiramatsu, T. Kondo and K. Asayama, *J. Phys. Soc. Jpn*, 1988, **57**, 30.
43. K. Asayama, Y. Kitaoka, K. Fujiwara, K. Ishida and S. Ohsugi, Proc. 2nd ISSP Int. Symp. The Physics and Chemistry of Oxide Superconductors, *Springer Proceedings in Physics*, 1992, **60**, 349.
44. P. C. Hammel, M. Takigawa, R. H. Heffner, Z. Fisk and K. C. Ott, *Phys. Rev. Lett.*, 1989, **63**, 1992.
45. Y. Kohori *et al.*, *J. Magn. Magn. Mater.*, 1990, **90–91**, 667.
46. K. Ishida, Y. Kitaoka, G.-q. Zheng and K. Asayama, *J. Phys. Soc. Jpn*, 1991, **60**, 3516. S. Ohsugi, Y. Kitaoka, K. Ishida, G.-q. Zheng, K. Asayama, *J. Phys. Soc. Jpn*, 1994, **63**, 700.
47. S. E. Barrett, D. J. Durand, C. H. Pennington, C. P. Slichter, T. A. Friedmann, J. P. Rice and D. M. Ginsberg, *Phys. Rev. B*, 1990, **41**, 6283.
48. K. Ishida, Y. Kitaoka, T. Yoshitomi, N. Ogata, T. Kamino and K. Asayama, *Physica C*, 1991, **179**, 29. *J. Phys. Soc. Jpn*, 1993, **62**, 2803.
49. S. Schmitt-Rink, K. Miyake and C. M. Varma, *Phys. Rev. Lett.*, 1986, **57**, 2575.
50. A. T. Fiory, A. F. Hevard, P. M. Mankiewich and R. E. Howard, *Phys. Rev. Lett.*, 1988, **61**, 1419. Y. J. Uemura *et al.*, *J. Phys. (France)*, 1988, **49**, suppl. c8–2807.
51. K. Asayama, G.-q. Zheng, Y. Kitaoka, K. Ishida and K. Fujiwara, *Physica C*, 1991, **178**, 281.
52. W. N. Hardy, D. A. Bonn, D. C. Morgan, R. Liang and K. Zhang, *Phys. Rev. Lett.*, 1993, **70**, 3999.
53. D. A. Bonn, S. Kamal, K. Zheng, R. Liang, D. J. Baar and E. Klein, *Phys. Rev. B*, 1994, **50**, 4051.
54. Y. Onishi, Y. Ohashi, Y. Shingaki and K. Miyake, *J. Phys. Soc. Jpn*, 1996, **65**, 675.
55. K. Asayama, Y. Kitaoka, G.-q. Zheng, K. Ishida and S. Ohsugi, *Hyperfine interaction*, 1993, **79**, 835. Y. Kitaoka, K. Ishida and K. Asayama, *J. Phys. Soc. Jpn*, 1994, **63**, 2052.
56. T. Hotta, *J. Phys. Soc. Jpn*, 1993, **62**, 272.
57. T. Moriya, Y. Takahashi and K. Ueda, *J. Phys. Soc. Jpn*, 1990, **59**, 2095. T. Moriya and K. Ueda, *ibid.*, 1994, **63**, 1871.
58. N. Bulut and D. J. Scalapino, *Phys. Rev. Lett.*, 1991, **67**, 2898. N. Bulut and D. J. Scalapino, *Phys. Rev. B*, 1992, **45**, 2371.
59. Y. Itoh, H. Yasuoka, Y. Fujiwara, Y. Ueda, T. Machi, I. Tomeno, K. Tai, N. Koshizuka and S. Tanaka, *J. Phys. Soc. Jpn*, 1992, **61**, 1287.

60. G.-q. Zheng, Y. Kitaoka, K. Ishida and K. Asayama, *J. Phys. Soc. Jpn*, 1995, **64**, 2524.
61. K. Hanzawa, F. Komatsu and K. Yosida, *J. Phys. Soc. Jpn*, 1990, **59**, 3345.
62. Y. Ohta, W. Koshibae and S. Maekawa, *J. Phys. Soc. Jpn*, 1992, **61**, 2198.
63. G.-q. Zheng, E. Yanase, Y. Kitaoka, K. Asayama, Y. Kodama, R. Tanaka and S. Endo, *Solid State Commun.*, 1991, **79**, 51.
64. G.-q. Zheng, T. Mito, Y. Kitaoka, K. Asayama and Y. Kodama, *Physica C*, 1995, **243**, 337.
65. H. Zimmermann, M. Mali, I. Mangelschots, J. Roos, D. Brinkmann, J. Karpinski, S. Rusiecki and E. Kaldis, *J. Less-Common Metals*, 1990, 164–165, 132.
66. Y. Yamada, *Physica C*, 1991, **173**, 185.
67. Y. Tokunaga, K. Ishida, Y. Kitaoka and K. Asayama, *Solid State Commun.*, 1997, **103**, 43.
68. P. Mendels, H. Alloul, G. Collin, N. Blanchard, J. F. Marucco and J. Bobroff, *Physica C*, 1994, **235**, 1595.
69. F. Mila and T. M. Rice, *Phys. Rev. B*, 1989, **40**, 11382. F. Mila and T. M. Rice, *Physica C*, 1989, **157**, 561.
70. T. Shimizu, H. Yasuoka, T. Tsuda, K. Kosuge and Y. Ueda, *Bull. Magn. Res.*, 1990, **12**, 39.
71. H. Yasuoka, T. Shimizu, Y. Ueda and K. Kosuge, *J. Phys. Soc. Jpn*, 1988, **57**, 2659.
72. F. Raffa, T. Ohno, M. Mali, J. Roos, D. Brinkmann, K. Conder and M. Eremin, *Phys. Rev. Lett.*, 1998, **81**, 5912.
73. T. Ohno and K. Asayama, *Phys. Lett. A*, 1999, **258**, 367.
74. G.-q. Zheng, T. Odaguchi, Y. Kitaoka, K. Asayama, Y. Kodama, K. Mizuhashi and S. Uchida, *Physica C*, 1996, **263**, 367.
75. D. Pines, *Physica C*, 1991, **185–189**, 120. D. Monthoux and D. Pines, *Phys. Rev. B*, 1994, **47**, 6069.
76. D. Thelen and D. Pines, *Phys. Rev. B*, 1994, **49**, 3528.
77. N. J. Curro, T. Imai, C. P. Slichter and B. Dabrowski, *Phys. Rev. B*, 1997, **56**, 877.
78. Y. Tokunaga, K. Ishida, Y. Kitaoka and K. Asayama, *Physica C*, 1997, **282–287**, 1352.
79. G.-q. Zheng, Odaguchi, T. Mito, Y. Kitaoka, K. Asayama and Y. Kodama, *J. Phys. Soc. Jpn*, 1993, **62**, 2591.
80. K. Kakurai, S. Shamoto, T. Kiyokura and M. Sato, J. M. Tranquada and G. Shirane, *Phys. Rev. B*, 1993, **48**, 3485.
81. H. Harashina, S. Shamoto, T. Kiyokura, M. Sato and K. Kakurai, *J. Phys. Soc. Jpn*, 1993, **62**, 4009.
82. Y. Sidis, P. Bourges and B. Hennion, L. P. Regnault, R. Villeneuve, G. Collin and J. F. Marucco, *Phys. Rev. B*, 1996, **53**, 6811.
83. H. F. Fong, P. Bourges, Y. Sidis, L. P. Regnault, J. Bossy, A. Ivanov, D. L. Milius, I. A. Aksay and B. Keimer, *Phys. Rev. Lett.*, 1999, **82**, 1939.
84. M. Julien, T. Fehr, M. Horvati, C. Berthier, O. N. Bakharev, P. Segransan, G. Collin and J.-F. Marucco, *Phys. Rev. Lett.*, 2000, **84**, 3422.
85. H. Fukuyama and H. Kohno, *J. Magn. Magn. Mater.*, 1998, **177–181**, 483.
86. J. Oitmaa, *J. Magn. Magn. Mater.*, 1998, **177–181**, 620.
87. K. Ishida, K. Yoshida, T. Mito, Y. Tokunaga, Y. Kitaoka, K. Asayama, Y. Nakayama, J. Shimoyama and K. Kishio, *Phys. Rev. B*, 1998, **58**, R5960.
88. M. Takigawa and D. B. Mitzi, *Phys. Rev. Lett.*, 1994, **73**, 1287.
89. M. Oda, K. Hoya, R. Kubota, C. Manabe, N. Momono, T. Nakano and M. Ido, *Physica C*, 1997, **281**, 135.
90. H. Ding, T. Yokoya, J. C. Campuzano, T. Takahashi, M. Randeria, M. R. Norman, T. Mochiku, K. Kadowaki and J. Giapintzakis, *Nature*, 1996, **382**, 51.
91. J. M. Harris, Z. X. Shen, P. J. White, D. S. Marshall and M. C. Schabel, *Phys. Rev. B*, 1996, **54**, R15665.
92. Y. Tokunaga, K. Ishida, K. Yoshida, T. Mito, Y. Kitaoka, Y. Nakayama, J. Shimoyama, K. Kishio, O. Narikiyo and K. Miyake, *Physica B*, 2000, 284–288, 663.

93. G.-q. Zheng, H. Ozaki,W. G. Clark, Y. Kitaoka, P. Kuhns, A. P. Reyes, W. G. Moulton, T. Kondo, Y. Shimakawa and Y. Kubo, *Phys. Rev. Lett.*, 2000, **85**, 405.
94. G.-q. Zheng, H. Ozaki, W. G. Clark, M. Sakai, Y. Kitaoka, P. Kuhns, A. P. Reyes, W. Moulton, T. Kondo, Y. Shimakawa and Y. Kubo, *Physica C*, 2000, 341–348, 819.
95. G.-q. Zheng, W. G. Clark, Y. Kitaoka, K. Asayama, Y. Kodama, P. Kuhns and W. Moulton, *Phys. Rev. B*, 1999, **60**, R9947.
96. Y. Yanase and K. Yamada, *J. Phys. Soc. Jpn*, 1999, **68**, 2999, *ibid*, 2000, **69**, 2209.
97. T. Tanamoto, H. Kohno and H. Fukuyama, *J. Phys. Soc. Jpn*, 1994, **63**, 2739.
98. V. J. Emery and S. A. Kivelson, *Nature (London)*, 1995, **374**, 434.
99. K. Miyake and O. Narikiyo, *J. Phys. Soc. Jpn*, 1994, **63**, 3821.
100. A. Kampf and J. R. Schrieffer, *Phys. Rev. B*, 1990, **41**, 6399.
101. T. Sakai and Y. Takahashi, *J. Phys. Soc. Jpn*, 1998, **67**, 2630.
102. K. Ishida, Y. Tokunaga, Y. Kitaoka, G.-q. Zheng, K. Magishi, H. Mukuda, H. Tou, T. Mito and K. Asayama, *Physica B*, 1999, **259–261**, 511.
103. H. Ihara, K. Tokiwa, H. Ozawa, M. Hirabayashi, A. Negishi, H. Matuhata and Y. S. Song, *Jpn. J. Appl. Phys.*, Part 1, 1994, **33**, 503 *Jpn. J. Appl. Phys.*, Part 2, 1994, **33**, L300; *Physica C*, 1994, **235–240**, 981.
104. Y. Tokunaga, H. Kotegawa, K. Ishida, G.-q. Zheng, Y. Kitaoka, K. Tokiwa, A. Iyo and H. Ihara, *J. Low Temp. Phys.*, 1999, **117**, 473.
105. M. Ogino, T. Watanabe, H. Tokiwa, A. Iyo and H. Ihara, *Physica C*, 1996, **258**, 384.
106. Y. Maeno, H. Hashimoto, K. Yoshida, S. Nishizaki, T. Fujita, J. G. Bednorz and F. Lichtenberg. *Nature*, 1994, **372**, 532.
107. K. Ishida, Y. Kitaoka, K. Asayama, S. Ikeda, S. Nishizaki, Y. Maeno, K. Yoshida and T. Fujita, *Phys. Rev. B*, 1996, **56**, R505.
108. T. Oguchi, *Phys. Rev. B*, 1995, **51**, 1385.
109. T. M. Rice and M. Sigrist, *J. Phys. Cond. Matter*, 1995, **7**, L643.
110. K. Ishida, H. Mukuda, Y. Kitaoka, K. Asayama, Z. Q. Mao and Y. Maeno, *Phys. Rev. Lett.*, 2000, **84**, 5387.
111. K. Ishida, H. Mukuda, Y. Kitaoka, K. Asayama, Z. Q. Mao, Y. Mori and Y. Maeno, *Nature*, 1998, **396**, 658.
112. H. Mukuda, K. Ishida, Y. Kitaoka, K. Asayama, Z. Q. Mao, Y. Mori and Y. Maeno, *J. Phys. Soc. Jpn*, 1998, **67**, 3945.
113. K. Ishida, H. Mukuda, Y. Kitaoka, Z. Q. Mao, H. Fukazawa and Y. Maeno, *Phys. Rev. B*, 2001, 63, R 060507.
114. G. M. Luke, Y. Fudamoto, K. M. Kojima, M. I. Larkin, J. Merrin, B. Nachumi, Y. J. Uemura, Y. Maeno, Z. Q. Mao, Y. Mori, H. Nakamura and M. Sigrist, *Nature*, 1998, **394**, 558.
115. K. Miyake and O. Narikiyo, *Phys. Rev. Lett.*, 1999, **83**, 1423.
116. Y. Hasegawa, K. Machida and M. Ozaki, *J. Phys. Soc. Jpn*, 2000, **69**, 336.
117. G.-q. Zheng, Y. Wada, K. Hashimoto, Y. Kitaoka, K. Asayama, K. Takeya and K. Kadowaki, *J. Phys. Chem. Solids*, 1998, **59**, 2169.
118. K. Ikushima, J. Kikuchi, H. Yasuoka, R. J. Cava, H. Takagi, J. J. Krajewski and W. F. Peck, Jr., *J. Phys. Soc. Jpn*, 1994, **63**, 2878.
119. T. Kohara, T. Oda, K. Ueda, Y. Yamada, A. Mahajan, K. Elankumaran, Z. Hossian, L. C. Gupta, R. Nagarajan and R. Vijayaraghavan, *Phys. Rev. B*, 1995, **51**, 3985.

Index

Note — Page numbers in *italic* type refer to figures and tables.